論文 / 著書情報
Article / Book Information

題目(和文)	
Title(English)	Investigation of Plastic Deformation Behavior with the Portevin-Le Chatelier Effect in Austenitic Stainless Steel
著者(和文)	LEESeungyong
Author(English)	Seungyong Lee
出典(和文)	学位:博士（工学）, 学位授与機関:東京工業大学, 報告番号:甲第11768号, 授与年月日:2022年3月26日, 学位の種別:課程博士, 審査員:中田 伸生,尾中 晋,木村 好里,寺田 芳弘,村石 信二
Citation(English)	Degree:Doctor (Engineering), Conferring organization: Tokyo Institute of Technology, Report number:甲第11768号, Conferred date:2022/3/26, Degree Type:Course doctor, Examiner:,,,,
学位種別(和文)	博士論文
Type(English)	Doctoral Thesis

Doctoral Thesis

Investigation of Plastic Deformation Behavior with the Portevin-Le Chatelier Effect in Austenitic Stainless Steel

Seung-Yong Lee

Academic Supervisor : Nobuo Nakada

Sub-supervisor : Susumu Onaka

Department of Materials Science and Engineering

Tokyo Institute of Technology

Contents -Page

1. Research Background **-5-**

1.1 Introduction -6-

1.2 The Portevin-Le Chatelier (PLC) Effect -8-

1.2.1 Phenomenology -9-

1.2.2 Types of serration -10-

1.3 Dynamic Strain Aging (DSA) -13-

1.3.1 The physical model for DSA -14-

1.4 Motivation and objective of this study -17-

1.5 References -19-

2. Macroscopic and Microscopic Characterizations of the Portevin-Le Chatelier Effect in Austenitic Stainless Steel using High-Temperature Digital Image Correlation Analysis **-21-**

2.1 Introduction -22-

2.2 Experimental -24-

2.2.1 Material -24-

2.2.2 Tensile testing -24-

2.2.3 DIC analysis -25-

2.3 Results and discussion -30-

2.3.1 Macroscopic characterization of high-temperature PLC effect -30-

2.3.1.1 Evaluation of high-temperature tensile property by DIC -30-

2.3.1.2 Macroscopic strain rate variation associated with PLC band propagation\ -35-

2.3.1.3 Control mechanism of dynamic strain aging in austenitic stainless steel -39-

2.3.2 Microscopic characterization of high-temperature PLC band -42-

2.3.2.1 Type variation of high-temperature PLC band in terms of band propagation behavior -42-

2.3.2.2 Local strain development by A-type PLC band propagations -46-

2.4 Conclusions -56-

2.5 References -58-

3. Serrated Flow Accompanied with Dynamic Type Transition of the Portevin-Le Chatelier Effect in Austenitic Stainless Steel

-60-

3.1 Introduction -61-

3.2 Experimental -66-

3.2.1 Material -66-

3.2.2 Tensile testing with DIC analysis -66-

3.2.3 Definition of serration type -67-

3.3 Results -71-

3.3.1 Experimental results -71-

3.3.1.1 Serration behavior -71-

3.3.1.2 Correlation between serration and PLC band behavior -79-

3.3.1.3 Effect of global strain rate on dynamic type transition behavior -90-

3.3.2 Numerical simulation for the effect of strain rate on PLC band behavior

3.3.2.1 Ananthakrishna (AK) model -93-

3.3.2.2 Setting parameters for AK model -96-

3.3.2.3. Effect of strain rate on PLC band propagation and serration behavior -97-

3.4 Discussion -105-

3.5 Conclusions -109-

3.6 References -111-

3.7 Appendix -114-

3.7.1 Three dislocations behavior during the PLC effect in AK model -114-

3.7.2 Determination of the PLC band width -115-

4. Effects of Grain Size and Interstitial Atoms on the Portevin-Le Chatelier Effect in Austenitic Stainless Steel **-120-**

4.1 Introduction -121-

4.2 Experimental -123-

4.2.1 Material -123-

4.2.2 Tensile testing and DIC analysis -123-

4.3 Results and discussion -127-

4.3.1 Effect of grain size -127-

4.3.1.1 Serration behavior -127-

4.3.1.2 A-type PLC band behavior -130-

4.3.2 Effect of replacement of C by N -133-

4.4 Conclusion -137-

4.5 References -138-

5. Conclusions and Remarks **-140-**

Chapter 1

Research Background

1.1 Introduction

Among many metallic materials, “steel” has the closest relationship with our society because of its applications in almost all fields, such as structures, transportations, industries, and art. Thus, research of steel is the most important for making our society safer and more convenient than the other metallic materials.

Generally, various alloying elements are added into steels in order to improve target properties required for many applications. Although one of the major drawbacks of plain steels is “corrosion”, alloying Chromium (Cr) into steels can solve this problem. When at least 11 wt.% of Cr is added into steels, self-healing Cr-oxide can form on the steel surface resulting in good corrosion resistance, and we refer to the alloy as “stainless steel (STS)”. STSs are extensively used in many fields, for example, from cooking utensils in our daily life to spaceships in cutting-edge industries.

Among various types of STSs, austenitic stainless steel (γ-STS) has fine austenite stability due to Nickel (Ni), Carbon (C), and so on. Thus, γ-STSs have excellent high-temperature mechanical properties, and they are actively being used at high-temperatures in many industrial fields. Responding to recent global societies where the required

conditions are getting complex and harsher, many researchers are trying to improve their properties by means of the control of the addition of various alloying elements and their amount [1].

The addition of alloying elements can also invoke a dynamic phenomenon known as "Dynamic Strain Aging (DSA) [2-7]" in specific deformation conditions. Due to the DSA, an unexpected deformation manner as serration can take place in stress-strain curves, which is called as the Portevin-Le Chatelier (PLC) effect [8-10]. Since high-temperature mechanical properties is significantly affected by the PLC effect caused by DSA, it is very important to understand how material deforms under PLC effect preceding to application of the material. Nevertheless, there are been few studies on the high-temperature PLC effect in γ-STS despite of the importance. In this study, therefore, the high-temperature PLC effect and the accompanying mechanical properties in austenitic stainless steels was scrutinized by connecting microscopic DSA effect with mesoscopic strain localization behavior.

1.2 The Portevin-Le Chatelier (PLC) Effect

When metallic materials with solute atoms are subjected into specific deformation conditions, such as uniaxial-tensile and compression, plastic flow may display oscillatory plastic yielding under certain ranges of strain rates and testing temperatures. This oscillatory feature refers to as “serration”, which is also called as the PLC effect. The PLC effect has been receiving great attention since both works; One by A. Le Chatelier [8] who reported repetitive plastic oscillations in mild steels at elevated temperatures, the other one [9-10] by A. Portevin and F. Le Chatelier, who observed serration in aluminum alloys at different deformation rates. It is generally accepted that the PLC effect is the result from a temporal process called as DSA process, which is the repetitive dynamic response between solute atoms and the mobile dislocations. Also, the temporal process induces heterogeneous deformation features in materials. The feature is shown as a localized deformation band, which is commonly called as the “PLC band”. It has been reported that the spatio-temporal coupling process significantly affects mechanical properties of the materials under the PLC effect; On the one hand, the PLC effect is detrimental to ductility, formability, [11-12] and low fatigue life [13-14]. On the other hand, it has a beneficial effect on fracture toughness [15].

1.2.1 Phenomenology

In uniaxial tensile test, the specimen is deformed at a constant strain rate determined by the crosshead speed. At a time, the total strain, ε_{total}, is composed of two strain components, the plastic strain, ε_p, and the elastic strain, ε_e of the machine-specimen system.

$$\varepsilon_{total} = \varepsilon_e + \varepsilon_p \qquad (1\text{-}1)$$

$$\dot{\varepsilon}_{total} = \dot{\varepsilon}_e + \dot{\varepsilon}_p \qquad (1\text{-}2)$$

And, the elastic strain can be replaced by the followings.

$$\dot{\varepsilon}_{total} = \frac{\dot{\sigma}}{E} + \dot{\varepsilon}_p \qquad (1\text{-}3)$$

Where σ is the stress and E the elastic modulus of the specimen-machine system. The load drops associated with serration when the plastic strain rate, $\dot{\varepsilon}_p$ exceeds the imposed applied strain rate $\dot{\varepsilon}_{total}$. The plastic strain is the derivative of the plastic strain with time, as the following equations (1-4) and (1-5).

$$\varepsilon_p = \rho_m b x \qquad (1\text{-}4)$$

$$\frac{d\varepsilon_p}{dt} = \frac{d\rho_m}{dt} b\bar{x} + \rho_m b \frac{d\bar{x}}{dt} \qquad (1\text{-}5)$$

where ρ_m is the mobile dislocation density, $\bar{x}$ the average displacement by deformation and b the Burgers vector. The derivative of $\bar{x}$ with time, $d\bar{x}/dt$ is equal to the average dislocation velocity, $\bar{v}$. Thus, serration will therefore occur whenever there is an instantaneous variation in ρ_m or in $\bar{v}$, or in both.

1.2.2 Types of serrations

The serration behavior in stress-strain curves is observed in various morphologies depending on the test conditions, temperature, and the applied strain rate [16-23]. In Rodriguez's review paper [24], serrations are classified into five types, as shown in **Fig. 1.1**. At higher strain rates or lower temperatures, A-type serration occurs, which is characterized by periodic stress peaks followed by a drop to the general level of the stress–strain curve. In C-type serration, stress initially drops, and then rises to the general level of stress at lower strain rates or higher temperatures. As the intermediate condition, B-type serration with stress oscillation becomes visible around the general level of stress.

D- and E-types are shown in special cases; D-type serration are plateaus in the stress-strain curve with no work-hardening, while E-type serration is sometimes shown after A-type serration at high strains with little or no work hardening.

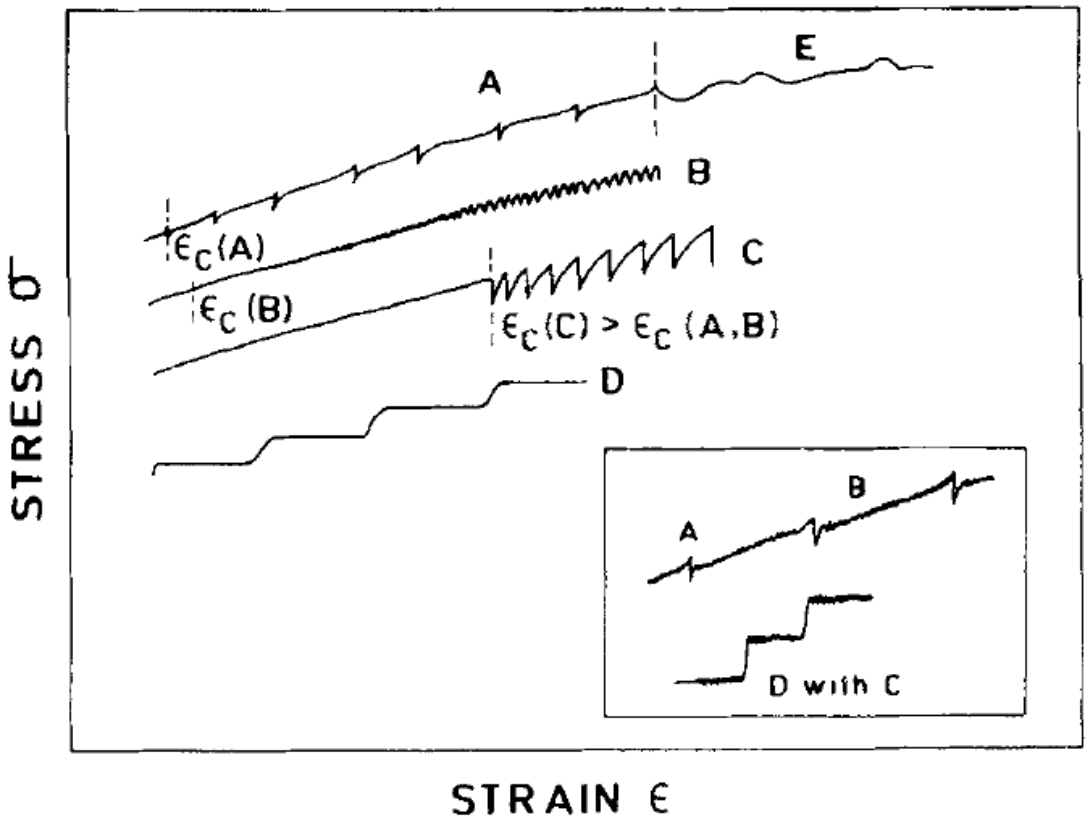

Figure 1.1 Types of serrations [24]

1.3 Dynamic Strain Aging (DSA)

It is generally accepted that DSA manifests the PLC effect [25-26]. DSA is the dynamic interaction between mobile dislocation and solute atoms during plastic deformation in solid-solution alloys [2-6]. In DSA, solute atoms can diffuse to dislocations that are temporarily arrested at obstacles, such as dislocation junctions, grain boundaries, and precipitates, resulting in the pinning of mobile dislocations, i.e., the formation of a Cottrell atmosphere [7]. It causes a reduction in the mobile dislocation density and the increment in flow stress, because fewer dislocations move faster to accommodate an applied strain rate. Eventually, the pinned dislocations are suddenly reactivated owing to depinning of the solute atoms, resulting in a transient drop in the flow stress. This series of processes originating from DSA are continuously repeated as long as the diffusion process is effective. Since DSA is the dynamic reaction affected by the velocity of moving dislocations and diffusion rate of the solute atoms, the DSA behavior sensitively varies depending on the several factors influencing them.

1.3.1 The physical model for DSA

McCormick [3] suggested a DSA model based on the Cottrell theory [7]. The DSA model for the onset of serrated flow suggests that solute atmospheres form by dislocations moving at less than a critical velocity, v_c, given by

$$v_c \simeq \frac{4D}{l}. \qquad (1\text{-}6)$$

Where D is the solute diffusion coefficient and l is the effective radius of the atmosphere. The radius l is equal to $U_m b/kT$ where U_m is the solute-dislocation binding energy in eV, b the Burgers vector, k the Boltzmann constant, and T the temperature. Initially, D is too small for solute atmosphere to form. The solute atmosphere associated with DSA process can be achieved not only by enhanced diffusion process through the increase in the dimensionless vacancy concentration, C_v, but also by the decrease in the dislocation velocity with increasing strain. Regarding the total dislocation density, $\rho \propto \rho_m$ in Eq. (1-5), Eq. (1-6) may be rewritten in terms of the vacancy concentration and total dislocation density, ρ, as

$$\dot{\varepsilon} = \frac{d\rho}{dt} b\bar{x} + \frac{4\rho b C_v D_0 exp\left(-\frac{Q_m}{kT}\right)}{l}. \qquad (1\text{-}7)$$

Where D_0 is the diffusion frequency factor, and Q_m is the effective activation energy in eV for solute diffusion. The increase in C_v and ρ by straining are expressed by the following equations.

$$C_v = H\varepsilon^m \qquad (1\text{-}8)$$

$$\rho = N\varepsilon^\beta \qquad (1\text{-}9)$$

Inserting both equations into Eq. (1-7) gives the following form.

$$\dot{\varepsilon} = N\beta\varepsilon^{\beta-1}\dot{\varepsilon}\, b\bar{x} + \frac{4N\varepsilon^\beta H\varepsilon^m b D_0}{l} exp\left(-\frac{Q_m}{kT}\right) \qquad (1\text{-}10)$$

Regarding $4bNHD_0/l = 1/Z$, Eq. (1-10) can be rewritten as

$$(\varepsilon^{\mathrm{DSA}})^{(m+\beta)} = (1 - N\beta\varepsilon^{\beta-1} b\bar{x}) Z\dot{\varepsilon}\, exp\left(\frac{Q_m}{kT}\right). \qquad (1\text{-}11)$$

In Eq. (1-11), $\varepsilon^{\mathrm{DSA}}$ is the critical strain for the onset of serrated flow. Also, the value of $(1 - N\beta\varepsilon^{\beta-1} b\bar{x})$ on the right-hand side can be considered as the constant, S, since the $\beta \cong 1$ [3, 29] and $\varepsilon > 0$. Thus, S mostly depends on $Nb\bar{x}$. The final form is as the below equation (1-12).

$$(\varepsilon^{\mathrm{DSA}})^{(m+\beta)} = SZ\dot{\varepsilon}\, exp\left(\frac{Q_m}{kT}\right) \qquad (1\text{-}12)$$

Eq. (1-12) says that the critical strain, $\varepsilon^{\mathrm{DSA}}$, decreases with increasing temperature, T, and with decreasing strain rate, $\dot{\varepsilon}$, and the activation energy, Q_m. The decrement in the critical strain means DSA process becomes more activated. We can track the type of the potential atoms for DSA by calculating the exponent value, $(m + \beta)$. The diffusion process through vacancy concentration is enhanced only if the potential atoms for DSA are substitutional atoms, and thereby the $(m + \beta)$ is higher in case of substitutional atoms than interstitial atoms. The value is reported to be around 2 for substitutional atoms, and around 1 for interstitial atoms [3].

1.4 Motivation and objective of this study

Although the general importance of DSA in the PLC effect has been clearly identified in many previous reports [25-26], there are still unclear for (1) how the microscopic (or atomic) solute atom-dislocation interactions results in the macroscopic serrated flow in stress-strain curve, (2) How materials behave in the intermediate scale (mesoscale) under the PLC effect, (3) How the PLC effect affects mechanical properties of materials

In this study, as motivated by these viewpoints, meso- & micro-scopic deformation behavior under the PLC effect was investigated in an Fe-19Cr-13Ni-0.2C stable austenitic stainless steel. Interestingly, it was found that this material has two temperature ranges showing DSA, such as “low-temperature DSA” from 473 K to 623 K and “high-temperature DSA” above 723 K. Thus, controlling mechanism of DSA was discussed in chapter 2 for the high-temperature DSA, and in chapter 3 for the low-temperature DSA, respectively.

In chapter 2, high-temperature PLC effect was characterized using high-temperature Digital Image Correlation (DIC) analysis during tensile testing. Correlation between macroscopic serration behavior and mesoscopic localized deformation band (referred to

as the PLC band) was clarified. Then, necking behavior under A-type PLC effect was discussed in terms of DSA process.

In chapter 3, various types of serrated flow were investigated in terms of propagation of the PLC band. For this, a numerical simulation based on dislocation dynamics was modelled for the PLC effect. Then, dynamic transition behavior of serrated flow was discussed.

Also, the PLC effect may vary not only with testing conditions but also with microstructural factors [16, 27-30] since DSA process is dependent on microstructural factors.

In chapter 4, effects of grain size and replacement of C by N on the PLC effect at high-temperature DSA region were investigated in terms of serration behavior and the PLC band characteristics.

In chapter 5, several results in each chapter were summarized.

1.5 References

[1] K.H. Lo, C.H. Shek, and J.K.L. Lai, Recent developments in stainless steels, Mat. Sci. Eng. R 65 (2009) 39-104.

[2] A.H. Cottrell, A note on the Portevin-Le Chatelier effect, Phil. Mag. 44 (1953) 829-832.

[3] P.G. McCormick, A model for the Portevin-Le Chatelier effect in substitutional alloys, Acta Metall. 20 (1972) 351-354.

[4] A. van den Beukel, Theory of the effect of dynamic strain ageing on mechanical properties, Phys, Status Solidi A 30 (1975) 197-206.

[5] A. van den Beukel, On the mechanism of serrated yielding and dynamic strain ageing, Acta Metall. 28 (1980) 965-969.

[6] P.G. McCormick, Dynamic strain ageing, Trans. Indian Inst. Met. 39 (1986) 98-106.

[7] A.H. Cottrell and B.A. Bilby, Dislocation theory of yielding and strain ageing of iron, Proc. Phys. Soc. A 62 (1949) 49-62.

[8] A. Le Chatelier, Influence du temps et de la température sur les essais au choc, Revue de Metallurgie 6 (1909) 914-917.

[9] A. Portevin and F. Le Chatelier, Sur un phénomène observé lors de l'essai de traction d'alliages en cours de transformation, Compt. Rend. Acad. Sci. Paris 176 (1923) 507-510.

[10] A. Portevin and F. Le Chatelier, Heat treatment of aluminium-copper alloys, in: Transaction of the American Society of Steel Treating, Vol. 5, 1924, pp. 457-478.

[11] V.A. Phillips, A.J. Swain, and R. Eborall, Yield point phenomena and stretcher-strain markings in aluminium-magnesium alloys, J. Inst. Metals 81 (1953) 625-647.

[12] K. Chihab, Y. Estrin, L.P. Kubin, and J. Vergnol, The kinetics of the Portevin-Le Chatelier bands in an Al-5at%Mg alloy, Scr. Metall. 21 (1987) 203-208.

[13] S. Herenu, I. Alvarez-Armas, and A.F. Armas, The influence of dynamic strain aging on the low cycle fatigue of duplex stainless steel, Scr. Mater. 45 (2001) 739-745.

[14] J.H. Wu and C.K. Lin, Effect of strain rate on high-temperature low-cycle fatigue of 17-4 PH stainless steels, Mat. Sci. Eng. A 390 (2005) 291-298.

[15] Y. Estrin and L.P. Kubin, Spatial coupling and propagative plastic instabilities, in: Continuum models for materials with microstructure, John Wiley & Sons, 1995, pp. 395-450.

[16] D.W. Kim, W.S. Ryu, J.H. Hong, and S.K. Choi, Effect of nitrogen on the dynamic

strain ageing behaviour of type 316L stainless steel, J. Mater. Sci. 33 (1998) 675-679.

[17] D.W. Kim, W.G. Kim, and W.S. Ryu, Role of dynamic strain aging on low cycle fatigue and crack propagation of type 316L(N) stainless steel, Int. J. Fatigue 25 (2003) 1203-1207.

[18] S.G. Hong and S.B. Lee, Mechanism of dynamic strain aging and characterization of its effect on the low-cycle fatigue behavior in type 316L stainless steel, J. Nucl. Mater. 340 (2005) 307-314.

[19] L.J. Meng, J. Sun, H. Xing, and G.W. Pang, Serrated flow behavior in AL6XN austenitic stainless steel, J. Nucl. Mater. 394 (2009) 34-38.

[20] I. Nikulin and R. Kaibyshev, Deformation behavior and the Portevin-Le Chatelier effect in a modified 18Cr-8Ni stainless steel, Mater. Sci. Eng. A 528 (2011) 1340-1347.

[21] V. Ganesan, K. Laha, M. Nandagopal, P. Parameswaran, and M.D. Mathew, Effect of nitrogen content on dynamic strain ageing behaviour of type 316LN austenitic stainless steel during tensile deformation, Mater. High Temp. 31 (2014) 162-170.

[22] B.K. Choudhary, Activation energy for serrated flow in type 316L(N) austenitic stainless steel, Mater. Sci. Eng. A 603 (2014) 160-168.

[23] A.S. Alomari, N. Kumar, and K.L. Murty, Serrated yielding in an advanced stainless steel Fe-25Ni-20Cr (wt%), Mater. Sci. Eng. A 751 (2019) 292-302.

[24] P. Rodriguez, Serrated plastic flow, Bull. Mater. Sci. 6 (1984) 653-663.

[25] E. Rizzi and P. Hahner, On the Portevin-Le Chatelier effect: theoretical modeling and numerical results, Int. J. Plast. 20 (2004) 121-165.

[26] A. Yilmaz, The Portevin-Le Chatelier effect: A review of experimental findings, Sci. Tech. Adv. Mater. 12 (2011) 063001.

[27] W. Charnock, The influence of grain size on the nature of portevin-lechatelier yielding, Phil. Mag. 18 (1968) 89-99.

[28] B.J. Brindley and P.J. Worthington, Serrated yielding in aluminium-3%magnesium, Acta Metall. 17 (1969) 1357-1361.

[29] S. Miura and H.Yamauchi, Influence of grain size on the Portevin-LeChatelier effect in Al-Mg alloys, Trans. JIM 13 (1972) 82-88.

[30] P.G. McCormick, Effect of grain size on serrated yielding in an Al-Mg-Si alloy, Phil. Mag. 23 (1971) 949-956.

Chapter 2

Macroscopic and Microscopic Characterizations of the Portevin-Le Chatelier Effect in Austenitic Stainless Steel using High-Temperature Digital Image Correlation Analysis

2.1 Introduction

Austenitic stainless steel (γ-STS) has been widely used for various applications in a wide temperature range. At an elevated temperature, the stress-strain curve of γ-STSs shows serrated flow [1-4]. It has been reported that the serrated flow in γ-STSs is closely related to dynamic strain aging (DSA) [5]. The high-temperature mechanical properties of γ-STSs are very sensitive to aspects such as the alloying elements and concentrations, temperature, and strain rate [6-13].

Meanwhile, DSA is also accompanied with a strain localization. The deformation of the gauge part of a tensile specimen is highly localized in a band shape; thus, the "PLC band" develops. Recently, the PLC band has been characterized by mapping the strain and strain rate distributions using digital image correlation (DIC) analysis. Thus, the PLC effect has been actively investigated by observing the PLC band during tensile testing in various metallic alloys [14-19]. However, the characterization of the PLC band with regard to DSA tends to be limited at room temperature in various alloys, such as Al-Mg alloys and Fe-Mn-C austenitic TWIP steels [14-20]. Meanwhile, there have been few studies on high-temperature PLC band characteristics in γ-STS, even though its high-

temperature mechanical properties are significantly affected by the DSA associated with the PLC effect [6-13]. To further understand the PLC effect and better control the mechanical properties of γ-STSs, it is necessary to investigate the PLC band characteristics at high temperatures where DSA occurs. In this chapter, DIC analysis for high-temperature tensile testing was carried out under various testing conditions using γ-STS to investigate the PLC effect from macroscopic and microscopic viewpoints. Further, the local strain development by the A-type PLC band and the criterion of necking deformation related to this were discussed.

2.2 Experimental

2.2.1 Material

The stable γ-STS, Fe-19Cr-13Ni-0.2C in mass%, was used in this study. The chemical composition is detailed in **Table 2.1**. To obtain a fully recrystallized austenite single-phase structure, a cold-rolled plate of 2 mm thickness was solution-treated at 1473 K for 3.6 ks, followed by water-cooling. The solution-treated material had an equiaxial-grained austenitic structure with an average grain size of 67 μm, as shown in **Fig. 2.1**.

2.2.2 Tensile Testing

For tensile testing, a plate-shaped test-piece with a gauge part of $50^{l} \times 10^{w} \times 2^{t}$ mm^3 in volume was machined from the solution-treated material by an electro-discharge machine. The surface of the test-piece was mechanically polished to eliminate the damaged layer induced during machining. Next, high-temperature tensile testing was carried out using an Instron-type tensile testing machine equipped with a heating furnace (AG-100KNG/RX and TCH-220PSP, Shimadzu Corp.) at temperatures from 723 K to 823 K under varying applied strain rates from 10^{-4} s^{-1} to 10^{-2} s^{-1}. Although it took

approximately 5.4 ks to attain the testing temperature, it was confirmed that no precipitates were formed after the tensile testing.

2.2.3 DIC analysis

The tensile deformation behavior was captured digitally with 2752 × 2200 pixels with sufficient high-time resolution (~ 1/7 fps) using a three-dimensional camera system, ARAMIS 3D, developed by GOM. Next, the strain distributions and strain rate were analyzed by the DIC software, GOM Correlate Professional. Because random patterns are required for digital image tracking in DIC analysis, the gauge part of the tensile test piece was decorated by heat-resistant black-and-white sprays before the testing to form a speckle pattern. The positional relations between the tensile testing machine, test piece and, DIC camera system, and the decorated tensile test piece are shown in **Fig. 2.2**. For the DIC analysis, the subset was set to be a square with 19 × 19 pixels, which corresponds to an area of approximately 1140 × 1140 μm^2. The high-temperature DIC system enables analysis of the in situ tensile deformation behavior even at a high temperature of 873 K. The strain can be three-dimensionally analyzed in a tensor by DIC, and then evaluated as the nominal strain in the tensile direction. The strains were globally and locally measured

as $\varepsilon^{\text{DIC-G}}$ and $\varepsilon^{\text{DIC-L}}$, respectively. $\varepsilon^{\text{DIC-G}}$ indicates the macroscopic average strain throughout the gauge part of a tensile test piece, while $\varepsilon^{\text{DIC-L}}$ is the microscopic strain calculated from a subset, such as to evaluate the strain in a PLC band. Meanwhile, the strain evaluated from the displacement of the crosshead of the tensile machine, ε^{C}, was also considered, because the usage of a strain gauge is generally highly limited in high-temperature testing. The critical strain referring to the localization of plastic flow was measured as the onset strain for serrated flow in the tensile curve, ε^{DSA}. All the strain measurements were conducted on the central line of the gauge part parallel to the tensile axis.

Table 2.1 Chemical composition of the Fe-19Cr-13Ni-0.2C austenitic stainless steel used in this study

	Cr	Ni	Mn	Si	P	S	C	N	Fe
wt.%	19.3	13.5	0.8	0.04	0.004	0.0006	0.208	0.004	Bal.

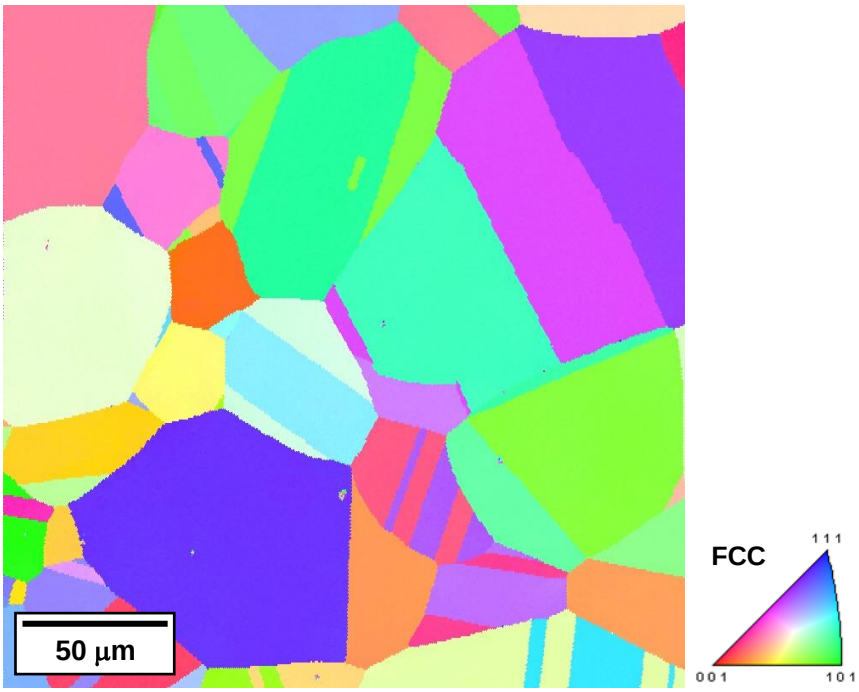

Figure 2.1 Inverse pole figure (IPF) map for the initial microstructure of an Fe-19Cr-13Ni-0.2C austenitic stainless steel.

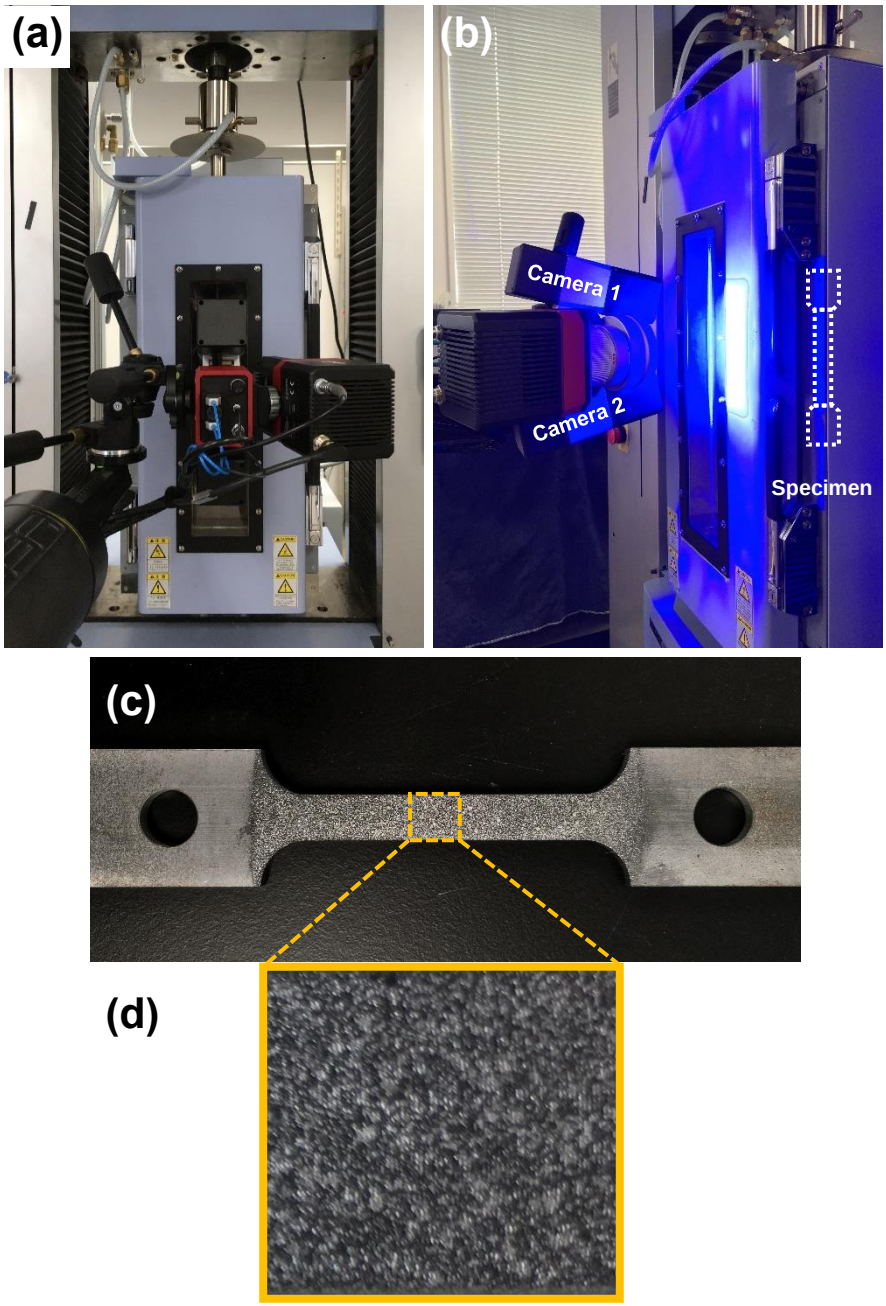

Figure 2.2 High-temperature digital image correlation (DIC) analysis system; (a) Front view and (b) side view showing the positional relationship between the DIC camera system and tensile testing machine; (c) A tensile test piece decorated by heat-resistant black-and-white sprays, and (d) the magnified image of the gauge part showing a speckle pattern.

2.3 Results and discussion

2.3.1 Macroscopic characterization of high-temperature PLC effect

2.3.1.1 Evaluation of high-temperature tensile property by DIC

The stress-strain curves obtained by high-temperature tensile testing under various conditions are shown in **Fig. 2.3**. In these curves, ε^{C} and $\varepsilon^{DIC\text{-}G}$ represent the engineering strains in (a) and (b), respectively. Clearly, ε^{C} **(a)** was overestimated when compared with $\varepsilon^{DIC\text{-}G}$ **(b)**, and the overestimation of the strain in ε^{C} was approximately 20% under all conditions. When a crosshead is moved at a constant speed, v_c, the total displacement of testing system, d_{total}, at a given time t is obtained by the product of v_c and t, and is also described by the sum of three components: the elastic displacement of the testing machine, d_e^m; and the elastic and plastic displacements of the specimen, d_e^s and d_p^s, respectively, as follows;

$$d_{total} = v_c t = d_e^m + d_e^s + d_p^s = \frac{P}{K} + \left(\varepsilon_e^s + \varepsilon_p^s\right)L \qquad (2\text{-}1)$$

Here, P, K, ε_e^s, ε_p^s, and L indicate the load, stiffness of the testing machine, elastic and plastic strains of the specimen, and initial gauge length, respectively. Given that the

apparent total strain of the tensile testing system, d_{total}/L, and the total strain of the specimen, $\varepsilon_{total}^{s} = \varepsilon_{e}^{s} + \varepsilon_{p}^{s}$, correspond to ε^{C} and $\varepsilon^{DIC\text{-}G}$, respectively, the considerable difference between ε^{C} and $\varepsilon^{DIC\text{-}G}$ reveals that $d_{e}^{m} = P/K$ is considerably large and hence, cannot be ignored due to the decreasing K at high temperature; i.e., high-temperature DIC analysis is effective to accurately measure only the strain of the specimen. Thus, we adopted the strain evaluated using DIC analysis as the representative of the engineering strain in the subsequent evaluations.

On the other hand, a serrated flow associated with plastic instability was observed in all stress-strain curves. **Fig. 2.4** shows the magnified curves corresponding to the boxed segment in (b). As reported in the most recent studies, the PLC band is essentially classified into three types in accordance with its characteristics related to serrated flow and band propagation as follows [19-21]: (1) A-type, where individual PLC bands propagate continuously in the gauge part of a specimen, and the flow stress is periodic and characterized by an abrupt rise, followed by a drop to the general level of the stress curve; (2) B-type, where PLC bands propagate discontinuously through the nucleation of a new band near the previous bands, and the flow stress appears to oscillate about the general level of the stress curve; and (3) C-type, where PLC bands are randomly nucleated

and non-propagating, and the flow stress drops abruptly below the general level of the flow curve. According to this classification, Fig. 2.4 reveals that the B-type serrated flow with a slight A-type flow occurred under the condition of 823 K/10^{-4} s^{-1}, whereas single A-type serrated flow occurred under other conditions. The critical strain, ε^{DSA}, is marked by black arrows. Further, ε^{DSA} decreases with increasing temperature and decreasing applied strain rate. Considering that the plastic instability is closely related to DSA in γ-STS, the tendency could be explained in terms of DSA; the diffusion of solute atoms to the temporarily arrested dislocations is accelerated by increasing temperature and decreasing strain rate, and thus, serrated flow occurs at a lower strain. In the same manner, a negative strain rate sensitivity was observed at 773 K, where the material had higher flow stress at a lower strain rate of 10^{-4} s^{-1} rather than at a higher strain rate of 10^{-3} s^{-1}. The negative strain-rate-sensitivity behavior was also exhibited by decreasing the strain rate from 5 × 10^{-3} s^{-1} to 10^{-3} s^{-1} at 823 K; this behavior consequently diminished, accompanying the change in the serrated flow to B-type at the lowest strain rate of 10^{-4} s^{-1}.

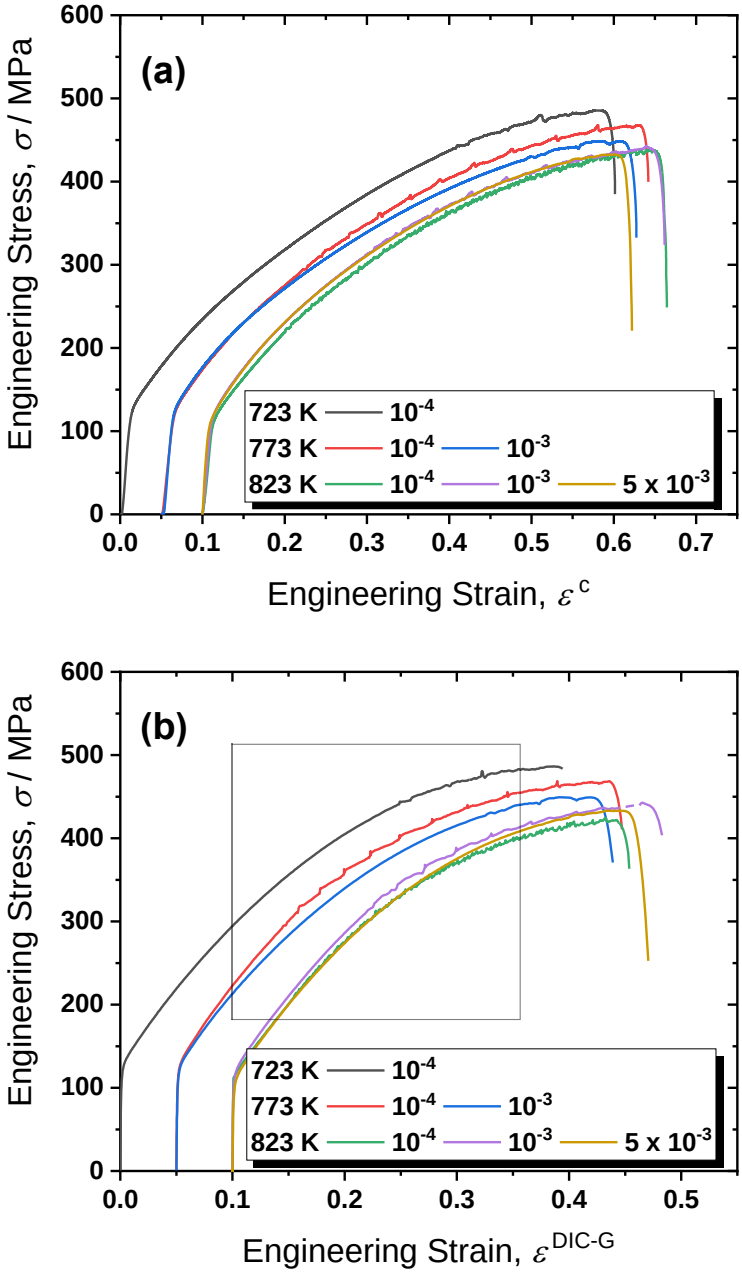

Figure 2.3 Engineering stress-strain curves of specimens tested at varying temperatures and strain rates. The strain was converted by (a) the displacement of the tensile testing machine and by (b) DIC analysis**.**

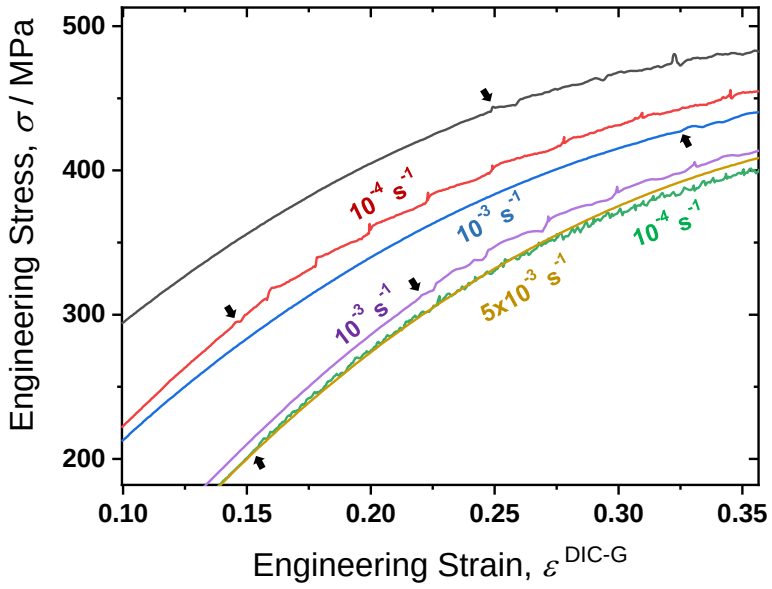

Figure 2.4 Magnified image of the boxed segment in Fig. 2.3(b)

2.3.1.2 Macroscopic strain rate variation associated with PLC band propagation

According to Eq. (2-1), the total strain of a specimen, ε^{s}_{total}, is described as

$$\varepsilon^{s}_{total} = \varepsilon^{s}_{e} + \varepsilon^{s}_{p} = \frac{v_c t}{L} - \frac{P}{KL} \qquad (2\text{-}2)$$

By differentiating Eq. (2-2) with t, the total strain rate of the specimen, $\dot{\varepsilon}^{s}_{total}$, can be expressed by Eq. (2-3) with the apparent nominal stress, σ^{m}, and the initial area, A^{m}, of the testing machine ($P = A\sigma$).

$$\dot{\varepsilon}^{s}_{total} = \frac{v_c}{L} - \frac{A}{KL}\dot{\sigma}^{m} \qquad (2\text{-}3)$$

Here, $\dot{\sigma}^{m}$ is the apparent nominal stress rate of the testing machine. Eq. (2-3) can be simply expressed with $M = A^{m}/KL$, as below.

$$\dot{\varepsilon}^{s}_{total} = \frac{v_c}{L} - M\dot{\sigma}^{m} \qquad (2\text{-}4)$$

If M is negligibly small, it is understood from Eq. (2-4) that $\dot{\varepsilon}^{s}_{total}$ should be constant at v_c/L under a conventional testing condition with relatively low $\dot{\sigma}^{m}$. **Fig. 2.5(a)** shows the change in $\varepsilon^{DIC\text{-}G}$ as a function of t under 773 K/10^{-4} s^{-1}, where the A-type PLC effect occurs. The slope of the curve indicates the mean strain rate of the gauge part of the

specimen, $\dot{\varepsilon}^{\text{DIC-G}}$, in this figure. The area surrounded by the dashed line is magnified in **Fig. 2.5(b)**, and the nucleation of each PLC band, which was identified by DIC analysis as mentioned later, is indicated by the black arrow. At a lower strain than the critical strain for the 1st PLC band nucleation, $\dot{\varepsilon}^{\text{DIC-G}}$ was calculated to be approximately 6×10^{-5} s^{-1}, which is considerably lower than the applied strain rate of 10^{-4} s^{-1} shown by the red line in (a). In addition, it is interesting that $\dot{\varepsilon}^{\text{DIC-G}}$ discontinuously increased stepwise after each nucleation of the PLC bands and, finally, was equal to the applied strain rate of 10^{-4} s^{-1}, as shown in **Fig. 2.6**. These results suggest that $M\dot{\sigma}^{m}$ in Eq. (4) is considerably large at the early stage of deformation and becomes smaller by repeated PLC band propagation due to the lowering $\dot{\sigma}$. In other word, from the macroscopic point of view, when $\dot{\sigma}$ becomes small, the strain was limited in the gauge part of the tensile test piece, resulting in ductile fracture with a necking deformation, i.e., the beginning of necking deformation can be explained by the conventional plastic instability condition.

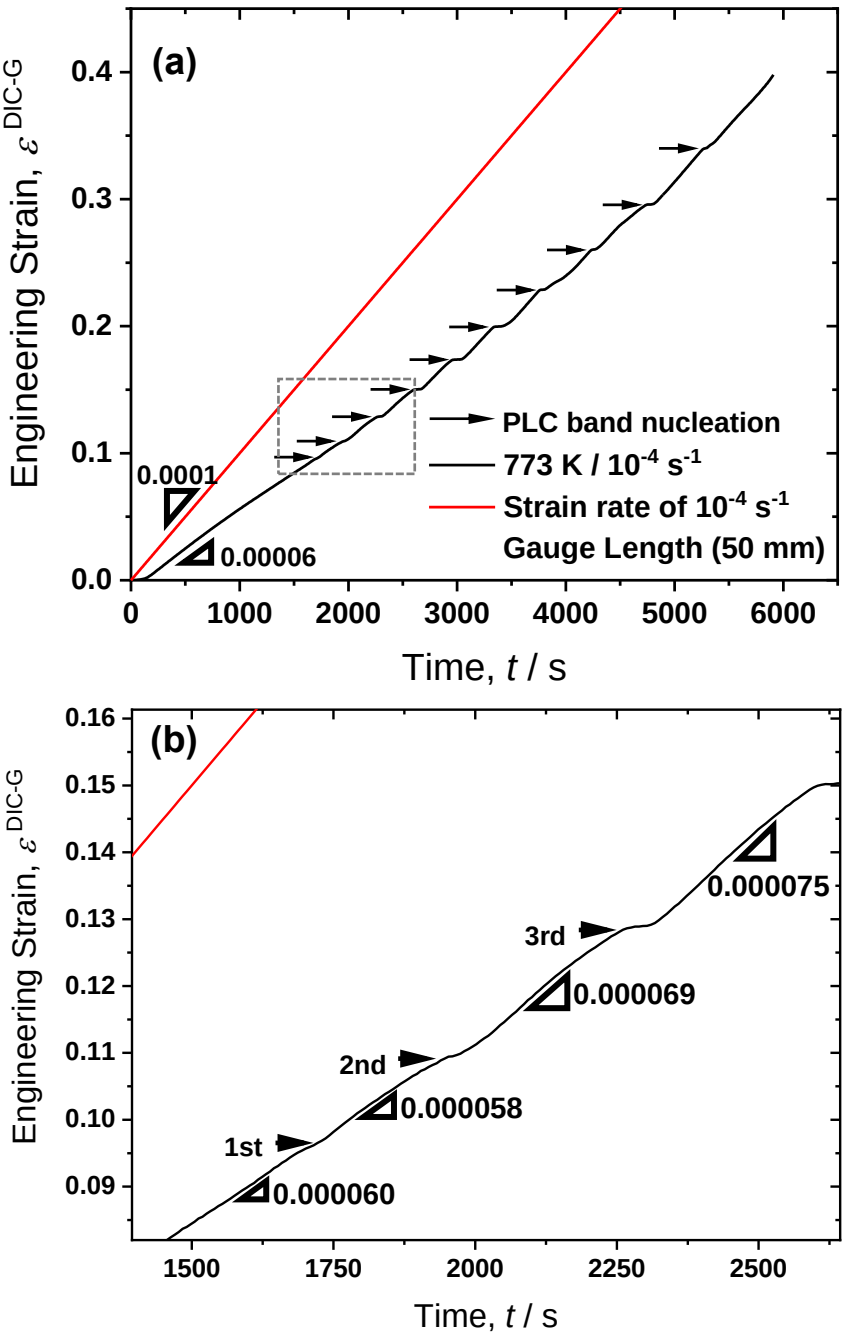

Figure 2.5(a) Change in global strain of a gauge part ε^{DIC-G}; The boxed segment in (a) is magnified in (b), and each black arrow indicates the strain that a PLC band nucleates with.

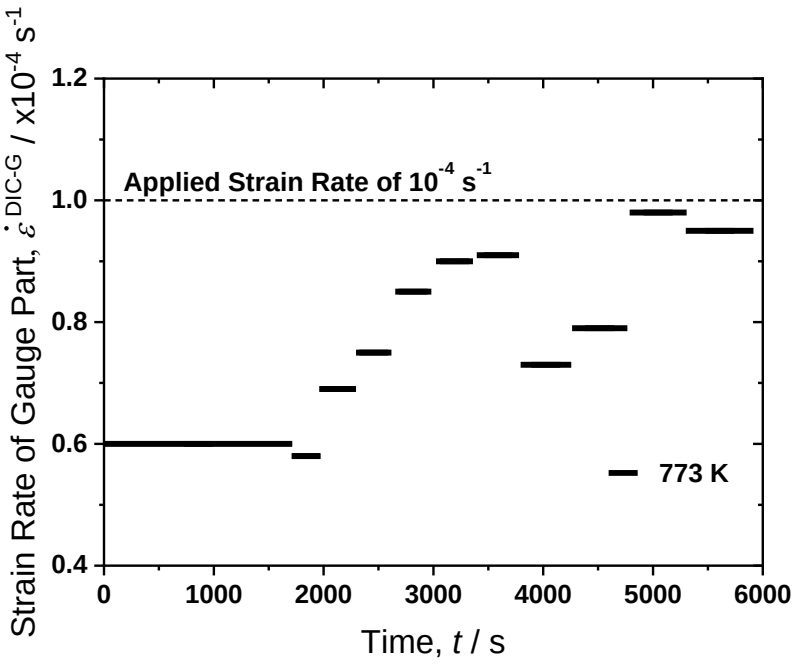

Figure 2.6 Global strain rate $\dot{\varepsilon}^{DIC-G}$ as a function of time under 773 K/10^{-4} s^{-1}.

2.3.1.3 Control mechanism of dynamic strain aging in austenitic stainless steel

In the physical model for DSA, the critical strain, ε^{DSA}, is expressed by the following equation [22].

$$(\varepsilon^{DSA})^{m+\beta} = SZ\,\dot{\varepsilon}\,exp\left(\frac{Q}{RT}\right) \qquad (2\text{-}5)$$

Here, S and Z are constants, and Q, R, and T are the activation energy for the diffusion of solute atoms in J/mol, the gas constant (8.314 J/(mol × T)), and the absolute temperature, respectively. In addition, m and β denote the exponents related to the vacancy concentration and dislocation density in solids, respectively. In the following calculation, $\varepsilon^{DIC\text{-}G}$ and $\dot{\varepsilon}^{DIC\text{-}G}$ at the onset of the serrated flow in the tensile curves were regarded as ε^{DSA} and $\dot{\varepsilon}$ in Eq. (2-5) to consider the critical condition where the PLC effect appears. **Fig. 2.7(a)** shows the relation between $ln\ \dot{\varepsilon}$ and $ln\ \varepsilon^{DSA}$ at 823 K. The slope represents ($m + \beta$) and was evaluated to be 2.42. It has been reported [21,23-24] that ($m + \beta$) ranges from 0.5 to 1 for the diffusion of the interstitial atom and from 2 to 3 for the diffusion of the substitutional atom. Therefore, it can be inferred that the DSA above 723 K in an Fe-19Cr-13Ni-0.2C γ-STS is closely related to the diffusion of the substitutional atom. The relation between $ln\ \varepsilon^{DSA}$ and $1/T$ is also displayed in **Fig. 2.7(b)** at an applied strain rate

of 10^{-4} s^{-1}, where the slope corresponds to the $1/(m + \beta) \times Q/R$ value. Inserting the values of $(m + \beta)$ and R yielded a Q of 183 kJ/mol. In previous studies, the activation energy for the bulk diffusion of the substitutional Cr atom in austenite was reported to be approximately 400 kJ/mol [8,25]. It has been reported that substitutional solutes can diffuse along the dislocation core with 0.4-0.7 times the activation energy for bulk diffusion [26]. Solute atmospheres form on forest dislocations, and then move to temporarily arrested mobile dislocations through pipe diffusion [27-28]. Hong *et al.* [9] have suggested that the pipe diffusion of substitutional Cr atoms with an activation energy of 182.2–205.3 kJ/mol resulted in serration at a higher temperature in cold-worked 316L γ-STS, which agrees well with the present result. Thus, it can be concluded that DSA occurs in an Fe-19Cr-13Ni-0.2C γ-STS above 723 K and results from the interaction between the dislocations and the pipe diffusion of substitutional Cr atoms.

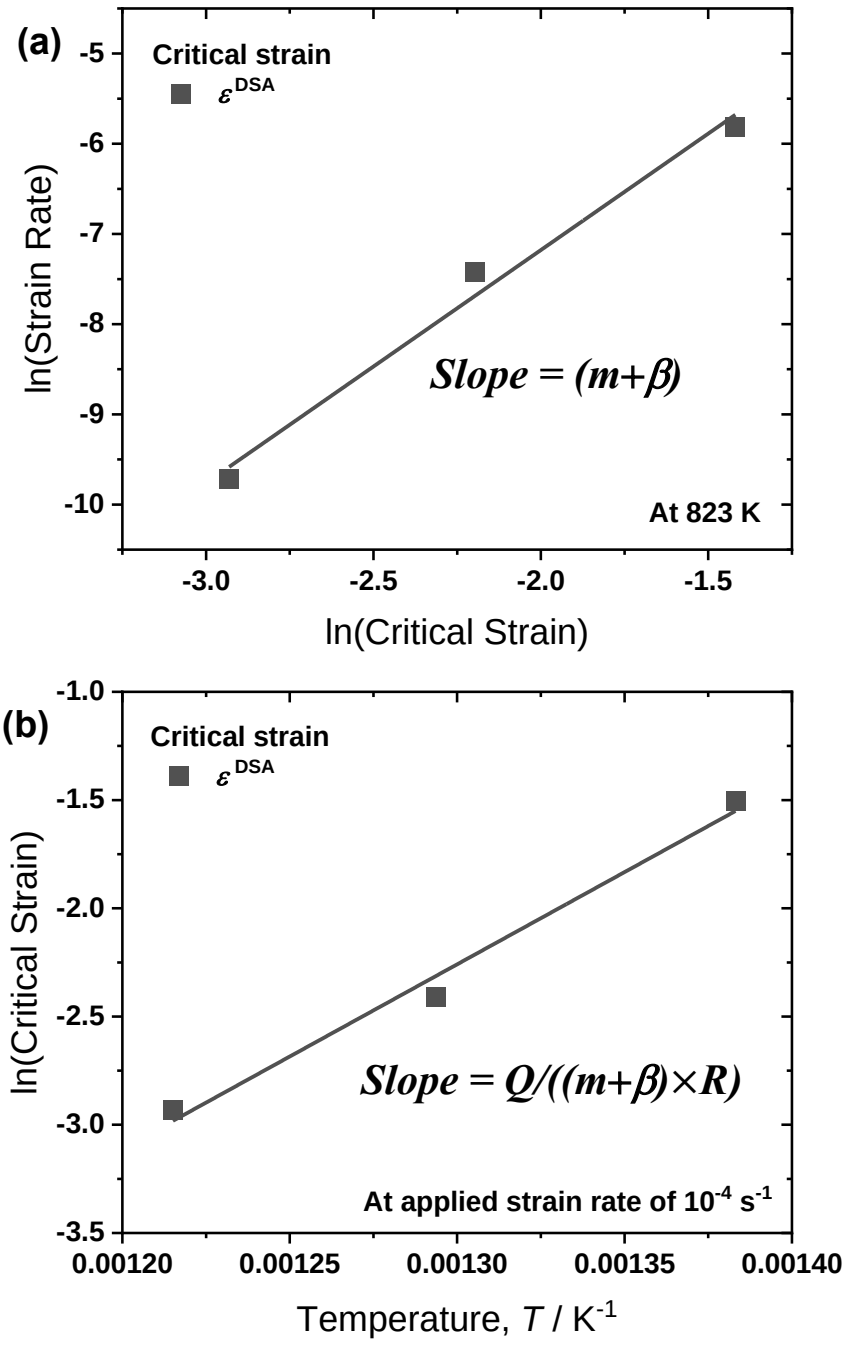

Figure 2.7(a) $ln\ \dot{\varepsilon}^{DIC\text{-}G}$ vs $ln\ \varepsilon^{DIC\text{-}G}$ at 823 K and (b) $ln\ \varepsilon^{DIC\text{-}G}$ and $1/T$ at the applied strain rate of 10^{-4} s^{-1}. $\dot{\varepsilon}^{DIC\text{-}G}$ and $\varepsilon^{DIC\text{-}G}$ were measured by DIC analysis at the onset of the initial PLC band nucleation.

2.3.2 Microscopic characterization of high-temperature PLC band

2.3.2.1 Type variation of high-temperature PLC band in terms of band propagation behavior

Fig. 2.8(a) and **(b)** show the magnified image of the tensile curves showing serrated flow and the strain rate map acquired at 773 K under the applied strain rate of 10^{-4} s^{-1} (red curve), respectively. The series of DIC images correspond to the black arrows are in Fig. 2.8(a). Clearly, a typical A-type PLC band was developed; a PLC band nucleated at an edge of the gauge part, and then propagated toward the opposite edge. It was also confirmed that all features indicating the development of an A-type PLC band tended to recur as the PLC bands propagated in an identical direction along the gauge part. **Fig. 2.9(b)** and **(c)** show DIC images indicating the serrated flow in the red boxed segments (b) and (c) under 823 K/10^{-4} s^{-1} (green curve) in **Fig. 2.9(a)**, respectively. Although a PLC band propagated along the gauge part similarly to the A-type PLC band as shown in Fig. 2.8, the propagation behavior was clearly different; a new PLC band was nucleated near the previous one in Fig. 2.9(b), and the newly formed PLC band was immobile and then diminished in Fig. 2.9(c), which is a typical characteristic of B-type PLC bands. The

difference in the propagation behaviors between A-type and B-type PLC bands (Fig. 2.8 and 2.9), visualized by high-temperature DIC analysis, corresponds to the difference in serrated flow in the stress-strain curves (Fig. 2.3). The overall feature of the high-temperature PLC band observed in γ-STS is the same as that of the PLC band formed in other alloys at room temperature [14-21]. Subsequently, the characteristics of the A-type PLC band were analyzed in more detail considering the strain development by the PLC band, while those of B-type and C-type PLC bands were discussed in detail in chapter 3.

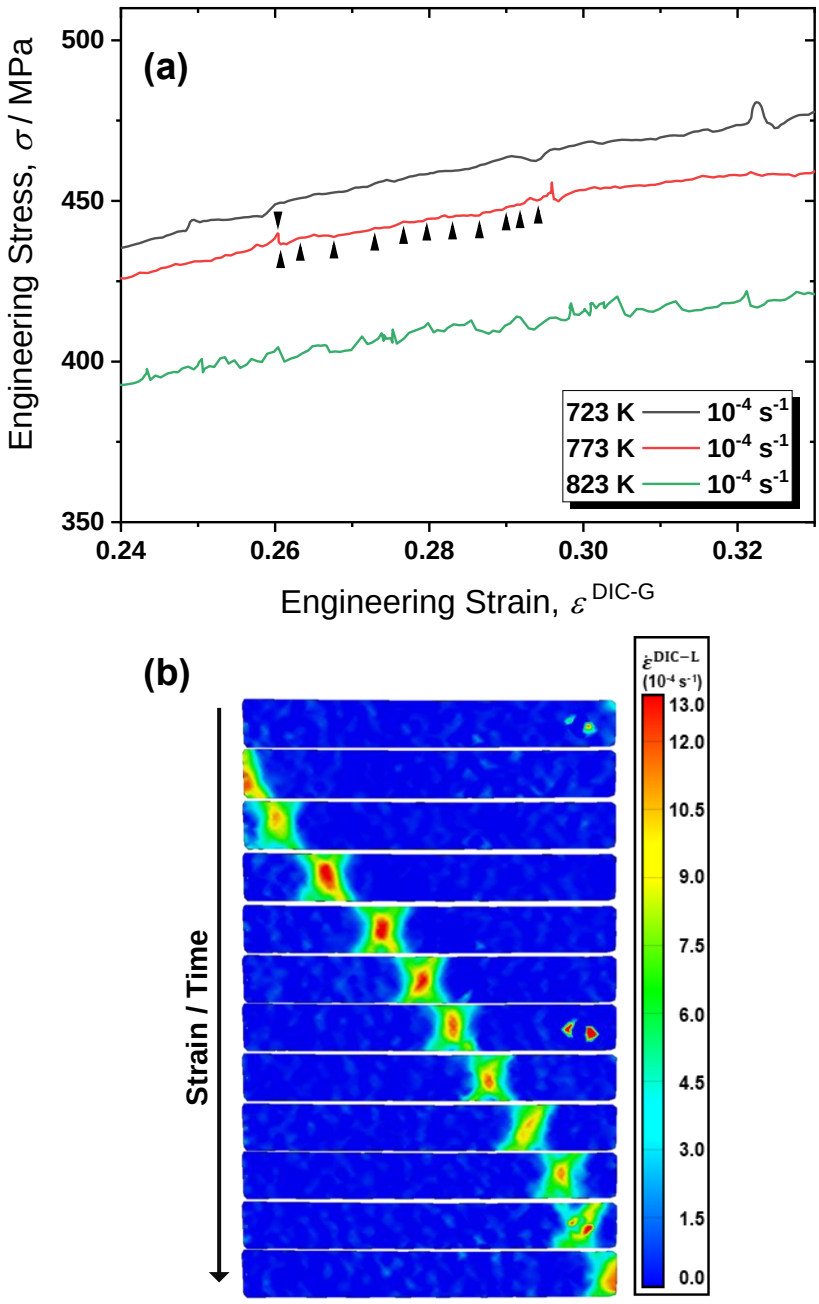

Figure 2.8 Strain rate distribution map showing A-type PLC band propagation in the gauge part of a test piece deformed at 773 K/10^{-4} s^{-1}. Each image in (b) was acquired at the strain represented by the black triangles in the stress-strain curve in(a).

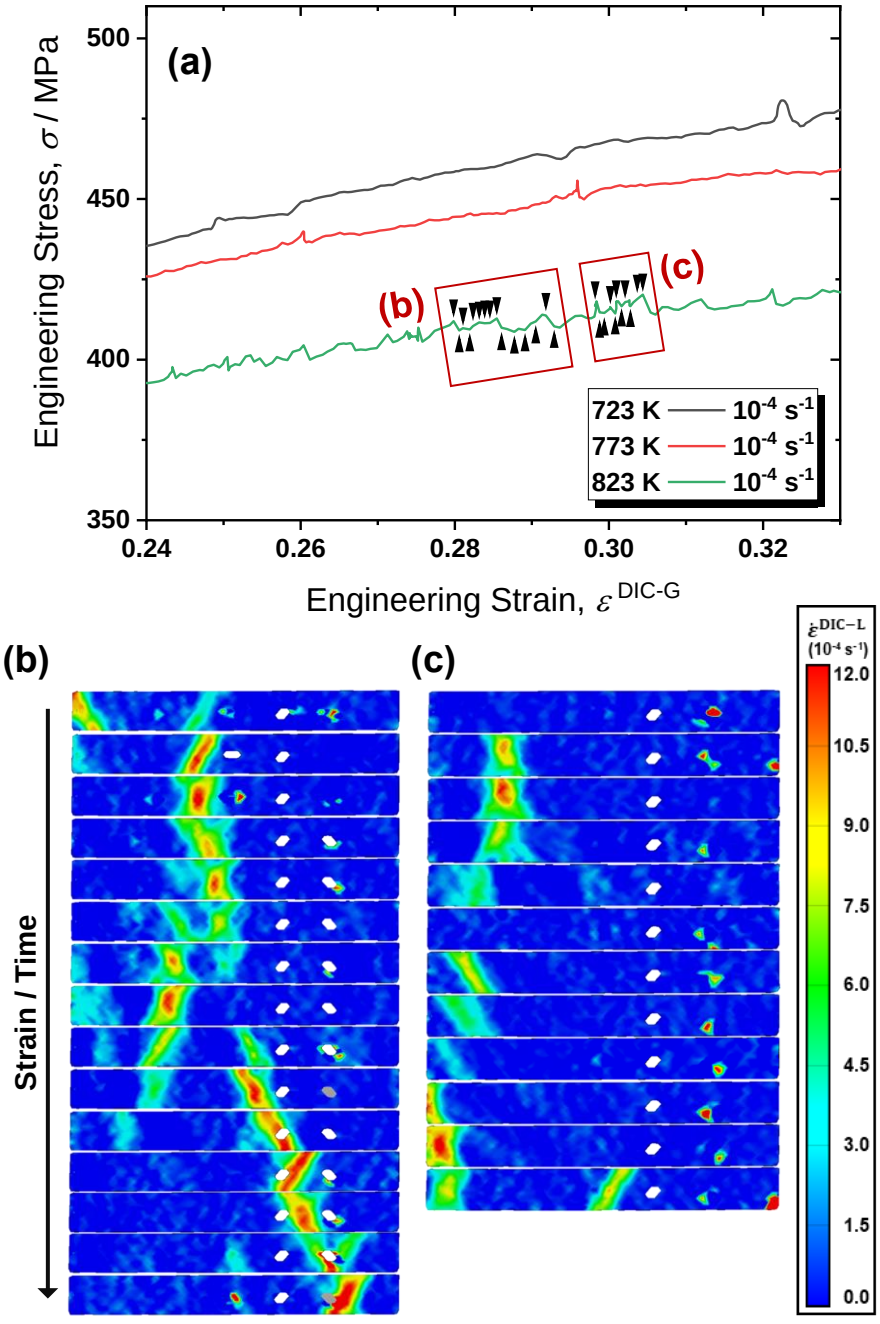

Figure 2.9 Strain rate distribution map showing B-type PLC band propagation in the gauge part of a test piece deformed at 823 K/10^{-4} s^{-1}. Each image in (b) and (c) was acquired at the strain represented by the black triangles in the red boxed segments (b) and (c) in (a), respectively.

2.3.2.2 Local strain development by A-type PLC band propagations

Considering the local strain development by the A-type PLC band, we identified other interesting characteristics of the PLC effect. **Fig. 2.10** shows the development of $\varepsilon^{\mathrm{DIC\text{-}L}}$ during tensile deformation under 773 K/10^{-4} s^{-1}. Here, the position for local strain measurement was fixed at points A and B, which were 8.0 mm away from both edges of the gauge part, as illustrated in the inset. It was confirmed that ten PLC bands (#1-10) nucleated at the edge of the point A side (starting end) and then propagated toward the opposite edge of the point B side (terminal end) in succession. Consequently, the tenth PLC band stopped at the middle of the gauge part, following which a necking deformation occurred at the stopped PLC band. The time dependencies of $\varepsilon^{\mathrm{DIC\text{-}L}}$ measured at points A and B are indicated by black and red lines, respectively. $\varepsilon^{\mathrm{DIC\text{-}L}}$ at point A increased in a stepwise shape, which suggests that the local strain instantaneously increased when each PLC band passed. Therefore, the $\varepsilon^{\mathrm{DIC\text{-}L}}$ at point B exhibited a similar stepwise shape with a time difference. There are two aspects to focus on: $\varepsilon^{\mathrm{DIC\text{-}L}}$ was higher at point B than at point A after a PLC band propagated, and the instantaneous increment of $\varepsilon^{\mathrm{DIC\text{-}L}}$ caused by the passage of the PLC band was monotonous with increasing number of PLC bands. To clarify these features of local strain by the A-type PLC band, the local strain

distribution in the gauge part where the *i*-th PLC band propagates is schematically illustrated in **Fig. 2.11**. After the n-th PLC band propagates through the gauge part ($i = n$), the contentious gradient of $\varepsilon^{DIC\text{-}L}$ gently developed from the starting end to the terminal one. Because of the gentle gradient of $\varepsilon^{DIC\text{-}L}$ in the gauge part, the (n+1)-th PLC band preferred to nucleate at the starting end, leading to the repeatable A-type PLC band propagation in an identical direction. Subsequently, when the (n+1)-th PLC band propagates, the deformation of the gauge part is highly localized at the PLC band with a steep gradient of $\varepsilon^{DIC\text{-}L}$, and the gradient gradually increases with increasing number of PLC bands. This figure reveals that the local strain rate, $\dot{\varepsilon}^{DIC\text{-}L}$, is maximized at the PLC band, suggesting that DSA should be considered under the local condition. Therefore, the change in the mean $\dot{\varepsilon}^{DIC\text{-}L}$ of the PLC band was measured under 773 K/10^{-4} s^{-1} and displayed as a function of $\varepsilon^{DIC\text{-}G}$ in **Fig. 2.12**. $\dot{\varepsilon}^{DIC\text{-}L}$ was evaluated as a mean by tracking individual PLC bands. $\dot{\varepsilon}^{DIC\text{-}L}$ is consistently much higher than the applied strain rate (10^{-4} s^{-1}) and gradually increases from 2.0×10^{-4} s^{-1} to 1.4×10^{-3} s^{-1} before the necking deformation. The initial and final $\dot{\varepsilon}^{DIC\text{-}L}$ values under different tensile conditions are summarized in **Table 2.2**. Although $\dot{\varepsilon}^{DIC\text{-}L}$ varied depending on the applied strain rate and temperature, all final $\dot{\varepsilon}^{DIC\text{-}L}$ reached a high value, 3-14 times higher than the applied

strain rate. These results suggest that the initiation of necking deformation through the development of the A-type PLC band is closely associated with the increase in $\dot{\varepsilon}^{\text{DIC-L}}$ at the PLC bands.

Fig. 2.13 shows the map of strain rate and temperature to discuss the A-type PLC effect. In this map, $\dot{\varepsilon}^{\text{DIC-G}}$, at the onset of the serrated flow in tensile curves, is shown by a black solid square, whereas $\dot{\varepsilon}^{\text{DIC-L}}$, at the initial and final PLC bands, is indicated with colored solid and open circles, respectively. From Eq. (2-5), the critical strain rate for the A-type PLC effect can be expressed as:

$$ln\,\dot{\varepsilon} = (m+\beta)\ln\varepsilon^{\text{DSA}} - \left(ln\,S + ln\,Z + \frac{Q}{RT}\right). \qquad (2\text{-}6)$$

By substituting the experimental results, $(m + \beta)$, Z, and Q, mentioned in 3.1.3 into eq. (2-6), the relation between $\dot{\varepsilon}^{\text{DIC-G}}$ and T can be calculated at a given ε^{DSA}. The calculated linear relations between $ln\ \dot{\varepsilon}^{\text{DIC-G}}$ and $1/T$ at $\varepsilon^{\text{DSA}} = 0.35$, 0.40, and 0.45, which are close to the global strain where necking deformation commences under all tensile conditions, are shown by the black lines. The calculated lines can be regarded as the transition boundaries indicating the critical strain rate and temperature condition at which the A-type PLC effect occurs. Under the tensile deformation condition at a higher temperature

and lower strain rate than the transition boundary (lower left region in the graph), the A-type PLC effect should occur before reaching the strain for necking deformation. Considering that the A-type PLC band appeared under the five global conditions, it is reasonable that all the black solid squares lie in the DSA region. On the other hand, it is more interesting that the initial $\dot{\varepsilon}^{\text{DIC-L}}$ tends to be in the DSA region, whereas the final $\dot{\varepsilon}^{\text{DIC-L}}$ is in the non-DSA region under all deformation conditions. Regardless, the necking strain varies depending on the tensile condition; however, this result suggests that the local condition in PLC bands transited from DSA to non-DSA regions during tensile deformation. The transition causes softening due to the weakening DSA effect, due to which the PLC band propagation stops, and necking deformation occurs within the PLC band. Thus, the necking process with the A-type PLC band is activated when the local strain rate inside the PLC band reaches the critical value, at which the diffusion of substitutional Cr atoms can no longer restrict the movement of dislocations.

From these results, it can be concluded that the occurrence of necking deformation associated with the A-type PLC effect is controlled by the local strain rate within the PLC band from the microscopic viewpoint, which satisfies the plastic instability from the macroscopic viewpoint. Particularly, the increment in strain by PLC band nucleation is

important and originates from the interaction between dislocations and Cr atoms or a Cr-C atom pair, although the detailed mechanism is yet to be clarified. Therefore, in order to increase uniform elongation, it is important to control the local strain rate in PLC bands by alloy design as well as control of the temperature and applied strain rate.

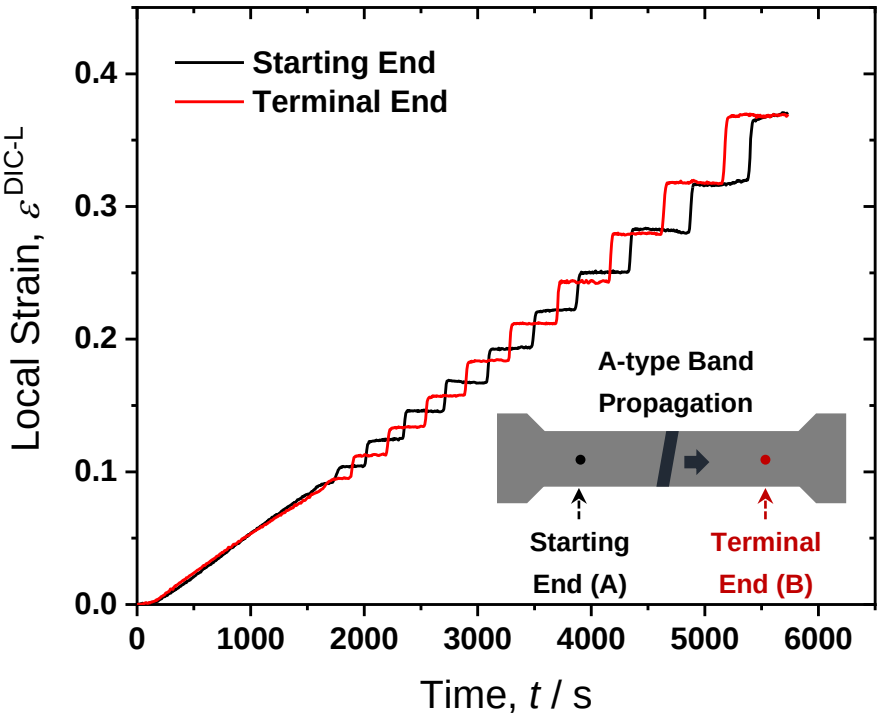

Figure 2.10 Change in local strain ε^{DIC-L} as a function of time under the tensile condition of 773 K/10^{-4}. The local strain was measured at points A and B, which were 8.0 mm away from both edges of the gauge part; starting end (black line) for the band initiation site and terminal end (red line) for the band termination site, respectively.

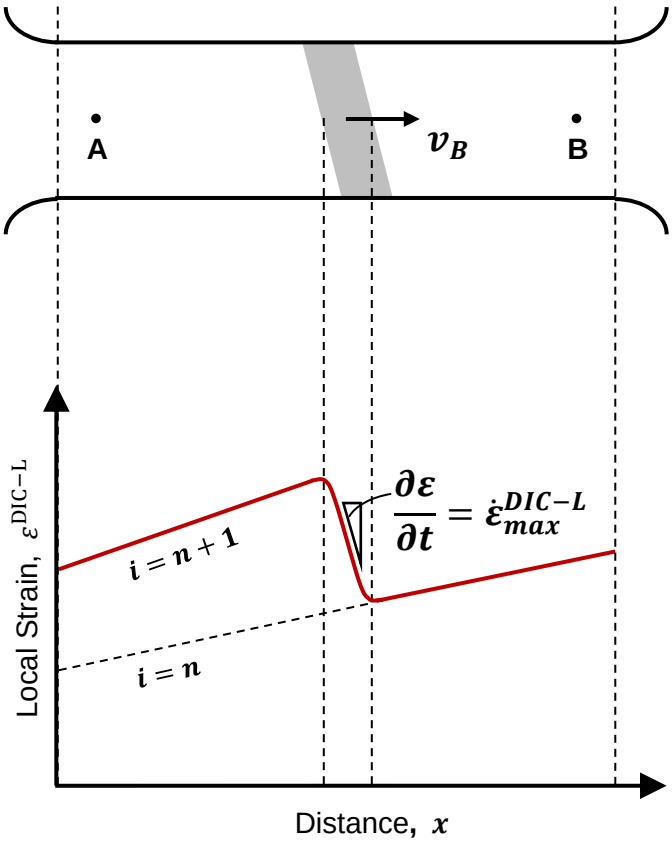

Figure 2.11 Schematic illustration showing the local strain distribution in the gauge part where the *i*-th PLC band propagates.

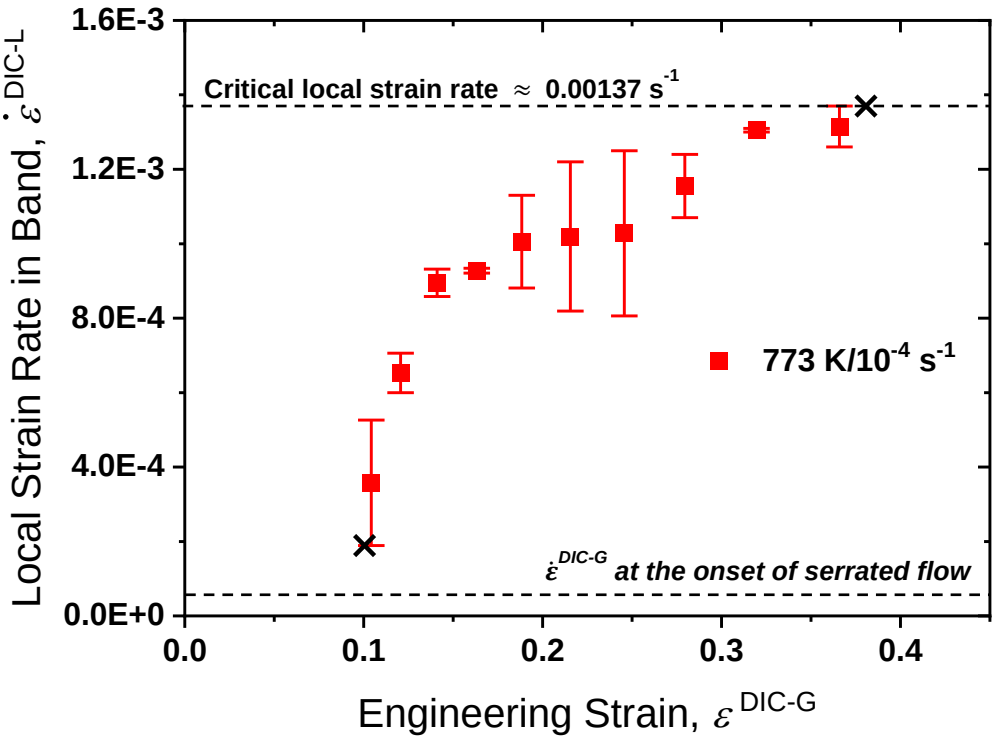

Figure 2.12 Change in local strain rate $\dot{\varepsilon}^{DIC-L}$ in each band as a function of the global strain ε^{DIC-G} at 773 K/10^{-4} s^{-1}.

Table 2.2 Local strain rates in the initial and final bands under different tensile conditions indicating A-type PLC band behavior

Testing condition	Local strain rate (s^{-1})	
	Initial band	Final band
723 K / 10^{-4} s^{-1}	1.20×10^{-4}	1.19×10^{-3}
773 K / 10^{-4} s^{-1}	1.89×10^{-4}	1.37×10^{-3}
773 K / 10^{-3} s^{-1}	1.58×10^{-3}	5.03×10^{-3}
823 K / 10^{-3} s^{-1}	9.37×10^{-4}	7.70×10^{-3}
823 K / 5×10^{-3} s^{-1}	6.96×10^{-3}	1.49×10^{-2}

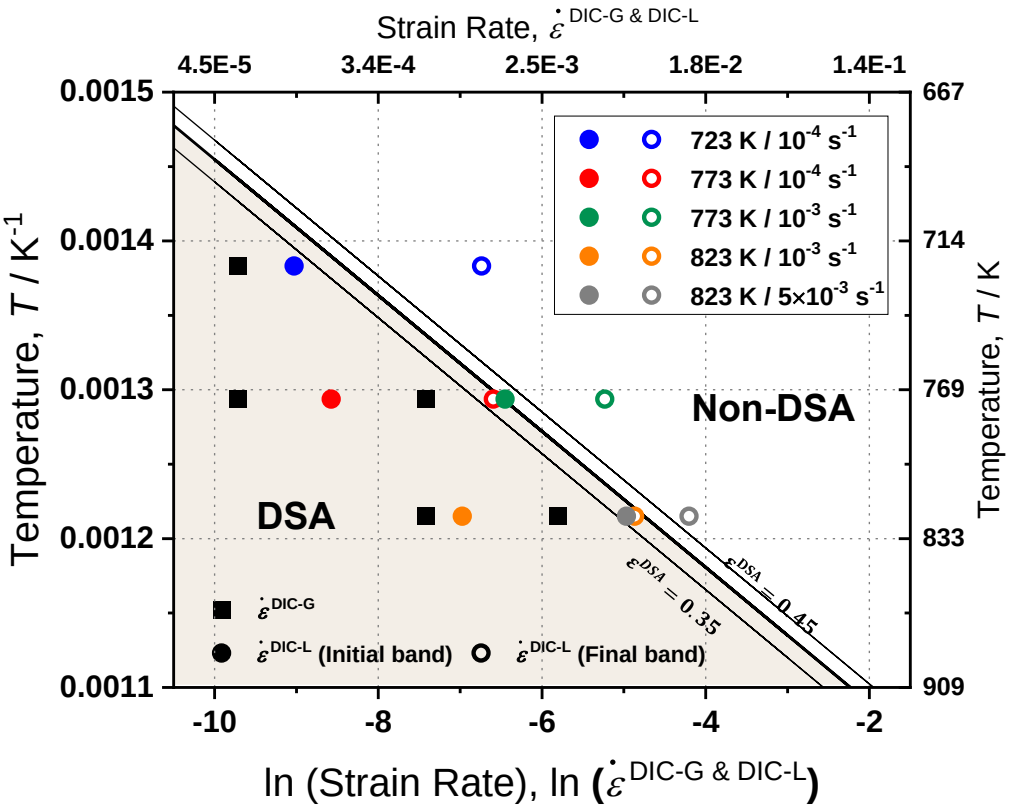

Figure 2.13 Map of $ln\ \dot{\varepsilon}$ and $1/T$, indicating the critical condition of the A-type PLC effect. The global strain rate $\dot{\varepsilon}^{DIC\text{-}G}$ at the onset of serrated flow in the tensile curves is represented by a black solid square, whereas the local strain rates $\dot{\varepsilon}^{DIC\text{-}L}$ at the initial and final PLC bands are indicated with colored solid and open circles, respectively.

2.4 Conclusions

In this chapter, high-temperature tensile testing was carried out under various testing conditions in Fe-19Cr-13Ni-0.2C austenitic stainless steel, and the high-temperature PLC effect associated with DSA was characterized using DIC analysis. The obtained conclusions are as follows:

1. High-temperature DIC analysis is a very effective method to accurately measure only the strain of a specimen while excluding the appreciable elastic contribution of the testing machine related to the lowering machine stiffness at a high temperature. The global strain rate of the gauge part was discontinuously increased stepwise with the formation of each PLC band. Finally, the total deformation of the testing system was concentrated in the gauge part on the tensile test piece, which resulted in a necking deformation according to the conventional plastic instability theory.

2. Characterization of the critical strain and strain rate of the gauge part by high-temperature DIC analysis enabled the accurate evaluation of the PLC effect. The serrated flow associated with plastic instability observed in the stress-strain curves is related to DSA caused by the interaction between the dislocations and the pipe

diffusion of the substitutional Cr atoms.

3. The local strain is nonuniformly distributed in the gauge part and is higher at the terminal end than at the starting end after a PLC band propagated. Therefore, the A-type PLC band prefers to nucleate and propagate in an identical direction. In addition, the local strain is instantaneously increased when a PLC band passes, and this instantaneous increase tends to increase with increasing number of PLC bands.

4. The local strain rate inside a PLC band is much higher than the applied strain rate to cover the total deformation of a gauge part, and increases with the progress of tensile deformation. Consequently, a necking process is activated when the local strain rate inside the PLC band reaches the critical value where the PLC effect does not occur.

2.5 References

[1] L.H. de Almeida and S.N. Monteiro, The significance of Dynamic Strain Aging in Austenitic Stainless Steel, in: Proceedings of the Second International Conference on Mechanical Behavior of Materials, Boston, 1976, pp. 1697-1701.

[2] C. Gupta, J.K. Chakravartty, S.L. Wadekar, J.S. Dubey, Effect of serrated flow on deformation behaviour of AISI 403 stainless steel, Mater. Sci. Eng. A 292 (2000) 49-55.

[3] K. Tsuzaki, T. Hori, T. Maki, I. Tamura, Dynamic strain aging during fatigue deformation in type 304 austenitic stainless steel, Mater. Sci. Eng., 61 (1983) 247-260.

[4] K. Kako, Y. Miyahara, K. Hide, M. Mayuzumi, Influence of the strain rate on the low cycle fatigue life of an austenitic stainless steel with a ground surface finish in different environments, J. Japan Inst. Met. 72 (2008) 206-210.

[5] L.H. de Almeida, I. Le May, P.R.O. Emygdio, Mechanistic modeling of dynamic strain aging in austenitic stainless steels, Mater. Char. 41 (1998) 137-150.

[6] D.W. Kim, W.S. Ryu, J.H. Hong, S.K. Choi, Effect of nitrogen on the dynamic strain ageing behaviour of type 316L stainless steel, J. Mater. Sci. 33 (1998) 675-679.

[7] D.W. Kim, W.G. Kim, W.S. Ryu, Role of dynamic strain aging on low cycle fatigue and crack propagation of type 316L(N) stainless steel, Int. J. Fatigue 25 (2003) 1203-1207.

[8] S.G. Hong and S.B. Lee, Mechanism of dynamic strain aging and characterization of its effect on the low-cycle fatigue behavior in type 316L stainless steel, J. Nucl. Mater. 340 (2005) 307-314.

[9] L.J. Meng, J. Sun, H. Xing, G.W. Pang, Serrated flow behavior in AL6XN austenitic stainless steel, J. Nucl. Mater. 394 (2009) 34-38.

[10] I. Nikulin and R. Kaibyshev, Deformation behavior and the Portevin-Le Chatelier effect in a modified 18Cr-8Ni stainless steel, Mater. Sci. Eng. A 528 (2011) 1340-1347.

[11] V. Ganesan, K. Laha, M. Nandagopal, P. Parameswaran, M.D. Mathew, Effet of nitrogen content on dynamic strain ageing behaviour of type 316LN austenitic stainless steel during tensile deformation, Mater. High Temp. 31 (2014) 162-170.

[12] B.K. Choudhary, Activation energy for serrated flow in type 316L(N) austenitic stainless steel, Mater. Sci. Eng. A 603 (2014) 160-168.

[13] A.S. Alomari, N. Kumar, K.L. Murty, Serrated yielding in an advanced stainless steel Fe-25Ni-20Cr (wt%), Mater. Sci. Eng. A 751 (2019) 292-302.

[14] D. Zhemchuzhnikova, M. Lebyodkin, D. Yuzbekova, T. Lebedkina, A. Mogucheva, R. Kaibyshev, Interrelation between the Portevin Le-Chatelier effect and necking in AlMg alloys, Int. J. Plast. 110 (2018) 95-109.

[15] H.Y. Yu, S.M. Lee, J.H. Nam, S.J. Lee, D. Fabregue, M.H. Park, N. Tsuji, Y.K. Lee, Post-uniform elongation and tensile fracture mechanism of Fe-18Mn-0.6C-xAl twinning-induced plasticity steels, Acta Mater. 131 (2017) 435-444.

[16] A. Muller, C. Segel, M. Linderov, A. Vinogradov, A. Weidner, H. Biermann, The Portevin-Le Chatelier effect in a metastable austenitic stainless steel, Metall. Mater. Trans. A 47 (2016) 59-74.

[17] L. Chen, H.S. Kim, S.K. Kim, B.C. De Cooman, Localized Deformation due to Portevin-LeChatelier Effect in 18Mn-0.6C TWIP Austenitic Steel, ISIJ Int. 47 (2007) 1804-1812.

[18] J.K. Kim, L. Chen, H.S. Kim, S.K. Kim, Y. Estrin, B.C. De Cooman, On the tensile behavior of high-manganese twinning-induced plasticity steel, Metall. Mater. Trans. A 40A (2009) 3147-3158.

[19] Y. Zhang, J.P. Liu, S.Y. Chen, X. Xie, P.K. Liaw, K.A. Dahmen, J.W. Qiao, Y.L. Wang, Serration and noise behaviors in materials, Prog. Mater. Sci. 90 (2017) 358-460.

[20] A. Yilmaz, The Portevin-Le Chatelier effect: a review of experimental findings, Sci. Tech. Adv. Mater. 12 (2011) 063001.

[21] P. Rodriguez, Serrated plastic flow, Bull. Mater. Sci. 6 (1984) 653-663.

[22] P.G. McCormick, A model for the Portevin-Le Chatelier effect in substitutional alloys, Acta Metall. 20 (1972) 351-354.

[23] B.K. Choudhary, K.B.S. Rao, Influence of strain rate and temperature on serrated flow behaviour in type 316L(N) austenitic stainless steel, Trans. Indian Inst. Met. 55 (2002) 311-319.

[24] A. Van Den Beukel, On the mechanism of serrated yielding and dynamic strain ageing, Acta Metall. 28 (1980) 965-969.

[25] C.F. Jenkins, G.V. Smith, Serrated plastic flow in austenitic stainless steel, Trans. Metall. Soc. AIME 245 (1969) 2149-2156.

[26] L.J. Cuddy, W.C. Leslie, Some aspects of serrated yielding in substitutional solid solutions of iron, Acta Metall. 20 (1972) 1157-1167.

[27] A.W. Sleeswyk, Slow strain-hardening of ingot iron, Acta Metall. 6 (1958) 598-603.

[28] R.A. Mulford, U.F. Kocks, New observations on the mechanisms of dynamic strain aging and of jerky flow, Acta Metall. 27 (1979) 1125-1134.

Chapter 3

Serrated Flow Accompanied with Dynamic Type Transition of the Portevin-Le Chatelier Effect in Austenitic Stainless Steel

3.1 Introduction

Dynamic strain aging (DSA) is the dynamic interaction between mobile dislocations and solute atoms during plastic deformation in solid-solution alloys [1-5]. In DSA, solute atoms can diffuse to dislocations that are temporarily arrested at obstacles, such as dislocation junctions, grain boundaries, and precipitates, resulting in the pinning of mobile dislocations, i.e., the formation of a Cottrell atmosphere [6]. Eventually, the pinned dislocations are suddenly reactivated owing to depinning of the solute atoms. This series of processes originating from DSA are continuously repeated as long as the diffusion process is effective. The repetition appears as serrated flow in a stress-strain curve and is known as the Portevin-Le Chatelier (PLC) effect. It is also known that different types of serrated flow appear depending on the deformation conditions, temperature, and applied strain rate [7-9]. Three types of serrated flow are widely recognized, as shown in **Fig. 3.1**. At higher strain rates or lower temperatures, A-type serration occurs, which is characterized by periodic stress peaks followed by a drop to the general level of the stress-strain curve. In C-type serration, stress initially drops and then rises to the general level of stress at lower strain rates or higher temperatures. As the

intermediate condition, B-type serration with stress oscillation becomes visible around the general level of stress.

Single-type serration usually appears under identical deformation conditions. However, it has been reported that the serrated flow in various alloys sometimes transitions dynamically from one type to another type, even when both the deformation temperature and applied strain rate are kept constant. For example, Yu et al. [10] reported that the type of serrated flow changed in the order of B-, (B + C)-, and C-type at 873 K in 80/20 nickel-chromium alloy. Transition behavior from A- to (A+B)-type was also observed at 923 K in the austenitic stainless steel (γ-STS) 316LN [11]. However, it is unclear why the type transition of PLC-affected serration takes place dynamically under constant deformation conditions, although variation of the PLC effect affects the mechanical properties, especially the strain hardening and fracture behavior [12-16].

It has also been reported that localized deformation bands on gauge parts of test specimens occur during the appearance of serrated flow [7-9]. These localized deformation bands are called PLC bands. Recently, some researchers investigated PLC bands in detail using digital image correlation (DIC) analysis, which can analyze and

visualize distributions of the strain and strain rate of an object with high accuracy [15-21]. As a result, it was found that nucleation and propagation behavior of PLC bands differed depending on the deformation conditions and that the difference tended to correspond to the variation in the type of serrated flow. However, there is still little information on the correlation between serrated flow and PLC band behavior, especially in materials showing the PLC effect at high temperatures, because only the appearance of serrated flow has been focused without observing high-temperature PLC bands. According to previous studies [7-11], the dynamic transition of serration type at high temperature should be also considered in connection to PLC band behavior. As for the application of DIC analysis to PLC bands, in our previous research [20], we succeeded in applying DIC analysis for high-temperature deformation and investigated the propagation behavior of a single A-type PLC band at approximately 773 K in γ-STS. It is expected that this newly developed high-temperature DIC analysis would help us understand the mechanism of the dynamic transition of serrated flow associated with PLC bands.

In this study, the tensile deformation behavior of γ-STS was investigated using high-temperature DIC analysis at temperatures from 473 K to 623 K, and the corresponding relationship between the types of serration and PLC band behavior was clarified. The

dynamic type transition of PLC-affected serration is discussed in terms of the variation of global strain rate at the gauge part using numerical modeling for PLC band propagation.

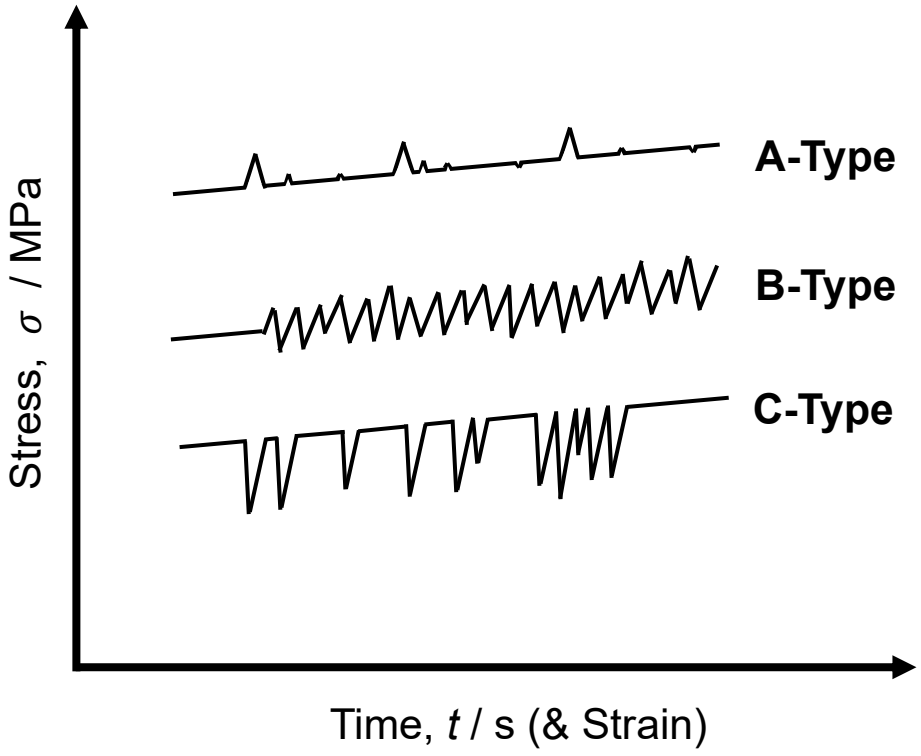

Figure 3.1 Schematic illustration for three types of serration flow generally accepted [9].

3.2 Experimental

3.2.1 Material

In this study, stable γ-STS, Fe-19Ni-13Cr-0.2C in wt.%, was used, and its chemical composition is detailed in **Table 2.1** (see chapter 2). A cold-rolled plate 2.0 mm thick was solution treated at 1473 K for 3.6 ks, followed by water cooling. The solution-treated material had an austenitic single phase with equiaxed grains 67 μm in diameter. For tensile testing, a plate-shaped test piece with a gauge length of 50 mm and a width of 10 mm was machined from the solution-treated material by an electro-discharge machine. The surface of the test piece was mechanically polished to eliminate the damaged layer induced during the machining. Speckle patterns were formed by decorating the gauge part of the tensile test piece with heat-resistant black-and-white sprays.

3.2.2 Tensile testing with DIC analysis

Tensile testing was performed using an Instron-type tensile testing machine equipped with a heating furnace (AG-100KNG/RX and TCH-220PSP, Shimadzu Corp.) at temperatures from 473 K to 623 K under applied strain rates from 5×10^{-5} s^{-1} to 5×10^{-4}

s^{-1}. During tensile testing, the data sampling rate of the tensile load was properly chosen to capture stress fluctuation behavior relevant to serrated flow (>3 Hz). We confirmed that there was no precipitation, even after tensile fracture.

At the same time, the tensile deformation behavior was captured digitally as 2752 × 2200-pixel images at a sufficiently high time resolution (~1/7 fps) using a three-dimensional camera system, ARAMIS 3D, developed by GOM. Next, the distributions of strain and strain rate were analyzed by the DIC software GOM Correlate Professional. The positional relation between the high-temperature tensile testing machine, the furnace, and the DIC analyzing cameras followed the method described by chapter 2.

3.2.3 Definition of serration type

According to the **Fig. 3.1**, as suggested by Rodriguez [9], the magnitude of the stress fluctuation in stress-strain curves was used for the detection and type classification of serrated flows. However, no quantitative criterion of the magnitude of stress fluctuation for the serrated flow has been established so far. Because the stress fluctuation caused by the DSA process is sometimes extremely small, especially at lower strain regions, two types of serration can overlap in many cases [7-11]. Therefore, the threshold of the

magnitude of stress fluctuation was treated objectively first. After tensile testing, a stress-strain curve was generalized using the Savitzky-Golay smoothing filter (built-in OriginPro® 9.85 software) to obtain a referential stress-strain curve without serrations. Each point of the generalized tensile data was acquired from the respective second-order polynomial made using 300-1500 raw data points (depending on data sampling rate in each testing). Comparing the serrated flow with the generalized non-serrated flow, the absolute value of the maximum deviation in stress between them within a certain period of time (~40 s) was evaluated as the magnitude of the stress fluctuation, $\Delta\sigma$. When a stress-strain curve had a $\Delta\sigma$ value higher than 0.5 MPa at a given time, it was regarded as serrated flow because this value was higher than the tolerance of the testing machine. In A-type and C-type serrated flows, a relatively large stress peak, jump-up or drop appears along with the stress fluctuation. Therefore, the type classification of serrated flows was conducted in terms of the ratio of the magnitude of the stress peak $\Delta\sigma_{peak}$ against $\Delta\sigma$ just before the stress peak $R_{\Delta\sigma}$, as schematically illustrated in **Fig. 3.2**. The serrations were classified into five types according to $R_{\Delta\sigma}$ as follows:

$R_{\Delta\sigma}$: A-type $\geqq$ 2.5 > (A+B)-type $\geqq$ 1.5 > B-type $\geqq$ -1.5 > (B+C)-type $\geqq$ -2.5 > C-type

For A- and C-type serrated flows, $\Delta\sigma$ was sometimes lower than 0.5 MPa while maintaining clear stress peaks. In such cases, these serrated flows were simply classified as A- or C-type serrations.

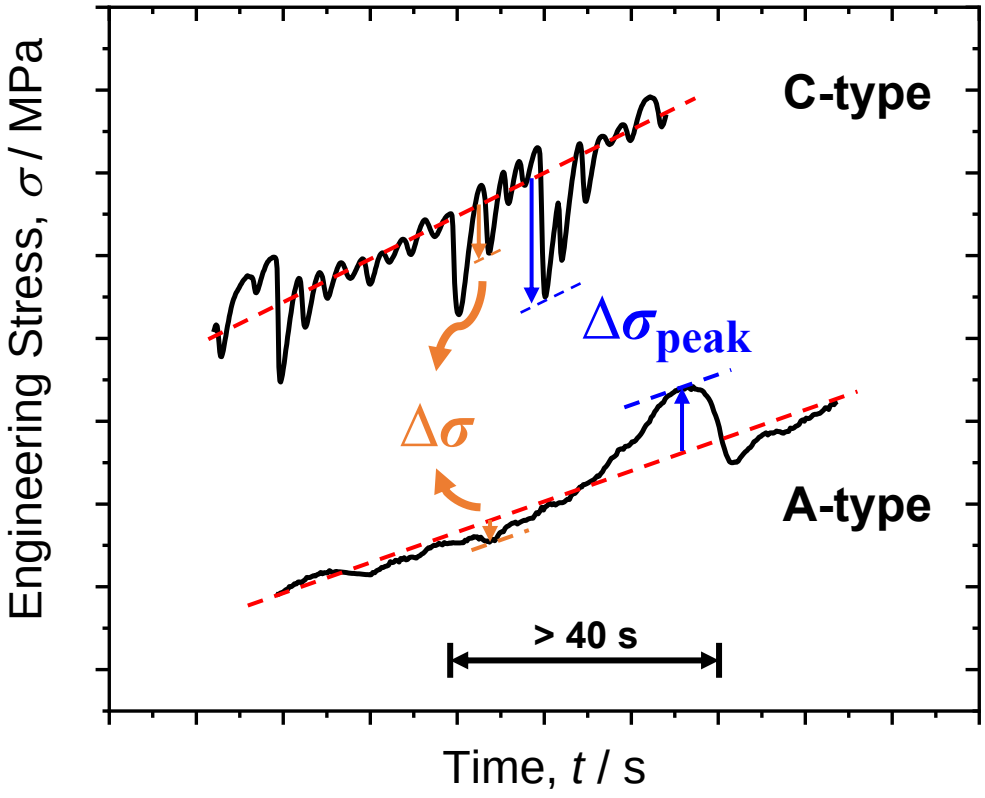

Figure 3.2 Schematic illustration for the quantitative definition method of serrated flow.

3.3 Results

3.3.1 Experimental results

3.3.1.1 Serration behavior

Fig. 3.3 shows engineering stress-strain curves tested at 523 K (red), 573 K (blue), and 623 K (green) at a strain rate of 10^{-4} s^{-1} as representative results in this study. Here, the horizontal axis is indicated by time *t* to compare with subsequent DIC analyses. The stress-strain curves obtained at different strain rates are shown in **Fig. 3.4**. The stress-strain curves clearly show serrated flow in all temperature regions, and the flow stress increases with decreasing temperature, which are typical characteristics of DSA. It has been reported that the serrated flow in austenitic stainless steels in these temperature regions is induced by DSA and is attributed to the diffusion of interstitial carbon but not substitutional chromium [21-24]. As indicated in **Fig. 3.5 (a)** and **(b)**, the activation energy for DSA evaluated by temperature and strain rate dependencies for critical strain (see section 1.3.1 and 2.3.1.3) was calculated to be approximately 61 kJ/mol. This value is close to one-half that of carbon volume diffusion in the austenite matrix (135 kJ/mol), which suggests that DSA is controlled by the pipe diffusion of carbon. It should be noted

here that the serrated flow and its stress fluctuation behavior looked different depending not only on temperature but also on deformation time. **Fig. 3.6(a)** and **(b)** show the magnified images of Fig. 3.3 at t = 700-1100 s and 3500-5250 s, respectively. Here, jump-up and drop stress peaks, which characterize A- and C-type serration, are indicated by upward- and downward-pointing triangles, respectively. In addition, some of the neighboring stress fluctuations (or oscillation) are indicated by line segments. At 623 K (green), serrated flow changed dynamically from (A+B)- to (B+C)- and then to single C-type serration (a). The serration behavior eventually diminished at approximately t = 1500 s (b). At 573 K (blue), (A+B)-type serration appeared at the early stage of deformation (a) and quickly transitioned to C-type serration (b). Unlike the abovementioned (A+B)-serration consisting of both jump-up stress peaks (A-type) and large stress fluctuations (or oscillation, B-type), relatively small stress fluctuation occurred between two adjoining A-type serration peaks at 523 K, leading to a single A-type serrated flow (b).

These transition behaviors of serrated flow depending on temperature and deformation time are summarized in **Fig. 3.7**. The figure clearly shows that the starting time of serrated flow decreased, i.e., lower critical strain, with increasing temperature and that the serrated flow consisted of various types of serrations. Although the type variation

is intricately interrelated in all temperature regions, there are two trends: (1) A- and C-type serrations are isolated from each other and (2) B-type serration tends to be activated together with A-type serration rather than C-type serration. The dynamic transition of serration type was therefore investigated while taking into account PLC band development.

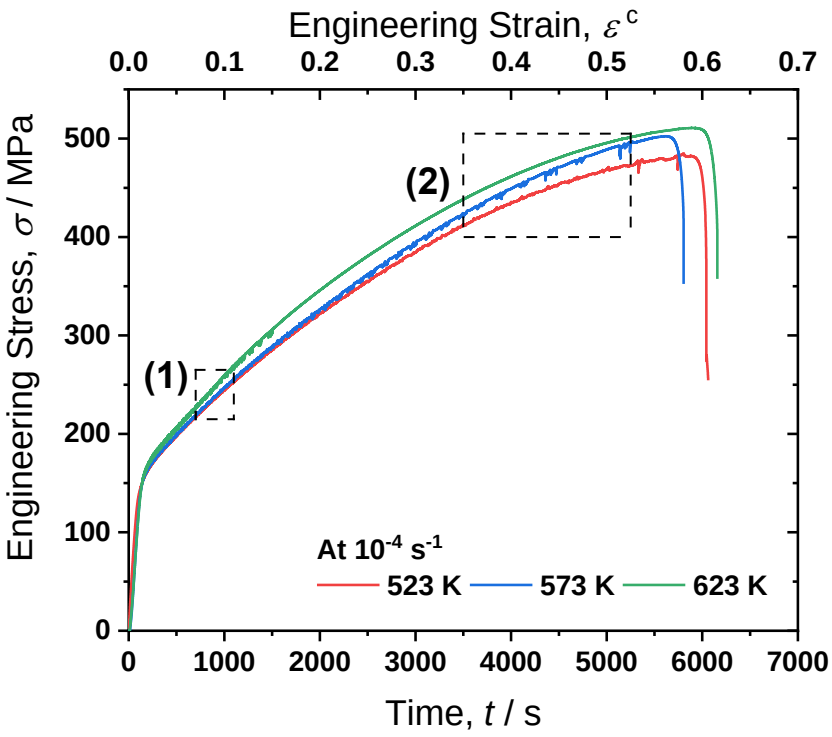

Figure 3.3 Engineering stress-strain curves of specimens tested at temperatures ranging from 523 K to 623 K at an applied strain rate of 10^{-4} s^{-1}.

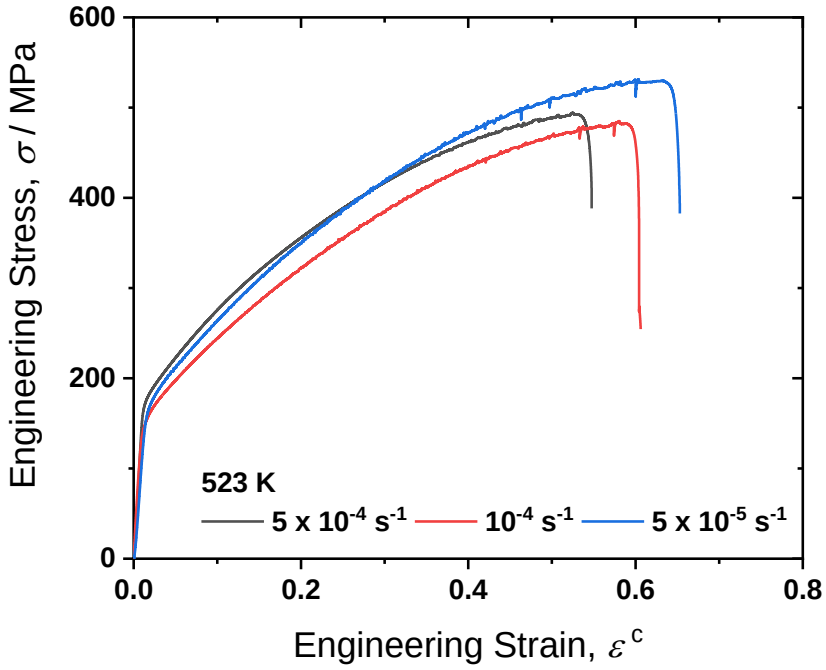

Figure 3.4 Engineering stress-strain curves with varying applied strain rate at 523 K.

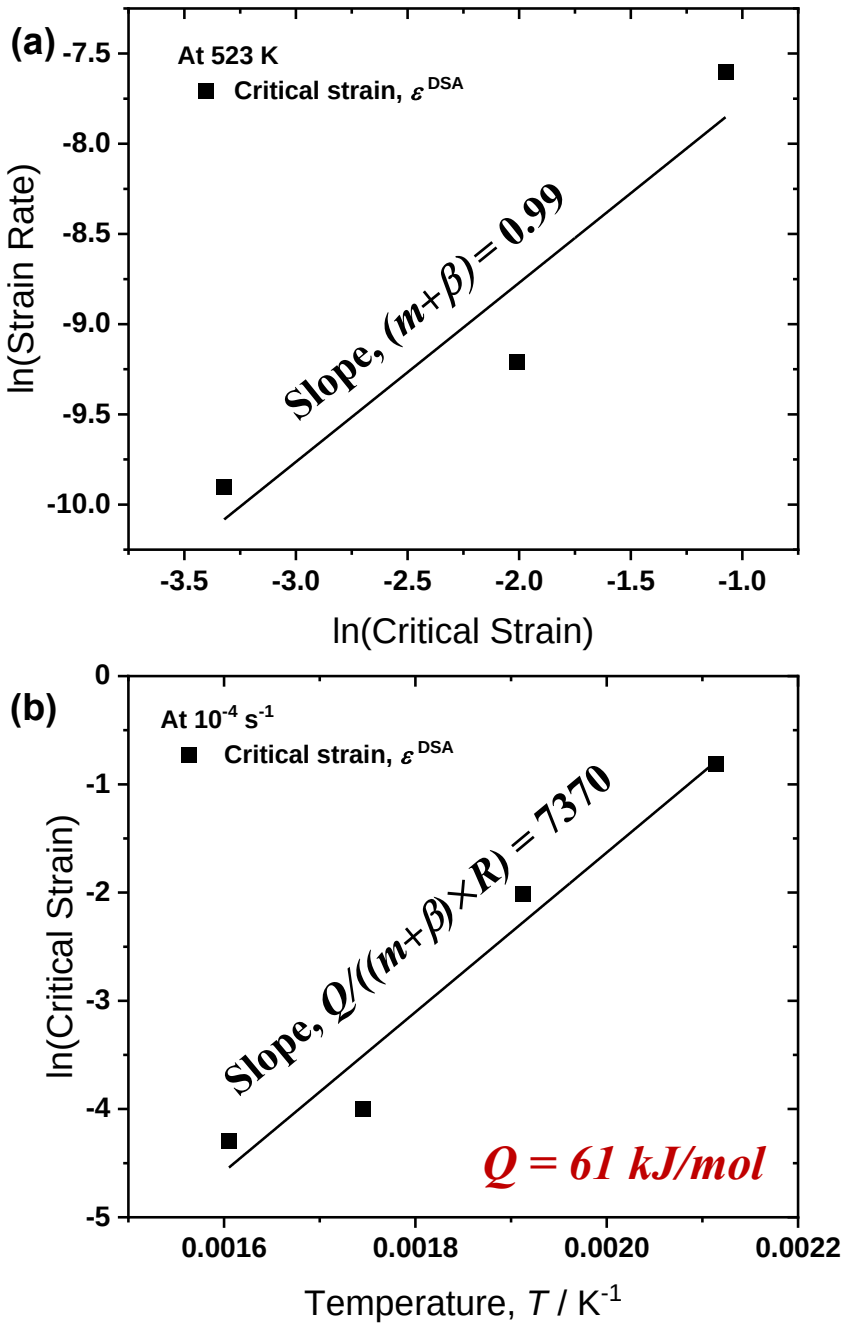

Figure 3.5(a) *ln*(applied strain rate) vs *ln*(critical strain) at 523 K; (b) *ln*(critical strain) vs $1/T$ at the applied strain rate 10^{-4} s^{-1}.

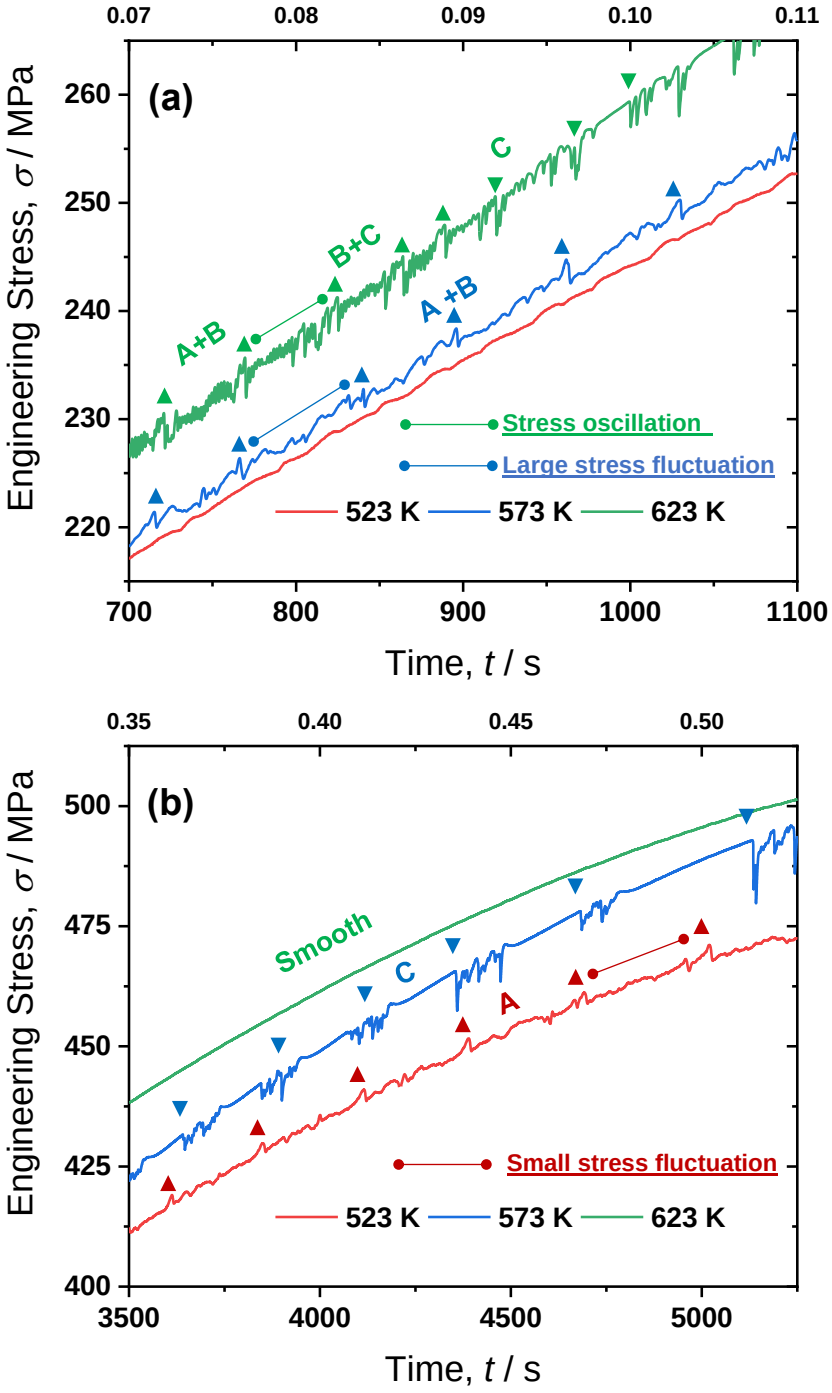

Figure 3.6 Magnified images of the boxed segments (a) for the left box (1) and (b) for the right box (2), respectively, in Fig. 3.3.

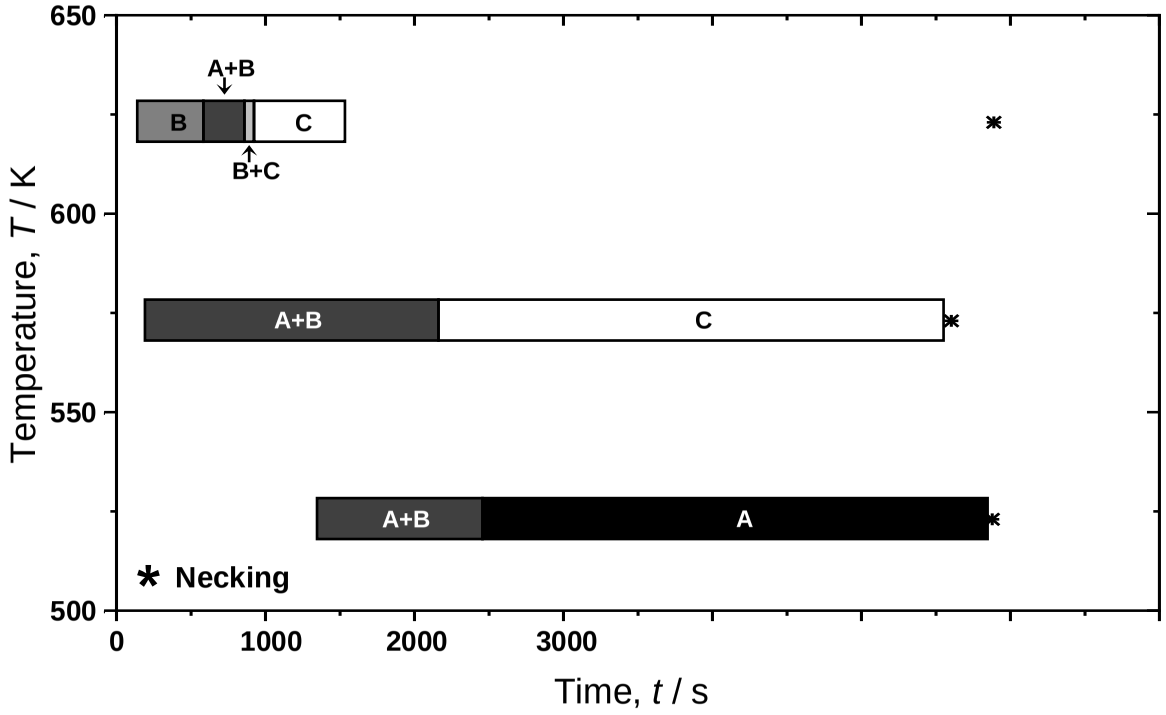

Figure 3.7 Serration behavior with deformation time at three temperatures.

3.3.1.2 Correlation between serration and PLC band behavior

Fig. 3.8 shows the time evolution of strain rate distribution on the gauge part at three temperatures. The local strain rate along the tensile direction was evaluated along the central axis of the gauge part by high-temperature DIC and continuously displayed in a serial flow of testing time. The top side of test piece was fixed in the tensile testing machine, and thus the bottom side is moved down in this image. The high-temperature DIC analysis clearly proved that plastic deformation was localized in a narrow region of the gauge part for a long period, and its strain rate was much higher than the applied strain rate of 10^{-4} s^{-1}. The highly strained local region moved along the gauge part during tensile testing, which reveals that the PLC band clearly developed under the current deformation conditions. However, the PLC band behavior seemed to vary during tensile deformation. In addition to the strain rate development, the dynamic transition in serration type with respect to time, summarized in Fig. 3.7, is displayed on the upper side of each image. It was found that the PLC band behavior tended to vary in accordance with the type transition of serrated flow. The correspondence between the serration type and the PLC band behavior is characterized in detail as follows with individual examples.

A-type serrated flow (**Fig. 3.9**, $T = 523$ K and $t = 4370$-4670 s): A PLC band nucleated at the bottom side and fully propagated toward the top side of the gauge part. In response to this, a large stress peak (jump-up stress peak) came from the PLC band nucleation, and small stress fluctuation continued during PLC band propagation in the stress-strain curve. The propagating manner, where a PLC band nucleated with a large stress peak and continuously moved to the opposite gauge part, is like "walking". Similar A-type PLC band behavior was observed at higher temperatures in our previous study [20].

B-type serrated flow (**Fig. 3.10**, $T = 623$ K and $t = 225$-525 s): Unlike the nucleation of the A-type PLC band, this PLC band nucleated inside the gauge part, as indicated by white arrows in the DIC image. The manner of PLC band propagation was different from the "walking" A-type PLC band. It was found that the PLC bands preferred to be isolated near the previous band, as indicated by the curved orange arrows, and they did not connect with each other perfectly. This proves that the PLC band propagation in this case progressed by relay nucleation of many PLC bands with relatively wide intervals. The propagating manner in a B-type PLC band is thus that of "hopping." Accordingly, the propagation is not smooth, and the propagation distance is shorter compared with that of an A-type PLC band. In the stress-strain curve, relatively large stress peaks are shown

along the stress oscillation curve, as indicated by upward-pointing triangles. When a relatively large stress peak appears, a new PLC band tends to nucleate in a new region (as indicated by white arrows in DIC images). Between the adjoining large stress peaks, very dense stress fluctuations occur with hopping propagation.

(A+B)-type serrated flow (**Fig. 3.11**, T = 573 K and t = 400-700 s): The propagation behavior of this PLC band was intermediate between A-type and B-type PLC bands. The interval between the relay nucleation of individual PLC bands (hopping distance) was narrower than that of B-type PLC bands, but the propagation seemed awkward (quasi-propagation). The distance of quasi-propagation in the gauge part was relatively short at the earlier stage of the (B+A) region, but it gradually increased with increasing time. Comparing the serrated flow with the DIC images, the stress fluctuated irregularly, with relatively higher stress amplitude than that in A-type serrated flow but less densely than that in B-type serrated flow during propagation of the PLC band. This PLC band thus shows intermediate behavior between a “walking” A-type PLC band and a ”hopping” B-type PLC band.

C-type serrated flow (**Fig. 3.12**, T = 623 K and t = 1250-1550 s): Unlike the above

three types, in C-type serrated flow, individual PLC bands had no interaction with each other. PLC bands nucleated at random places in the gauge part in a “jumping” manner, as indicated by the white arrows. The PLC band did not propagate, and thus the whole plastic deformation of the gauge part progressed only by simultaneous nucleation of many immobile PLC bands. Furthermore, it is interesting that when the simultaneous nucleation of PLC bands tended to be localized, jump-down stress peaks appeared in the stress-strain curve.

Based on the abovementioned serration and PLC band behavior, the corresponding relationship between them is summarized in **Fig. 3.13**. The variation of serrated flow is essentially attributed to the microscopic manner of PLC band nucleation, as mentioned by Yilmaz [8]. When PLC bands leading to highly localized plastic strain autocatalytically nucleate in the vicinity of a previously nucleated PLC band, the relay nucleation of the PLC bands is visualized as macroscopically smooth propagation of the PLC band. The formation of a macroscopic PLC band results in peak stress, whereas the propagation is associated with stress fluctuation on the stress-strain curve. If the microscopic manner of PLC band nucleation changes from walking to hopping with relatively wide intervals, the propagation of the PLC band becomes disconnected with relatively larger stress

fluctuation or oscillation. Also, the propagation distance decreases owing to the initiation of another series of PLC band nucleation and propagation steps. This corresponds to the transition from A-type to B-type serrated flow. Because the difference between them is the interval between relayed PLC bands, they easily appear together as (A+B)-type serration. Actually, it is difficult to clearly distinguish the transition from A- to (A+B)-type and from (A+B)- to B-type serration, and the serration type gradually changes during deformation. In contrast to the PLC band propagation, when PLC bands nucleate randomly in a jumping manner, propagation of the PLC band cannot occur. Although the reason why the flow stress decreases only in C-type serration has been unclear, it is expected that dislocations that are already pinned might be reactivated by a slight increase in applied stress.

It is noteworthy that strain localization behavior was clearly observed by DIC analysis at the onset of (A+B)-type serration at 523 K (see the strain rate distribution map in Fig. 3.8), where serrated flow could not be detected by the criterion used in this study owing to very small stress fluctuation. This reveals that the precursor of the PLC effect, which could hardly be detected from the stress-strain curve, must have occurred during deformation.

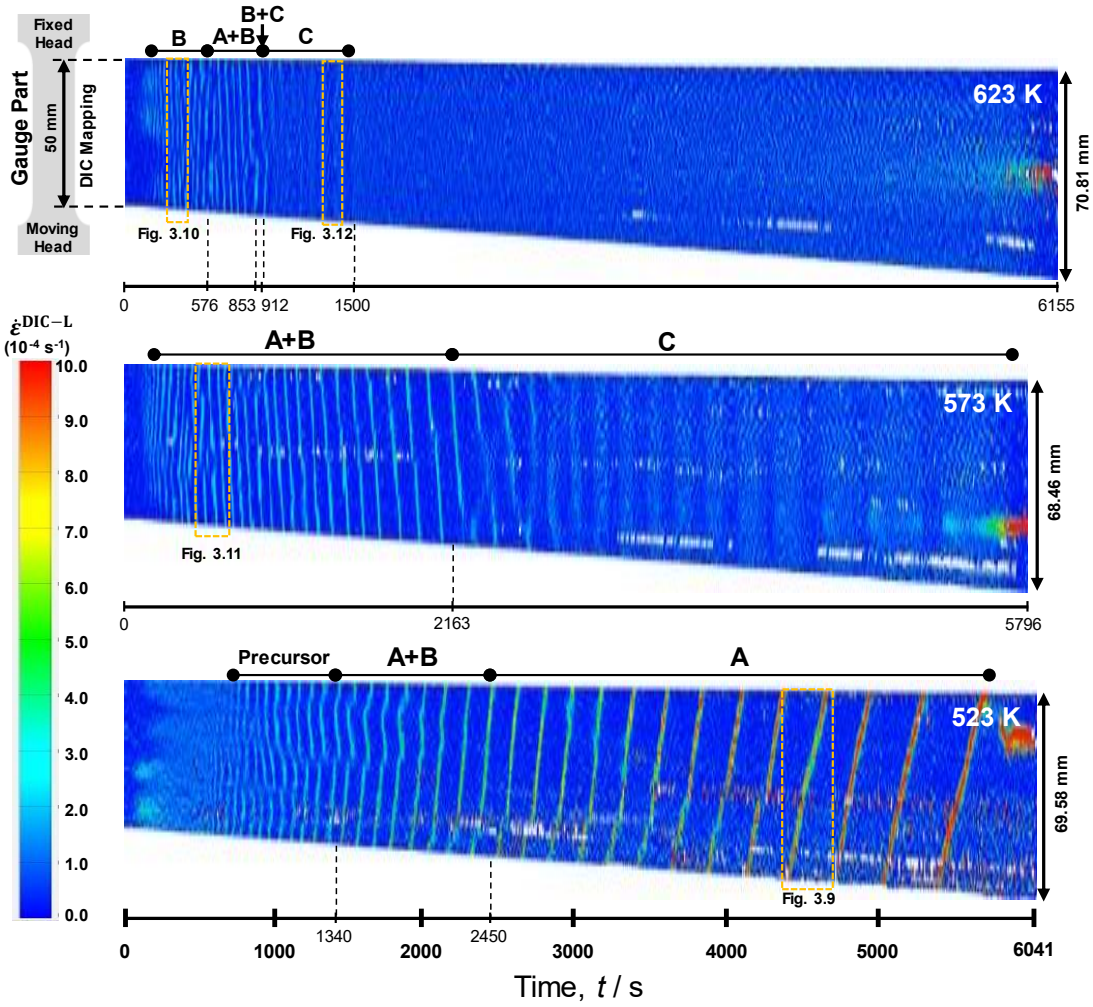

Figure 3.8 Time evolution of strain rate distribution on the gauge part at three temperatures. The local strain rate, $\dot{\varepsilon}^{\text{DIC-L}}$ along the tensile direction was evaluated along the central axis of the gauge part by high-temperature DIC and continuously displayed in a serial flow of testing time.

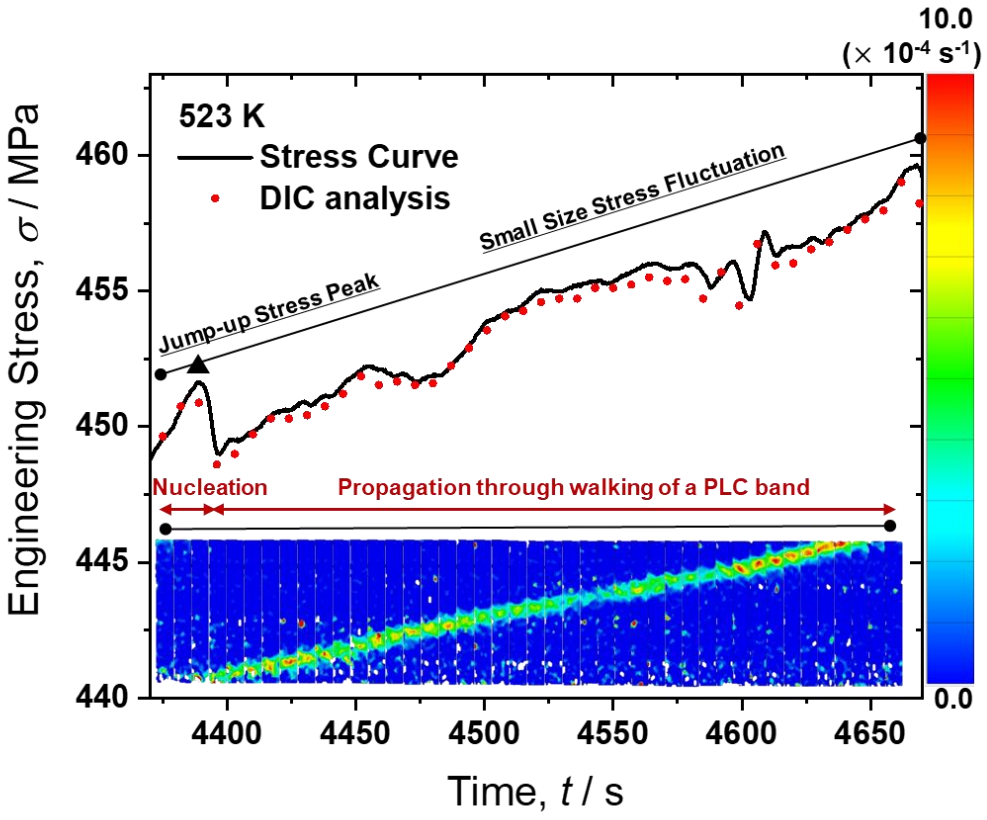

Figure 3.9 Strain-rate distribution map showing A-type PLC band propagation in the gauge part of a test piece deformed at 523 K/10^{-4} s^{-1}, as indicated by the dotted segment in Fig. 3.8. Each DIC image was acquired at the strain represented by the red circles in the stress–strain curve.

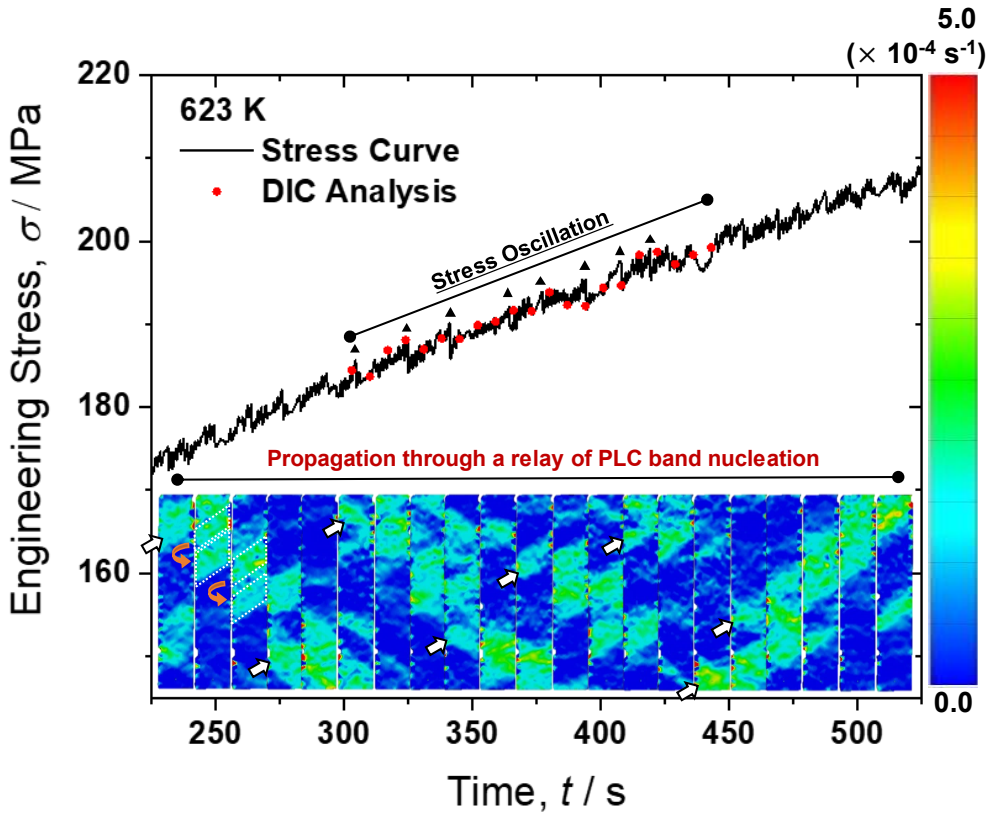

Figure 3.10 Strain-rate distribution map showing B-type PLC band propagation in the gauge part of a test piece deformed at 623 K/10^{-4} s^{-1}, as indicated by the dotted segment in Fig. 3.8. Each DIC image was acquired at the strain represented by the red circles in the stress–strain curve.

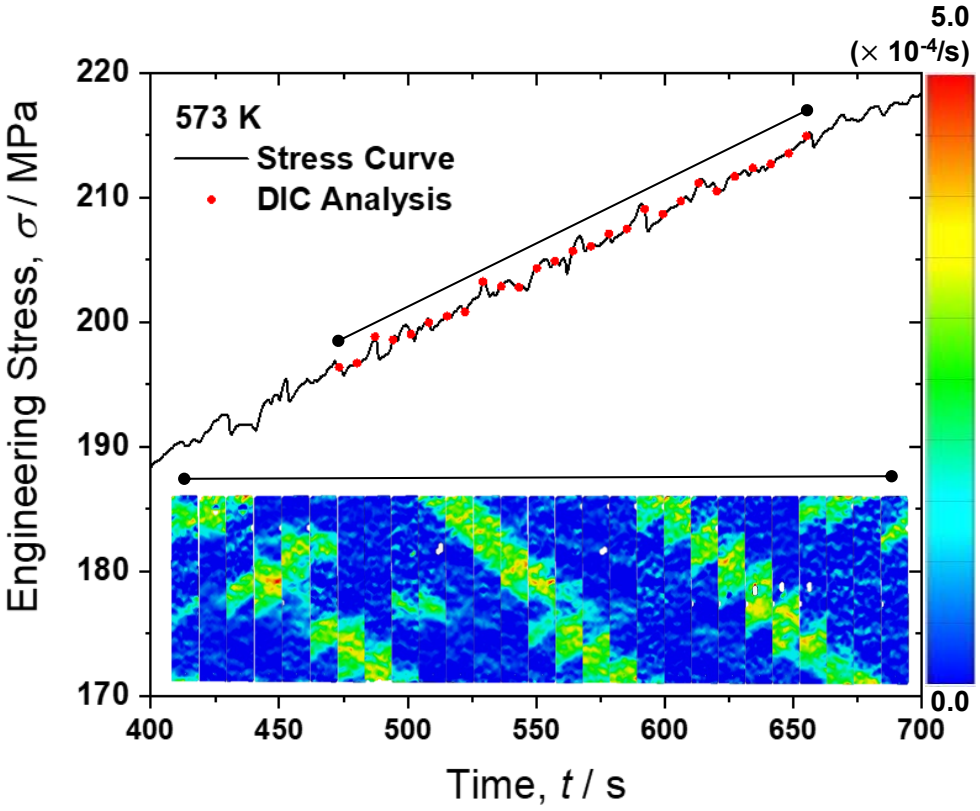

Figure 3.11 Strain-rate distribution map showing (A+B)-type PLC band propagation in the gauge part of a test piece deformed at 573 K/10^{-4} s^{-1}, as indicated by the dotted segment in Fig. 3.8. Each DIC image was acquired at the strain represented by the red circles in the stress–strain curve.

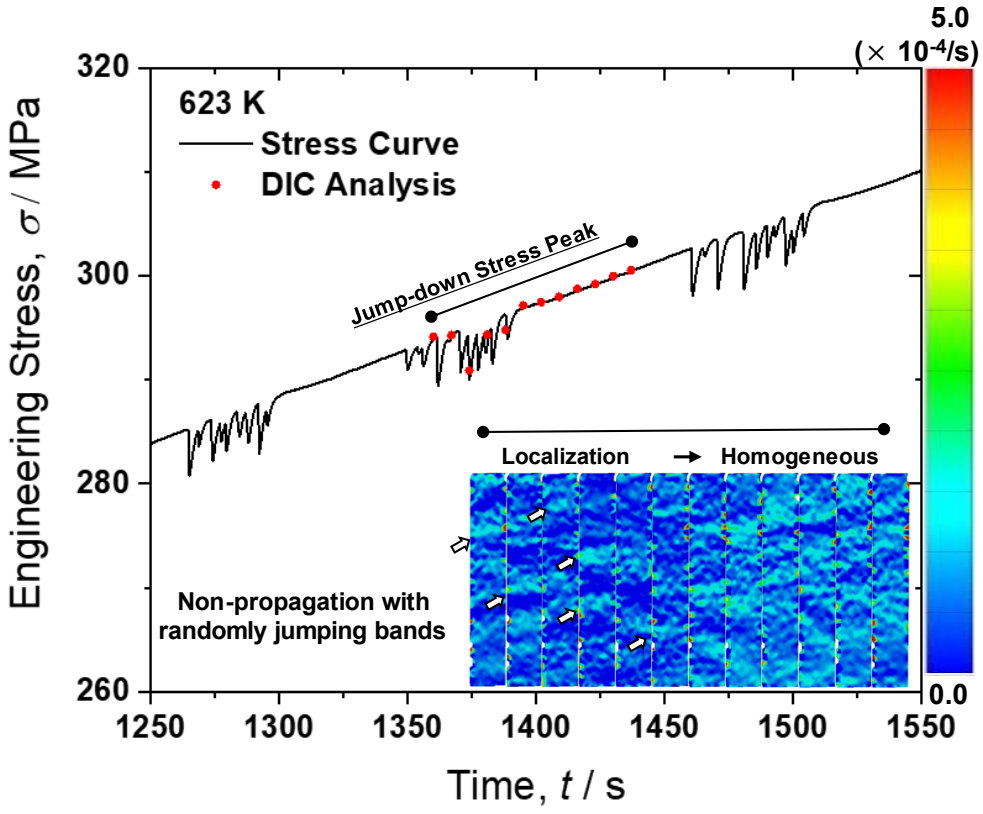

Figure 3.12 Strain rate distribution map showing C-type PLC band propagation in the gauge part of a test piece deformed at 623 K/10^{-4} s^{-1}, as indicated by the dotted segment in Fig. 3.8. Each DIC image was acquired at the strain represented by the red circles in the stress–strain curve.

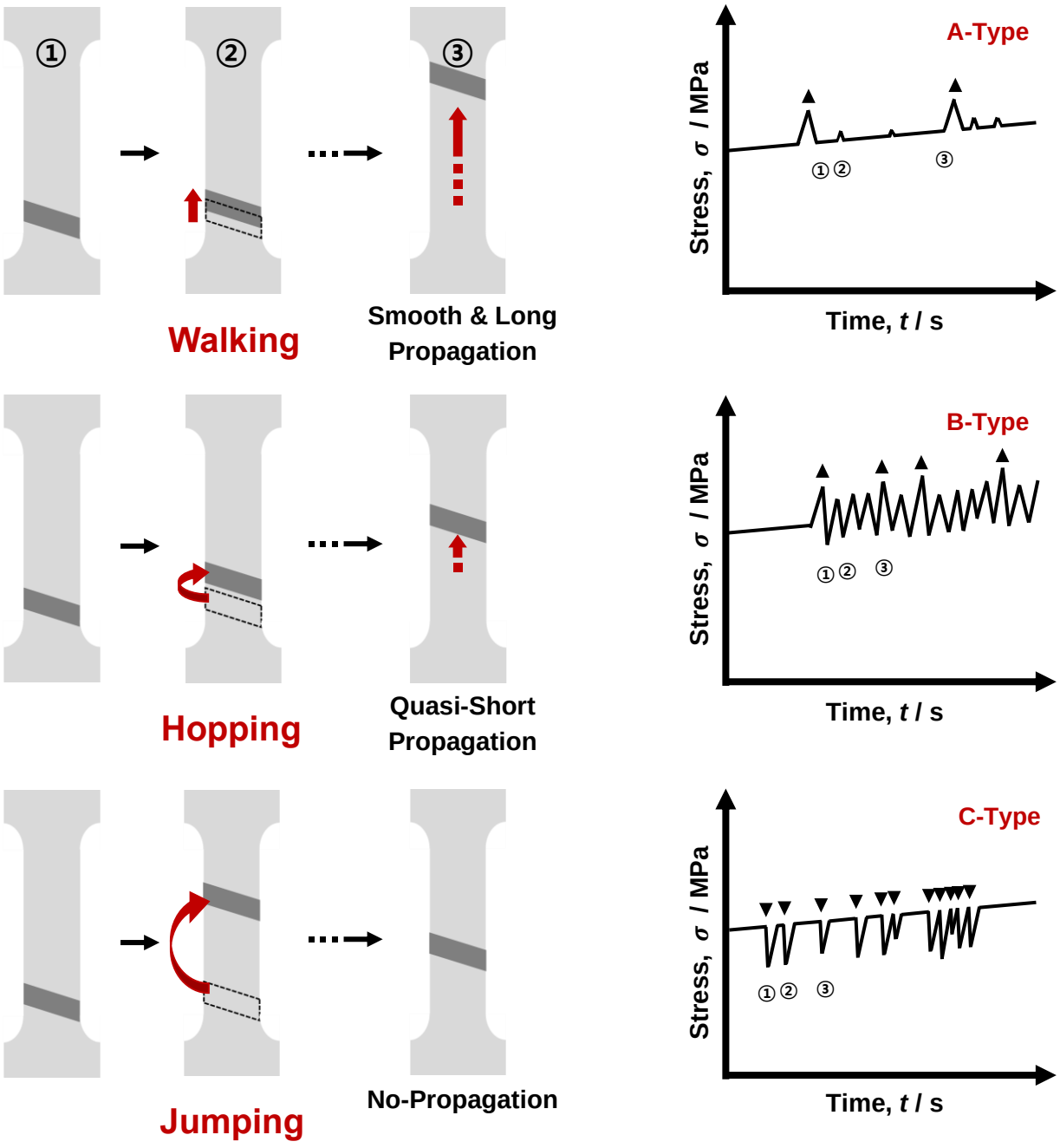

Figure 3.13 Schematic illustration for three types of PLC band propagation and the corresponding serration behavior.

3.3.1.3 Effect of global strain rate on dynamic type transition behavior

Many researchers [7-9] reported that the type of serrated flow generally varies depending on the applied strain rate. C-type serrated flow tends to appear at relatively lower strain rates, whereas A-type serrated flow occurs at higher strain rates, and intermediate strain rates exhibit B-type serrated flow. According to the general transition phenomenon, it is expected that dynamic type transitions of serrated flow and PLC band behavior might be affected by the strain rate. **Fig. 3.14(a)** shows the time variation of the global strain rate during uniform tensile deformation. The global strain rate is not the local strain rate in a PLC band but rather the average plastic strain rate on the gauge part of a test piece, which was calculate\ed by DIC analysis. To clarify the relationship between the serration type and the global strain rate, the values were measured after t = 300 s, at which time the elastic-to-plastic transition in the tensile curve was finished at both 573 K and 623 K. In Fig. 3.14(a), the difference in serration type is indicated with different symbols; squares for A-type, crosses for B-type, and circles for C-type, whereas solid diamonds indicate non-serrated flow. These symbols overlap when the serrated flow shows mixed type. It is clearly shown that the global strain rate is not constant; it dynamically changes during deformation. Before necking, the global strain rate was

always lower than the applied strain rate (10^{-4} s^{-1}). This is mainly because of an elastic contribution of the testing machine at higher temperature [20]. The global strain rate gradually increased with increasing time under A- and B-type serrated flow. However, when C-type serration was activated, the strain rate decreased. From this viewpoint, the type transition of serration is displayed as a function of the global strain rate in **Fig. 3.14(b)**. This figure clearly reveals that the dynamic transition of serration type obeys the increasing global strain rate, and the serration type dynamically changes in the order of C-, B-, and A-types with respect to the strain rate. The dynamic transition order by the global strain rate agrees with the general transition order by the applied strain rate, as reported in previous studies [7-9]. This suggests that the type transition behavior of serrated flow should be discussed in terms of the global strain rate and that the dynamic transition might occur under the condition where the global strain rate changes in the range corresponding to the range for the type transition of serration. Considering the dynamic transition of serration type in relation to PLC band behavior, it also proves that PLC band nucleation manner changes in the order of jumping, hopping, and walking with increasing global strain rate.

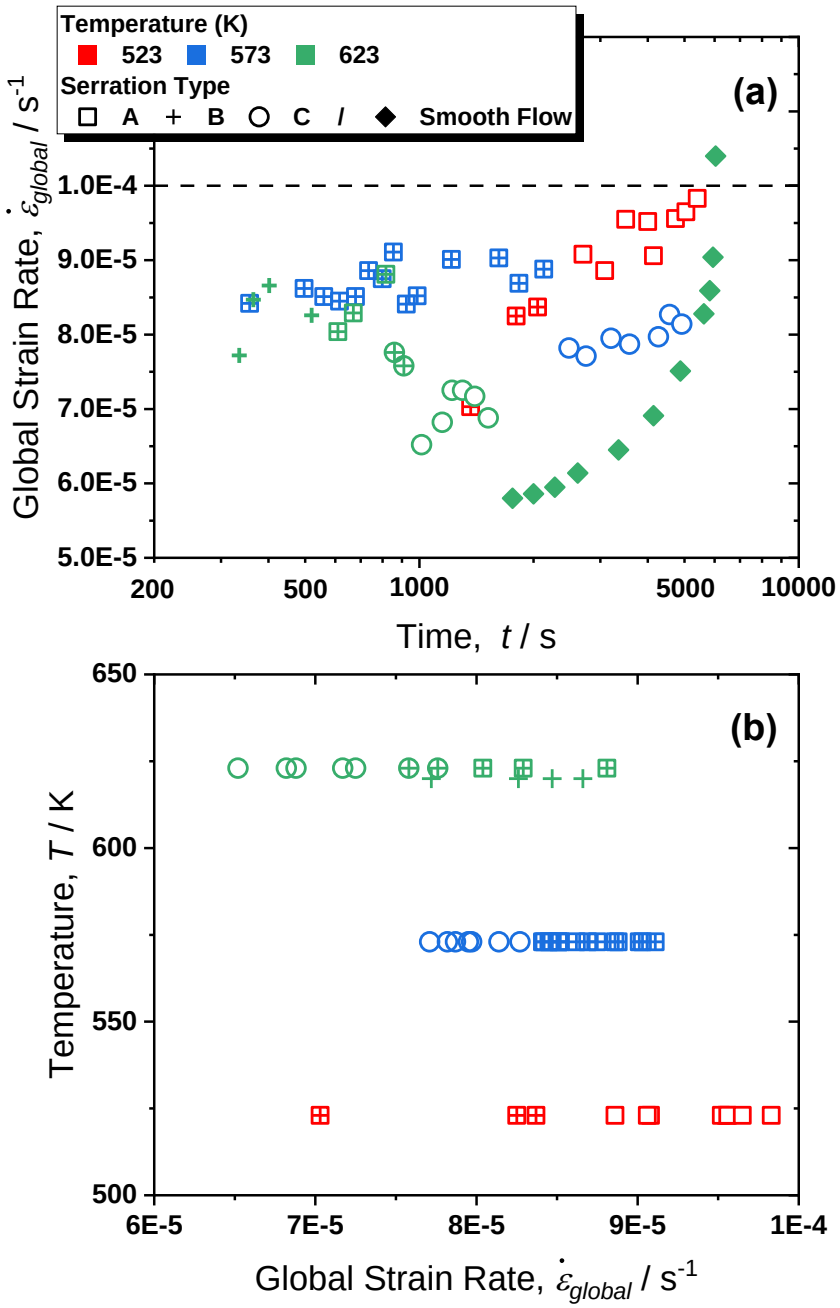

Figure 3.14 (a) Map of global strain rate and deformation time. Three temperatures are colored in red for 523 K, blue for 573 K, and green for 623K. Each serration type is presented by different symbols: squares for A-type, crosses for B-type, circles for C-type, and overlapping symbols for mixed type; (b) map of type transition of serration as a function of the global strain rate.

3.3.2 Numerical simulation for the effect of strain rate on PLC band behavior

The above-mentioned experimental results showed that the change in strain rate has an important role on serration and PLC band behavior. To determine the essential reasons why strain rate affects them, the role of strain rate was investigated using PLC band modeling based on dislocation dynamics.

3.3.2.1 Ananthakrishna (AK) model

The general feature of the PLC effect, especially band propagation behavior, is discussed using the Ananthakrishna (AK) model [25-27] because it can handle PLC band propagation behavior in connection with stress fluctuations on a relatively large scale compared with other methods, e.g., the finite element method [28-29]. The AK model reflects the nature of the dislocation bands (referred to as the PLC band) and their connection to the changes in the nature of the serrations in stress-strain curves. The model consists of three types of dislocation densities: mobile dislocations ρ_m, immobile dislocations ρ_{im}, and dislocations with solute atoms ρ_c. Unlike the Eq. (1-4) in chapter 1, the three dislocation densities vary with time. These types of dislocations are connected to each other, and their time evolutions are expressed as Eqs. (3.1)-(3.3), respectively,

with the stress rate descρibed by Eq. (3.4).

$$\frac{\partial \rho_m}{\partial t} = -\beta \rho_m{}^2 - p\beta \rho_m \rho_{im} + \omega \rho_{im} - \alpha_m \rho_m + \theta v_0 \left(\frac{\sigma_{eff}}{\sigma_y}\right)^{m0} \rho_m + \frac{\Gamma \theta v_0}{\rho_{im}} \frac{\partial}{\partial x^2} \left(\frac{\sigma_{eff}}{\sigma_y}\right)^{m0} \rho_m \qquad (3.1)$$

$$\frac{\partial \rho_{im}}{\partial t} = \beta \rho_m{}^2 + p\beta \rho_m \rho_{im} - \omega \rho_{im} + \alpha_c \rho_c \qquad (3.2)$$

$$\frac{\partial \rho_c}{\partial t} = \alpha_m \rho_m - \alpha_c \rho_c \qquad (3.3)$$

$$\frac{\partial \sigma_a}{\partial t} = E^* \left[\dot{\varepsilon}_a - \frac{b}{L} \int_0^L v_0 \left(\frac{\sigma_{eff}}{\sigma_y}\right)^m \rho_m dx\right] = E^* \left[\dot{\varepsilon}_a - \dot{\varepsilon}_p(t)\right] \qquad (3.4)$$

In Eq. (3.1), the first term refers to the immobilization of two mobile dislocations owing to the formation of locks and junctions. The second term represents the annihilation of a mobile dislocation with an immobile one. The third term indicates the reactivation of an immobile dislocation that has been pinned by solute atoms. The fourth term is related to solute atoms diffusing to mobile dislocations that are arrested temporarily at immobile dislocations. In this model, the mobile dislocations affected by solute atoms are denoted as $\alpha_m \rho_m$, which represents the loss term in Eq. (3.1), whereas it represents the gain term in Eq. (3.3). The term α_m is the factor related to the solute concentration c at the core of the dislocation. It can be expressed as $\alpha_m = D_c(T)c / \lambda^2$, where $D_c(T)$ is the diffusion coefficient of the solutes at temperature T and λ is the effective attractive distance for the

solute diffusion. Because dislocations gradually acquire solutes at rate α_c, they are strongly pinned and become immobile dislocations, ρ_{im}. Thus, $\alpha_c \rho_c$ is the gain term in Eq. (3.2). Immobile dislocations also include dislocations pinned by the solutes through aging process. The fifth term in Eq. (3.1) is the rate of multiplication of dislocations owing to cross-slip. In this term, v_0 is the initial mean velocity of the mobile dislocations, σ_y the yield stress, and m the velocity exponent. Thus, $v_0 = (\sigma_{eff} / \sigma_y)^{m0}$ is the mean velocity of the mobile dislocations on the effective stress $\sigma_{eff} = \sigma_a - h\rho_{im}^{1/2}$, which is based on the so-called Bally–Hirsh equation. The strengthening parameter is given as $h = aGb$ where a is a constant (~0.6), G the shear modulus, and b the magnitude of the Burgers vector. The sixth term in Eq. (3.1) represents spatial coupling between adjacent spatial elements on the gauge part, which means interaction of a PLC band with neighboring regions. Among many proposals on the origin of band propagation (see [30, 31] and references therein), the AK model is based on the double-cross slipping mechanism. The cross-slip process is controlled by high back-stress, which is given by the factor $1/\rho_{im}$. The details are mentioned by Ananthakrishna [32].

Three dislocations contribute to the global stress, as presented in Eq. (3.4). The term E^* is the effective elastic compliance of the specimen and testing machine, $\dot{\varepsilon}_a$ is the

applied strain rate, and L is the gauge length. To simulate this model, we fixed the length scale of the gauge part and used 100 spatial grids. To control the band that only propagates on the gauge part, the ρ_{im} value at both grid ends was set to be two orders of magnitude higher than the value in the other grids. Also, $\rho_m = \rho_c = 0$ was imposed at both ends as the starting condition. Eqs. (3.1)-(3.4) were solved using an adaptive step-size differential equation solver, the ODE23 solver in MATLAB.

3.3.2.2 Setting parameters for AK model

To understand effect of strain rate on PLC band propagation behavior, the AK model was adapted to simulate the PLC effect. To reproduce actual conditions as closely as possible, some parameters in Eqs. (3.1)-(3.4) were given values taken from the experimental results. The steady-state values for three dislocation densities were set to be $\sim 10^{12}$ m^{-2} for ρ_m, $\sim 10^{14}$ m^{-2} for ρ_{im}, and $\sim 10^{13}$ m^{-2} for ρ_c. By using $b = 2.5 \times 10^{-10}$ m and a range of $\dot{\varepsilon}_a$ values from 10^{-6} s^{-1} to 10^{-4} s^{-1}, the values of β and ω were calculated to be $\sim 10^{14}$ m^2/s and $\sim 10^{-4}$/s, respectively. For $\alpha_m = D_c(T)c / \lambda^2$, we first calculated the value of D_c through $D_c = D_0 \exp(-Q / RT)$. Considering the diffusion of interstitial C atoms as the

potential invoker of the DSA process in this temperature range, we referred to the typical values of D_0 and Q of 1.5×10^{-5} m^2/s and 135 kJ/mol, respectively [22], instead of the activation energy value experimentally acquired to alleviate the difficulty in setting parameters. Then, typical values of $c = 0.1$ and $\lambda = 10^{-9}$ m were chosen, and finally we acquired $\alpha_m = 0.5$. Then, using the steady-state condition of Eq. (3-3), α_c was set to be ~0.05. The detailed parameter values are shown in **Table 3.1**. In this study, the applied strain rate in Eq. (4), $\dot{\varepsilon}_a$, was considered as the global strain rate.

3.3.2.3 Effect of strain rate on PLC band propagation and serration behavior

Fig. 3.15(a) shows the time evolution of the PLC band simulated at $T = 523$ K and at the lowest strain rate of the setting condition, $\dot{\varepsilon}_a = 5.00 \times 10^{-6}$ s^{-1}. The z-axis shows the mobile dislocation density ρ_m, and a peak indicates the nucleation of a PLC band associated with a mobile dislocation burst. PLC bands appear to nucleate in random regions of the gauge section. **Fig. 3.15(b)** shows the corresponding global stress behavior when the PLC bands appear with time. Each stress drop means the formation of a PLC band. The global stress repetitively increases and decreases with almost the same

magnitude, which means the nucleation of a PLC band is not affected by another PLC band; in other words, there is no spatial correlation at the lowest strain rate. This type of PLC band behavior is typically referred to as a randomly jumping PLC band with non-propagation, i.e., a C-type PLC band.

As the strain rate increased, $\dot{\varepsilon}_a = 6.25 \times 10^{-6}$ s^{-1}, an interesting feature of PLC band nucleation occurred, as shown in **Fig. 3.16(a)**. It is clearly shown that new PLC bands tend to nucleate near previous PLC bands, as indicated by the dotted yellow lines. This means that spatially coupled correlation begins to work, effectively causing an increase in the number of mobile dislocations at the neighboring region (the region adjacent to the PLC band). Thus, PLC bands appear to partially propagate. This type of PLC band is regarded as a "hopping PLC band," exhibiting B-type PLC band behavior. During the appearance of B-type PLC band behavior, smaller stress fluctuations occur as compared with the large stress peak corresponding to the first PLC band nucleation of the relay nucleation, as shown in **Fig. 3.16(b)**. With further increasing strain rate to $\dot{\varepsilon}_a = 1.00 \times 10^{-5}$ s^{-1}, shown in **Fig. 3.17(a)**, the interval between individual nucleated PLC bands decreases, and the propagating distance increases with incremental increases in the contribution of spatial coupling. The hopping propagation by the series nucleation of PLC

bands is stopped by the nucleation of a new PLC band at a fresh region, as shown by the white arrows (#1 to #4). Accordingly, large stress peaks are associated with the nucleation of a new PLC band in a fresh region, and the stress fluctuates irregularly or oscillates between the large stress peaks, as shown in **Fig. 3.17(b)**. This appearance matches typical B-type serrated flow, as shown in **Fig. 3.10**.

Finally at the highest strain rate, $\dot{\varepsilon}_a = 1.63 \times 10^{-5}$ s^{-1}, the propagating manner of PLC bands appears as a "walking PLC band," as shown in **Fig. 3.18(a)**. It seems that one PLC band nucleates at one end of the gauge part and then propagates smoothly toward the opposite end. Large stress peaks come from the first PLC band formation of the series nucleation, as shown by the white arrows in **Fig. 3.18(b)**. Unlike B-type serrated flow, however, meager stress fluctuation or smooth flow appears between two adjoining large stress peaks because the interval between PLC bands narrows further, resulting in walking propagation of A-type PLC band.

Table 3.1. Parameters used in AK model

ρ_m (m^{-2})	~10^{12}	D_0 (m^2/s)	1.5×10^{-5}
ρ_{im} (m^{-2})	~10^{14}	c	0.1
ρ_c (m^{-2})	~10^{13}	λ (m)	1×10^{-9}
E^* (GPa)	131	Q (J/mol)	135,000
v	0.3	α_m (s^{-1})	0.5
a	0.6	α_c (s^{-1})	0.05
b (m)	2.5×10^{-10}	ω (s^{-1})	5×10^{-4}
σ_y (GPa)	0.14	β (m^2/s)	5×10^{-14}
θv_0 (s^{-1})	1	Γ	5×10^{-9}
$m0$	3		

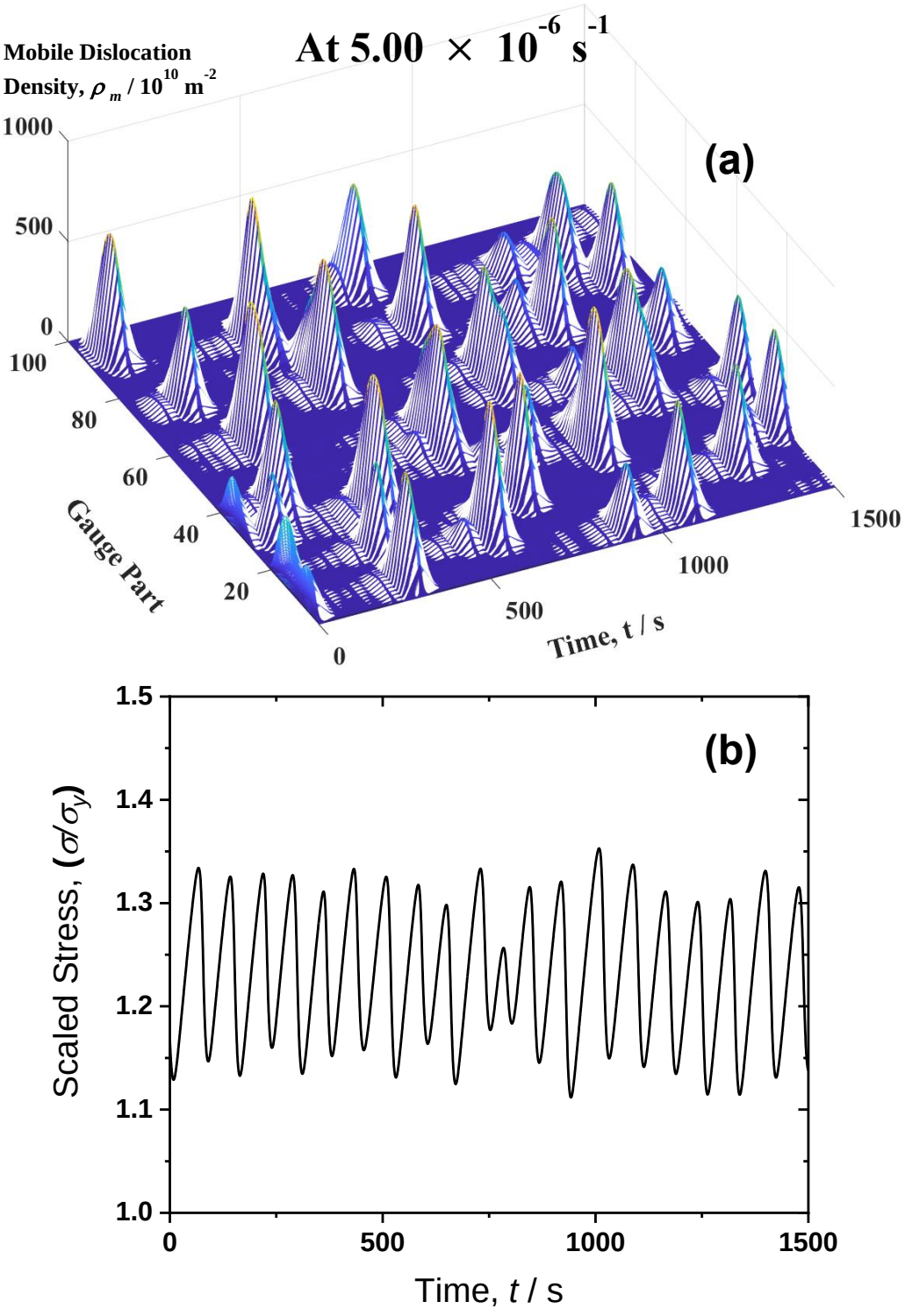

Figure 3.15 (a) Time evolution of PLC band and (b) the corresponding global stress behavior with time as the PLC band evolves at a strain rate of 5.00×10^{-6} s^{-1}. (a) and (b) indicate "jumping" PLC band and typical C-type serrated flow, respectively

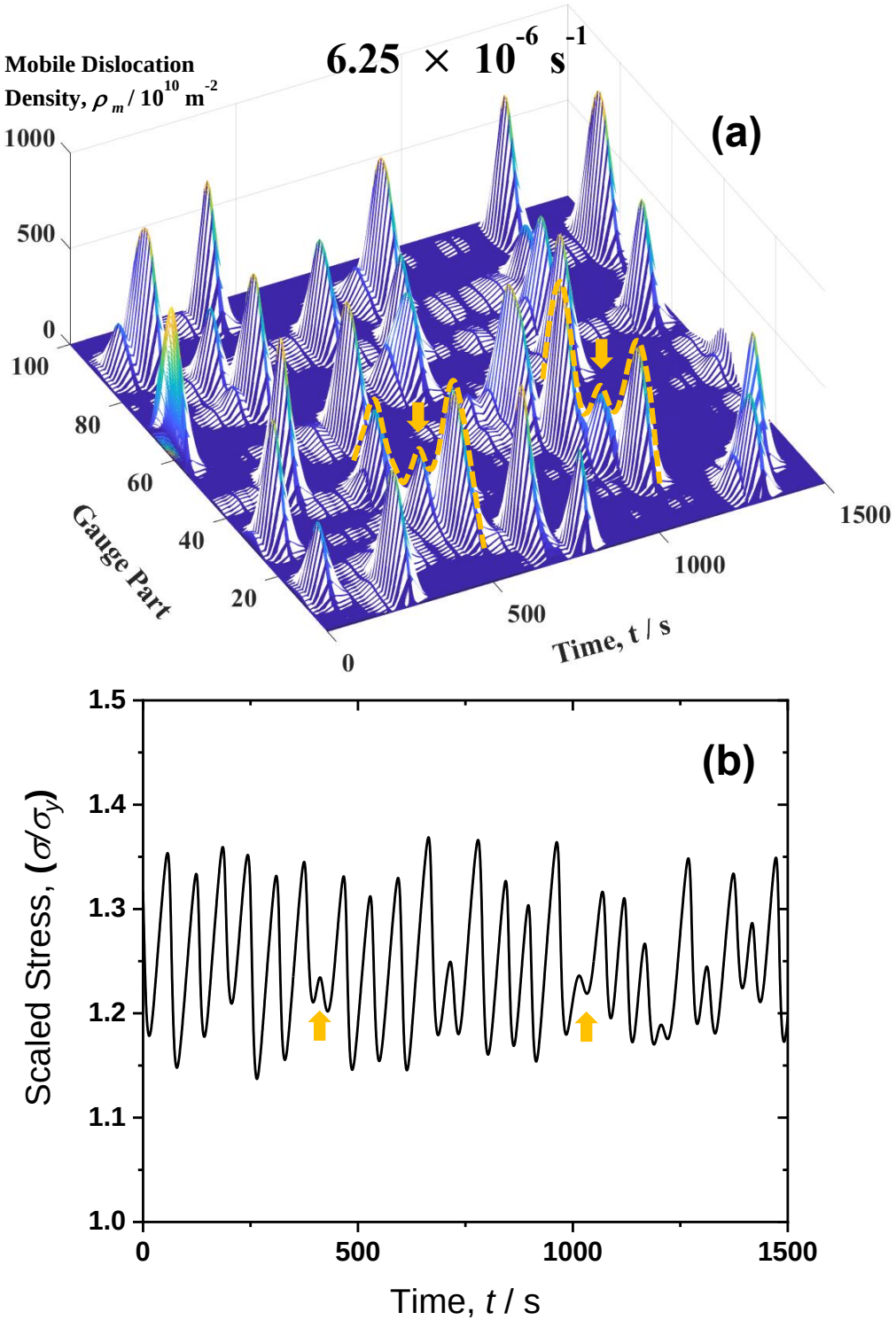

Figure 3.16 (a) Time evolution of PLC band and (b) the corresponding global stress behavior with time when the PLC band evolves at a strain rate of 6.25×10^{-6} s^{-1}.

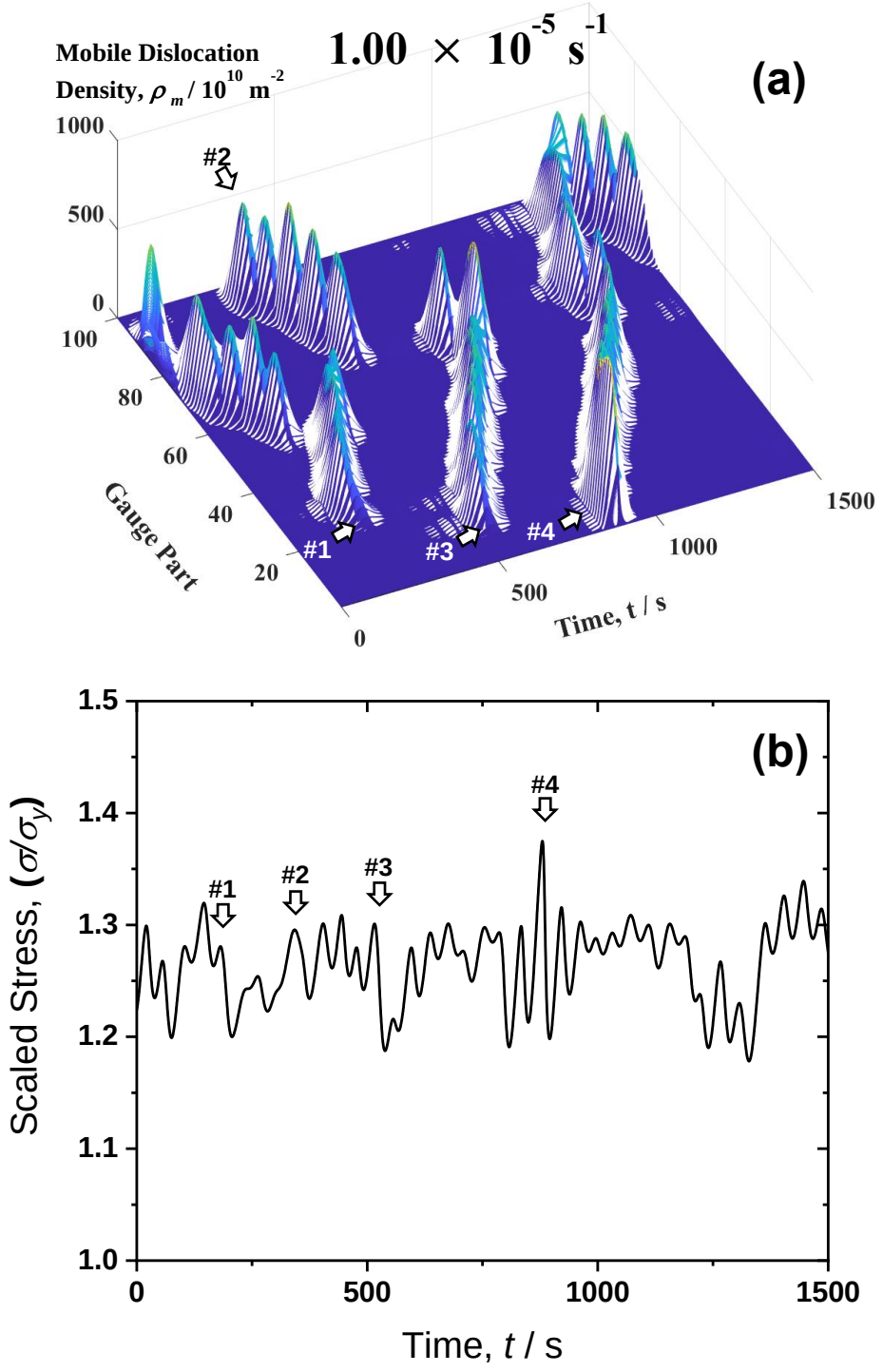

Figure 3.17 (a) Time evolution of PLC band and (b) the corresponding global stress behavior with time when the PLC band evolves at a strain rate of 1.00×10^{-5} s^{-1}. (a) and (b) indicate "hopping" PLC band and typical B-type serrated flow, respectively

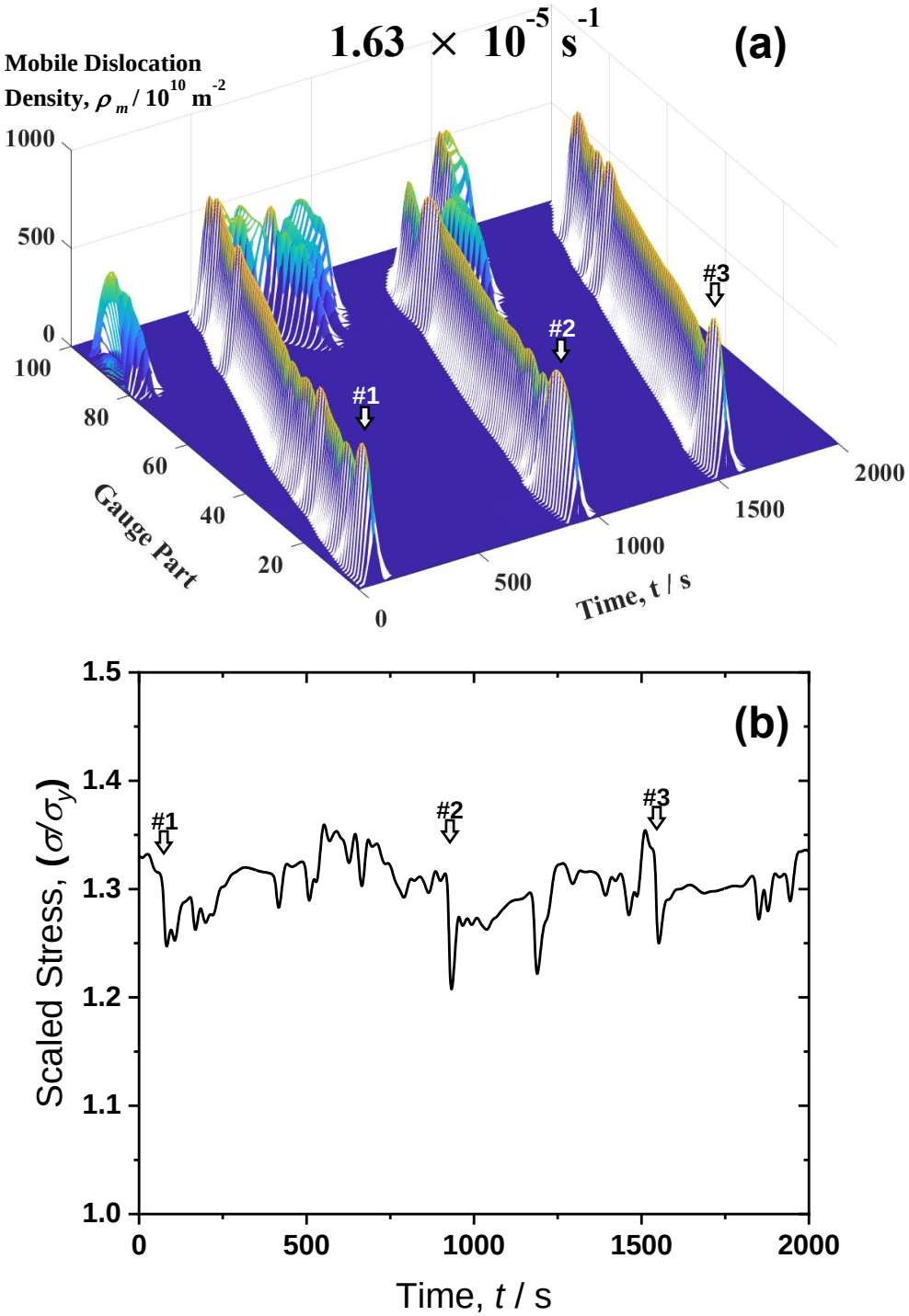

Figure 3.18 (a) Time evolution of PLC band and (b) the corresponding global stress behavior with time when the PLC band evolves at a strain rate of 1.63×10^{-5} s^{-1}. (a) and (b) indicate "walking" PLC band and typical A-type serrated flow, respectively.

3.4 Discussion

As shown by the above results, dislocation-based PLC band modeling reveals the strain rate effect on the nature of PLC band nucleation and propagation. Looking at Eqs. (3.1)-(3.4), the decrease in global stress occurs when the average plastic strain rate consisting of the mobile dislocation density exceeds the applied strain rate. When the applied strain rate is low, it takes a certain amount of time to nucleate a PLC band after the previously nucleated PLC band disappears, which is related to the reloading time scale associated with the applied strain rate [27]. Thus, the next band does not correlate with the previous band, and it can nucleate in a random region. As the reloading time decreases due to the increment in the applied strain rate, however, the time allowed for a burst of mobile dislocation to relax decreases. Thus, there is an insufficient time for dislocation processes to be completed, and the stress relaxation is only partial. Then, it is favorable for the stress relaxation to be mitigated plastically by interacting with the neighboring regions, and the next dislocation burst occurs more easily near the previous PLC band than in an isolated area. Accordingly, a smaller stress peak than the C-type serration peak occurs with the nucleation of next PLC band at spatially correlated region. This is the occurrence of the transition of “Jumping” C-type to “Hopping” B-

type PLC band behavior. As the strain rate further increases, the reloading time decreases further leaving even lesser time for a burst of mobile dislocation to relax. The nucleation of the next burst therefore becomes more favorable to overlap with the previous burst. The propagation distance of the PLC band increases, and stress drop size becomes more smaller during the propagation. It results in the transition of “Hopping” B-type to “Walking” A-type PLC band behavior. From these simulations, it can be concluded that PLC band behavior gradually shifts in the order of C-, B-, and A-type with respect to applied strain rate.

Modeling the effect of strain rate on PLC bands can explain the experimental results. The dynamic transition in propagating manner of a PLC band, from a randomly jumping PLC band to a hopping PLC band to a walking PLC band, originates from both the decrement in the reloading time and the incremental increase in the contribution of spatial-temporal coupling between the PLC band and its neighboring regions with increasing strain rate. The spatial-temporal coupling effect plays an important role on the microscopic manner of PLC band nucleation as follows: As the global strain rate increases, (1) the tendency for nucleation of the next PLC band near the previous one increases, and (2) the macroscopic propagation distance through the series of the PLC

band nucleation increases. According to the macroscopic PLC propagation behavior, serration behavior changes: (1) C-type serrated flow is only composed of large stress peaks related to randomly jumping PLC band nucleation owing to no macroscopic propagation of the PLC band, (2) B-type serrated flow is attributed to the relatively large stress fluctuation (and oscillation) during hopping propagation of the PLC band, and (3) A-type serrated flow results from the strong spatial coupling effect leading to small stress fluctuations during walking PLC band propagation. At both A- and B-type serrated flow, large stress peaks are shown by the first PLC band nucleation of the serial nucleation right before macroscopic PLC band propagation.

Comparing the experiments and the simulations, it was found that the strain rate range showing the PLC band behavior was significantly lower in the simulation: serrated flow with a PLC band occurred at the global strain rates ranging from 6.0×10^{-5} s^{-1} to 1.0×10^{-4} s^{-1} in the experiment, whereas the transition behavior of the PLC band occurred at the applied strain rates from 5.0×10^{-6} s^{-1} to 1.0×10^{-5} s^{-1} in the simulation. This was because of some assumptions used to simplify the simulation as well as an argument of simulating parameters. Nevertheless, it is considered that the dynamic type transition behavior due to the dynamic variation in the global strain rate observed in one

applied strain rate in this experimental result can be explained by the simulated band transition behavior using several applied strain rates in AK model.

Also, the reason why global strain rate decreases with the formation of C-type serration (see Fig. 3.14) has been unclear in this study, although DIC analysis revealed the dynamic change in global strain rate. Given that the global strain rate should increase during deformation [20], activation of the C-type PLC effect might cause the lowering global strain rate.

3.5 Conclusions

In this study, high-temperature tensile testing was carried out under various testing conditions in Fe-19Cr-13Ni-0.2C austenitic stainless steel, and the high-temperature PLC effect associated with DSA was characterized using DIC analysis. The obtained conclusions are as follows:

1. Stress-strain curves clearly exhibited serrated flow at all temperature regions, but the serrated flow behavior looked different depending on deformation time, even at a given temperature. In addition, there were two trends for the type transition of serrated flow: (1) A- and C-type serrations were isolated from each other and (2) B-type serration tended to be activated together with A-type serration rather than C-type serration.

2. High-temperature DIC analysis revealed that the PLC band behavior tended to vary in accordance with the type transition of serrated flow. It was also found that the variation of serrated flow can be essentially attributed to the microscopic manner of PLC band nucleation; the microscopic manner of PLC band nucleation takes place in the manner of walking in A-type, hopping in B-type, and jumping in C-type serration.

3. Global plastic strain rate in the gauge part was not constant but dynamically changed during deformation. In addition, it was revealed that the dynamic transition of serration type obeyed the variation in the global strain rate: the serration type dynamically changed in the order of C-, B-, and A-types with respect to the global strain rate. The dynamic transition order by the global strain rate agreed with the general transition order by the applied strain rate.

4. From the numerical modeling, it was found that the spatial coupling effect plays an important role in the microscopic manner of PLC band nucleation. As the global strain rate increased, (1) the tendency for nucleation of the next PLC band near the previous one increased and (2) the macroscopic propagation distance through the series of the PLC band nucleation increased. As strain rate increased, the serration behavior changed from C-type serrated flow with no macroscopic propagation of the PLC band to B-type serrated flow with hopping propagation of the PLC band owing to the contribution of the spatial coupling and finally to A-type serrated flow with walking PLC band propagation resulting from the strong spatial coupling effect.

3.6 References

[1] A.H. Cottrell, A note on the Portevin-Le Chatelier effect, Phil. Mag. 44 (1953) 829-832.

[2] P.G. McCormick, A model for the Portevin-Le Chatelier effect in substitutional alloys, Acta Metall. 20 (1972) 351-354.

[3] A. van den Beukel, Theory of the effect of dynamic strain ageing on mechanical properties, Phys, Status Solidi A 30 (1975) 197-206.

[4] A. van den Beukel, On the mechanism of serrated yielding and dynamic strain ageing, Acta Metall. 28 (1980) 965-969.

[5] P.G. McCormick, Dynamic strain ageing, Trans. Indian Inst. Met. 39 (1986) 98-106.

[6] A.H. Cottrell and B.A. Bilby, Dislocation theory of yielding and strain ageing of iron, Proc. Phys. Soc. A 62 (1949) 49-62.

[7] Y. Zhang, J.P. Liu, S.Y. Chen, X. Xie, P.K. Liaw, K.A. Dahmen, J.W. Qiao and Y.L. Wang, Serration and noise behaviors in materials, Prog. Mater. Sci. 90 (2017) 358-460.

[8] A. Yilmaz, The Portevin-Le Chatelier effect: A review of experimental findings, Sci. Tech. Adv. Mater. 12 (2011) 063001.

[9] P. Rodriguez, Serrated plastic flow, Bull. Mater. Sci. 6 (1984) 653-663.

[10] Q. Yu, P. A. Greaney, T.M. Evans and J.J. Kruzic, A critical dislocation velocity for serration mechanism transition in a nickel-chromium solid solution alloy, Int. J. Plast. 145 (2021) 103071.

[11] D.P. Rao Palaparti, V. Ganesan, J. Christopher and G.V. Prasad Reddy, Tensile flow analysis of austenitic type 316LN stainless steel: Effect of nitrogen content, J. Mater. Eng. Performance, 30 (2021) 2074-2082.

[12] H. Wang, C. Berdin, M. Maziere, S. Forest, C. Prioul, A. Parrot and P. Le-Delliou, Portevin-Le Chatelier (PLC) instabilities and slant fracture in C-Mn steel round tensile specimens, Scr. Mater. 64 (2011) 430-433.

[13] S. Fu, T. Cheng, Q. Zhang, Q. Hu and P. Cao, Two mechanisms for the normal and inverse behaviors of the critical strain for the Portevin-Le Chatelier effect, Acta Mater. 60 (2012) 6650-6656.

[14] M. Koyama, Y. Shimomura, A. Chiba, E. Akiyama and K. Tsuzaki, Room-temperature blue brittleness of Fe-Mn-C austenitic steels, Scr. Mater. 141 (2017) 20-23.

[15] H. Ait-Amokhtar and C. Fressengeas, Crossover from continuous to discontinuous propagation in the Portevin-Le Chatelier effect, Acta Mater. 58 (2010) 1342-1349.

[16] M. Mehenni, H. Ait-Amokhtar and C. Fressengeas, Spatiotemporal correlations in the Protevin-Le Chatelier band dynamics during the type B-type C transition, Mat. Sci. Eng. A 756 (2019) 313-318.

[17] X. Feng, G. Fischer, R. Zielke, B. Svendsen and W. Tillmann, Investigation of PLC band nucleation in AA5754, Mater. Sci. Eng. A 539 (2012) 205-210.

[18] K. Renard, S. Ryelandt and P.J. Jacques, Characterisation of the Portevin-Le Chatelier effect affecting an austenitic TWIP steel based on digital image correlation, Mater. Sci. Eng. A 527 (2010) 2969-2977.

[19] H. Halim, D.S. Wilkinson and M. Niewczas, The Portevin-Le Chatelier (PLC) effect and shear band formation in an AA5754 alloy, Acta Mater. 55 (2007) 4151-4160.

[20] S.Y. Lee, C. Takushima, J. Hamada and N. Nakada, Macroscopic and microscopic characterizations of Portevin-Le Chatelier effect in austenitic stainless steel using high-temperature digital image correlation analysis, Acta Mater. 205 (2021) 116560.

[21] L.H. de Almeida, I. Le May and P.R.O Emygdio, Mechanistic modelling of dynamic strain aging in austenitic stainless steels, Mater. Charact. 41 (1998) 137-150.

[22] J. Mola, G. Luan, Q. Huang, C. Ullrich, O. Volkova and Y. Estrin, Dynamic strain aging mechanism in a metastable austenitic stainless steel, Acta Mater. 212 (2021) 116888.

[23] K. Peng, K. Qian and W. Chen, Effect of dynamic strain aging on high temperature properties of austenitic stainless steel, Mat. Sci. Eng. A 379 (2004) 372-377.

[24] L. Shi and D.O. Northwood, The mechanical behavior of an AISI type 310 stainless steel, Acta Metall. Mater. 43 (1995) 453-460.

[25] J. Kumar, R. Sarmah and G. Ananthakrishna, General framework for acoustic emission during plastic deformation, Phys. Rev. B 92 (2015) 144109.

[26] R. Sarmah and G. Ananthakrishna, Influence of system size on spatiotemporal dynamics of a model for plastic instability: Projecting low-dimensional and extensive chaos, Phys. Rev. E 87 (2013) 052907.

[27] R. Sarmah and G. Ananthakrishna, Correlation between band propagation property and the nature of serrations in the Portevin-Le Chatelier effect, Acta Mater. 91 (2015) 192-201.

[28] S.C. Ren, T.F. Morgeneyer, M. Maziere, S. Forest and G. Rousselier, Effect of Luders and Portevin-Le Chatelier localization bands on plasticity and fracture of notched steel specimens studies by DIC and FE simulations, Int. J. Plast. 136 (2021) 102880.

[29] M. Maziere, J. Besson, S. Forest, B. Tanguy, H. Chalons and F. Vogel, Numerical aspects in the finite element simulation of the Portevin-Le Chatelier effect, Comput.

Methods Appl. Mech. Eng. 199 (2010) 734-754.

[30] M. Zaiser and P. Hähner, Oscillatory modes of plastic deformation: theoretical concepts, Phys. Status Solidi B 199 (1997) 267-330.

[31] L.P. Kubin, C. Fressengeas and G. Ananthakrishna, Collective behaviour of dislocations, in: F.R.N. Nabarro, M.S. Duesbery (Eds.), Dislocations in Solids, Elsevier, Amsterdam, 2002, pp. 101-192.

[32] G. Ananthakrishna and M.S. Bharathi, Phys. Rev. E5 70 (2004) 026111.

3.7 Appendix

3.7.1 Three Dislocations Behavior during the PLC effect in AK model

Fig. 3.19 indicates the contour maps showing the dynamic variation in three dislocations (ρ_m (a), ρ_{im} (b) and ρ_c (c)) with time under a typical C-type PLC effect at lower strain rate (5.00×10^{-6} s^{-1}). The x, y and z-axis are respectively showing the gauge part position, time and dislocation density. The result was taken at an arbitrary time range. It shows that each mobile dislocation burst matches with the nucleation of the PLC band, as shown in Fig. 3.15. The mobile dislocations change to the Cottrell dislocations through the diffusion process of solute atoms (through the term, $-\alpha_m\rho_m$ in Eq. 3.1), as shown in Fig. 3.19 (b). Then, the Cottrell dislocations are fully pinned by the aging process of the solute atoms and those transform to the immobile dislocations (through the term, $-\alpha_c\rho_c$ in Eq. 3.3). This is a cycle of DSA process. After the full transformation from the Cottrell dislocations to the immobile dislocations, the next PLC band nucleates through the reactivation term ($+\omega\rho_{im}$ in Eq. 3.1) at random region and the next one does not correlate with the previous one, which is the typical randomly jumping C-type PLC band behavior. It is also noteworthy that the C-type PLC band tends to nucleate preferentially at the region where immobile dislocation density is low. This means C-type PLC bands prefer

to nucleate at softer region with higher effective stress in a gauge part.

In the case of typical A-type PLC band behavior at higher strain rate (1.63×10^{-5} s^{-1}), on the other hand, A-type PLC band prefers to nucleate at the end of the gauge part, as shown in **Fig. 3.20**. The first PLC band nucleates at the end of the gauge part, and then the aging process is activated. Unlike C-type PLC band behavior, however, the next PLC band nucleates before the first PLC band are fully immobilized through the DSA process. A series of the PLC band nucleation occurs before the previous bands are fully immobilized, which is the typical walking A-type PLC band behavior.

3.7.2 Determination of the PLC band width

Although the PLC band propagation behavior was fully discussed as mentioned above, the PLC band formation behavior was not detailed. **Fig. 3.21(a)** indicates a typical C-type serrated flow, and **Fig. 3.21(b)** and **(c)** show the contour map of the mobile and immobile dislocation, respectively. When stress drop occurs (from point (1) to point (2) in Fig. 3.21(a)), PLC band nucleates at an element in gauge part. Then, the PLC band grows to the neighboring region during the stress drop, and the growth stops by changing to the

Cottrell dislocations. It means the PLC band width is balanced by the competition between the mobile dislocation burst by the spatial coupling terms (the fifth and sixth terms in Eq. 3.1) and DSA process during the stress drop (in a very short time).

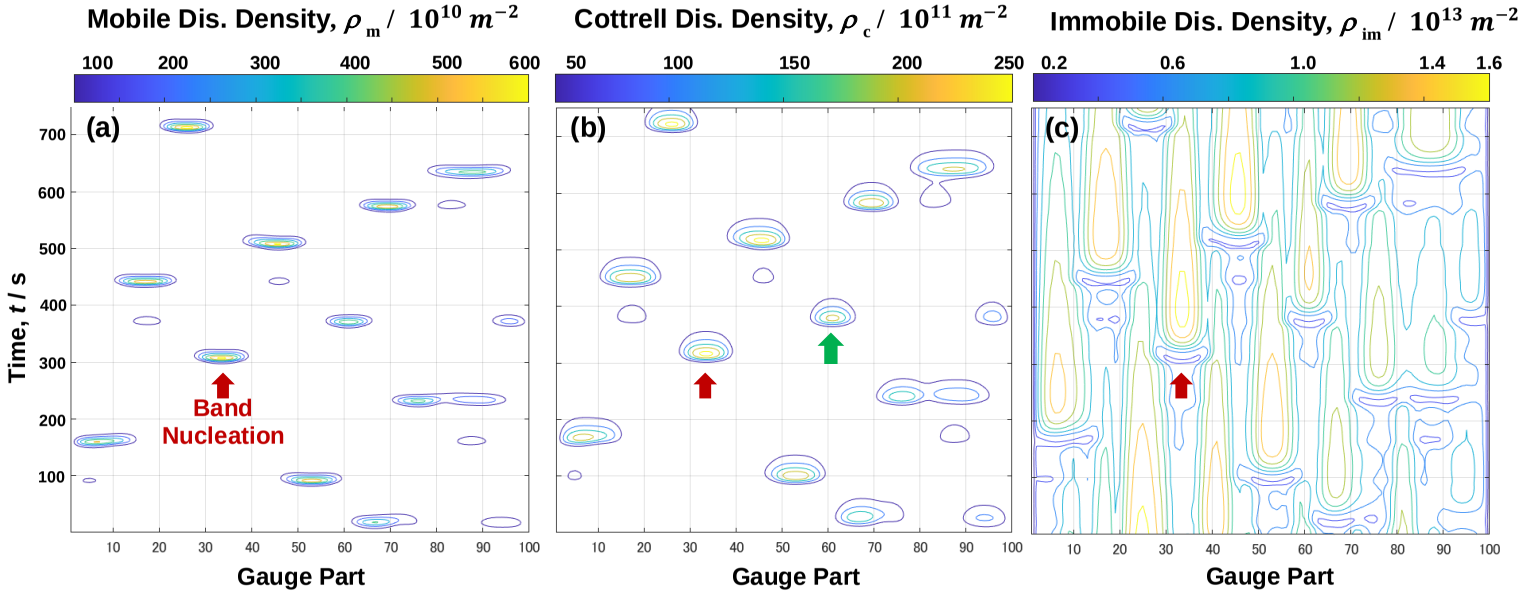

Figure 3.19 Contour map showing the density distribution of the mobile dislocation (a), the immobile dislocation (b), and the Cottrell dislocation (c), respectively, under typical C-type PLC band behavior at a strain rate of 5.00×10^{-6} s^{-1}. Note that the next PLC band (green arrow) nucleate after the Cottrell dislocations inside the previous PLC band (red arrow) are fully immobilized.

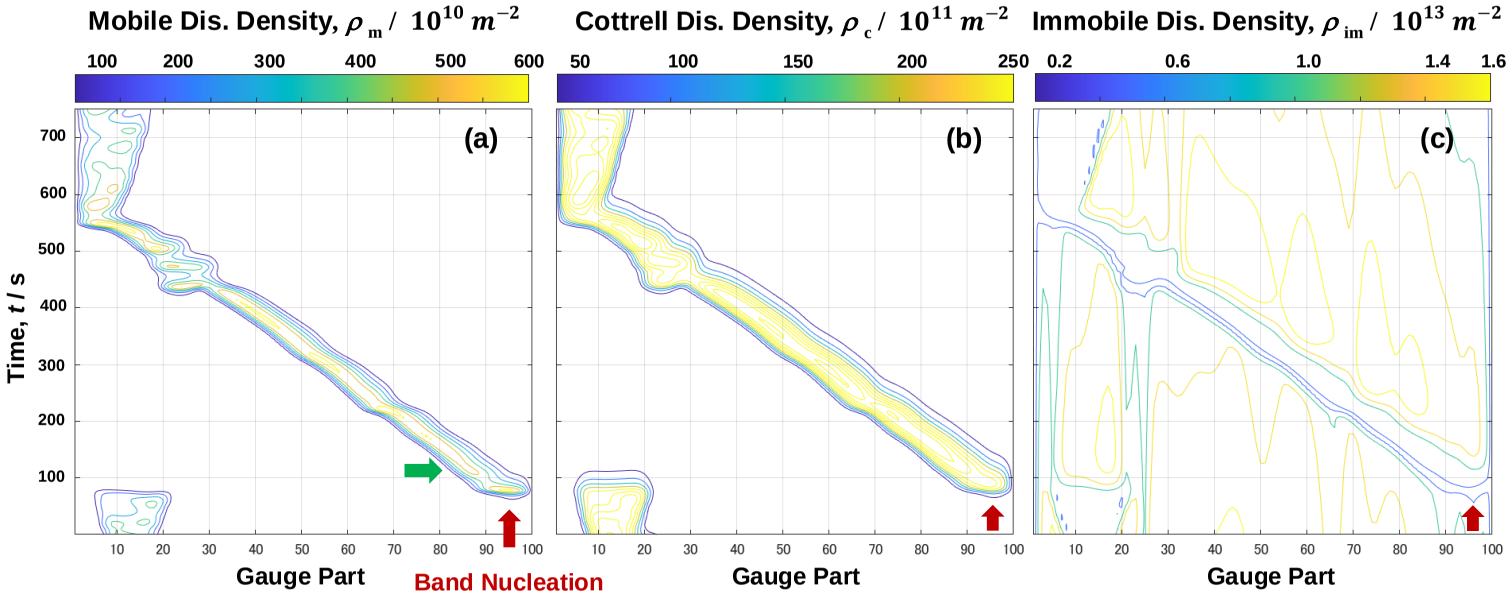

Figure 3.20 Contour map showing the density distribution of the mobile dislocation (a), the immobile dislocation (b), and the Cottrell dislocation (c), respectively, under typical A-type PLC band behavior at a strain rate of 1.63×10^{-5} s^{-1}. Note that the next PLC band (green arrow) nucleates before the Cottrell dislocations inside the previous PLC band (red arrow) are fully immobilized.

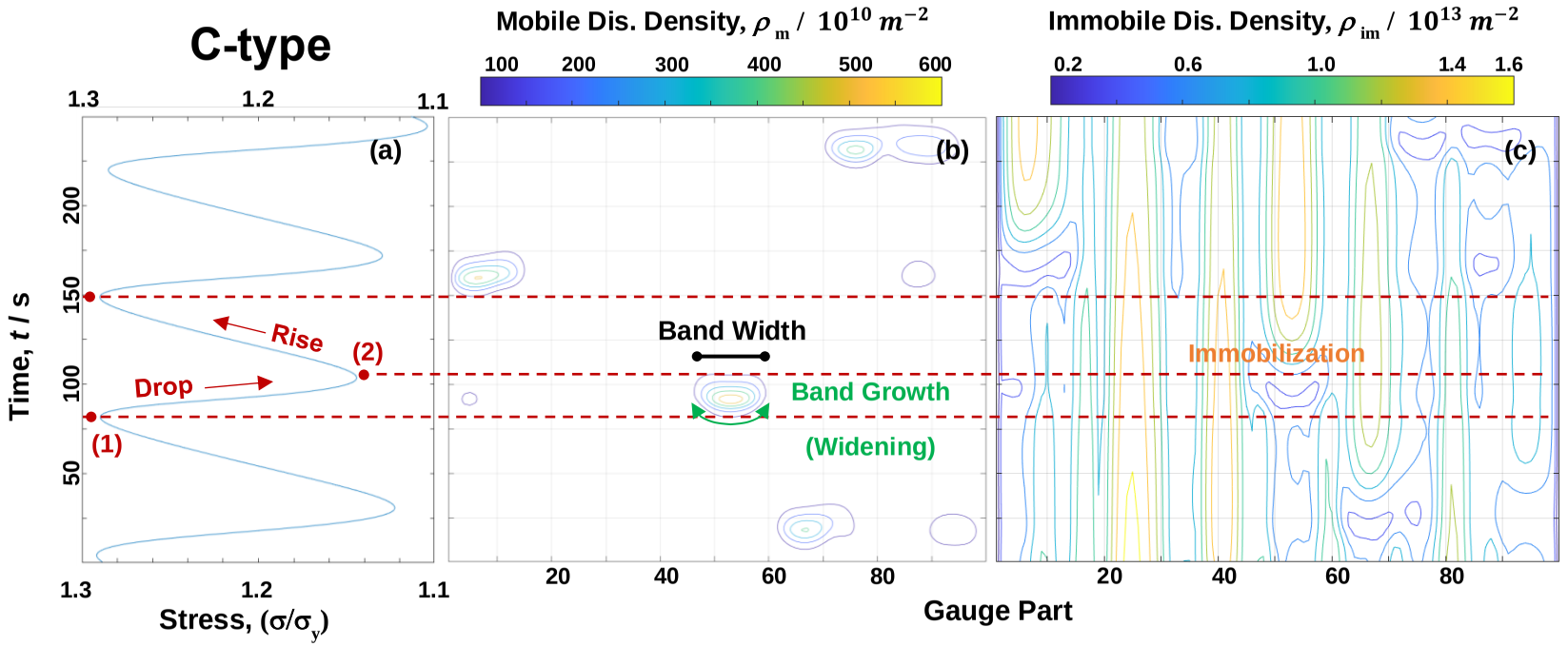

Figure 3.21 (a) Stress profile with time, and corresponding contour map showing the density distribution of the mobile dislocation (b), the immobile dislocation (c), respectively, under typical C-type PLC effect at a strain rate of 5.00×10^{-6} s^{-1}.

Chapter 4

Effects of Grain Size and Interstitial Atoms on the Portevin-Le Chatelier Effect in Austenitic Stainless Steel

4.1 Introduction

Austenitic stainless steels (γ-STS) are being used at various fields where the required condition for the usage of γ-STSs in each field are very diverse. Various properties required in each field are tailored by the addition of other alloying elements as well as Chromium (Cr), or by improving manufacturing conditions. Especially, to use γ-STS for high-temperature applications, fine austenite stability, long-term fatigue, and creep resistance are necessary. It has been reported that their properties of γ-STSs and other high-temperature structural materials are significantly influenced by microstructural factors, such as grain size and alloying elements [1-4]. As for austenite stability and strengthening of γ-STS, the addition of nitrogen (N) is very promising [5].

Meanwhile, many previous studies have reported (and also as discussed in the previous chapters) that dynamic strain aging (DSA) and its resulting PLC effect occurs at the elevated temperature in γ-STS with small amount of carbon (C) [6-13]. It is widely known that DSA depends greatly on the testing conditions like applied strain rate and temperature, since they affect the mean dislocation velocity and diffusivity of solute atoms. However, there are few studies on the effect of grain size and interstitial N on the

PLC effect in γ-STS, despite of higher possibility of that they also can change DSA kinetics. In this chapter, therefore, its effects influencing on the PLC effect were investigated using stable γ-STSs with C or N in terms of serration behavior and PLC band characteristics.

4.2 Experimental

4.2.1 Material

In this chapter, two stable austenitic stainless steels with different interstitial atoms, C and N, were used. Each chemical composition is detailed in **Table 4.1**. In this chapter, each C- and N-containing γ-STS refers to as HCS and HNS, respectively. In order to obtain a fully recrystallized austenite single-phase structure with various grain sizes in both materials, cold-rolled plates of 2 mm thickness were solution-treated at various temperatures for 3.6 ks, followed by water-cooling. HCS and HNS materials were solution-treated above 1373 K and 1273 K, respectively, to dissolve precipitates into austenite matrix, $Cr_{23}C_6$ for HCS and Cr_2N for HNS, respectively. Inverse Pole Figure (IPF) maps showing a recrystallized austenite single-phase at each different condition were summarized in **Fig. 4.1**. HCS had the average grain diameters of 13 μm and 67 μm, while HNS had 30 μm, 75 μm, and 155 μm with increasing solution-treated temperature.

4.2.2 Tensile testing and DIC analysis

Tensile testing and DIC analysis were carried out under high-temperature DSA region in this chapter. Same experimental procedure for tensile testing and DIC analysis was done as mentioned in the section 2.2.2 and 2.2.3.

Table 4.1 Chemical composition of the austenitic stainless steels used in this chapters

wt.%	Cr	Ni	Mn	Si	P	S	C	N	Fe
HCS	19.3	13.5	0.8	0.04	0.004	0.0006	0.208	0.004	Bal.
HNS	19.3	13.6	0.8	0.05	0.003	0.0005	0.005	0.204	Bal.

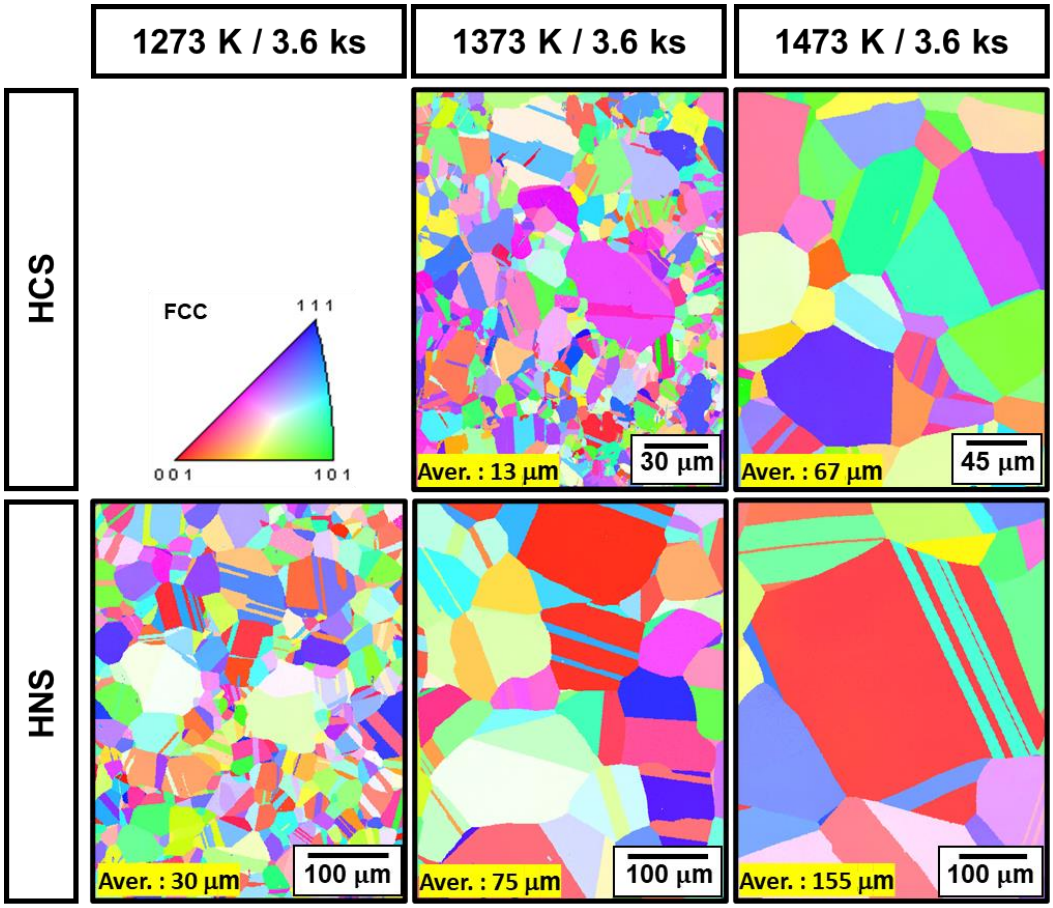

Figure 4.1 Inverse pole figure (IPF) maps for the initial microstructure of HCS and HNS solution-treated at various temperatures.

4.3 Results and discussion

4.3.1 Effect of grain size

4.3.1.1 Serration behavior

As an example of grain size effect on serration behavior, **Fig. 4.2** (a) and (b) indicate engineering stress-strain curves tested at 773 K for HCS and 823 K for HNS, respectively, under an applied strain rate of 10^{-4} s^{-1}. As shown in Fig. 4.2 (a), the black and red lines indicate HCS with 13 μm and 67 μm in grain diameter, respectively. They showed a typical grain size effect that yield stress increases with decreasing grain size. As for the serration behavior in HCS, all materials showed a single A-type serration behavior, but there were some differences as followings. With decreasing grain size, (1) critical strain for the onset of serrated flow decreases, as shown by black arrows; (2) the stress amplitude of A-type serration peaks sizes, defined as $\Delta\sigma_{DSA}$, increases, and the periodicity of the serration peaks decreases. Similar to HCS, HNS also showed the grain size effect of HCS, as shown in Fig. 4.2 (b). With decreasing grain size from 155 μm (blue line) to 30 μm (black line), higher yield stress and $\Delta\sigma_{DSA}$, and lower critical strain were observed, and all three curves had A-type serrated flow.

In DSA model as explained in section 1.3.1, the Eq. (1.8) in relation to dislocation density can be expressed considering grain size [14-17].

$$\rho = H' \frac{\varepsilon^{\beta}}{\mu^{n}} \qquad (4.1)$$

μ is the grain size and n is the exponent value ranging from 0 to 1. This equation expresses the tendency that total dislocation density ρ increases with decreasing grain size. Considering the grain size factor, the Eq. (1.10) can be rearranged as

$$(\varepsilon^{DSA})^{m+\beta} = SZ'\dot{\varepsilon}\,\mu^{n} exp(\frac{Q}{RT}) \quad . (4.2)$$

Accordingly, Eq. (4.2) indicates that the critical strain decreases with decreasing grain size. Therefore, the grain size effect on critical strain can be explained as followings. Austenite grain boundaries can act not only as mobile dislocation nucleation source but also as the effective obstacle for invoking DSA process. For these reasons, the critical condition for DSA is accomplished at lower strain with decreasing grain size.

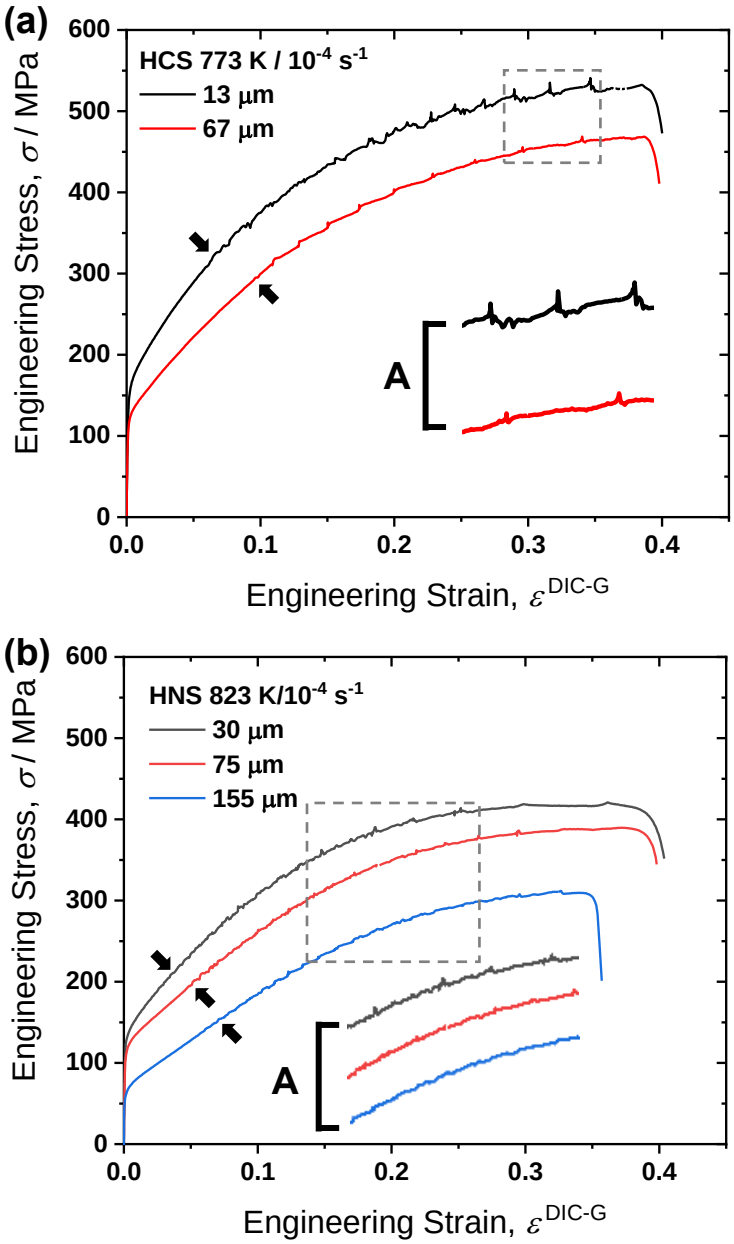

Figure 4.2 Engineering stress-strain curves of (a) HCS at 773 K and (b) HNS at 823 K, respectively, with varying grain size under an applied strain rate of 10^{-4} s^{-1}.

4.3.1.2 A-type PLC band behavior

Fig. 4.3 (a) indicates the magnified stress-strain curves of HCS with various grain sizes, which indicates typical A-type serrated flow. In order to understand the A-type serration behavior, high-temperature DIC analysis was conducted, and the obtained results were displayed in **Fig. 4.3 (b)** for HCS with 67 μm and in **Fig. 4.3 (c)** for HCS with 13 μm. The DIC images were taken at the strains indicated by black dotted points in Fig. 4.3 (a). It is commonly shown in both specimens that the PLC bands continuously propagate in the typical A-type "walking" manner, as mentioned in chapter 3, although the nucleation site of the A-type PLC bands is different between both materials: the PLC bands nucleated at an end of the gauge part in HCS with grain diameter of 67 μm, while they repeatedly nucleated at the central region of the gauge part in the case of grain size 13 μm. It was confirmed that the difference in nucleation site of PLC band is not the grain size effect by similar analyses with other specimens, although the detail reason has not been cleared yet. The grain size variation led to a slight difference in the PLC band width and the local strain (rate) inside each PLC band. In case of HCS, the PLC band width was ~4 mm for 67 μm and ~5 mm for 13 μm. Also, it was confirmed that the local strain rate inside the PLC band was hardly changed at 1.02×10^{-3} s^{-1} regardless of the grain size

difference. That is, although HCS with finer grain size seemed to have higher $\Delta\sigma_{DSA}$, it can be concluded that the grain size variation does not affect the nature of A-type PLC band behavior. This tendency was also identified in HNS.

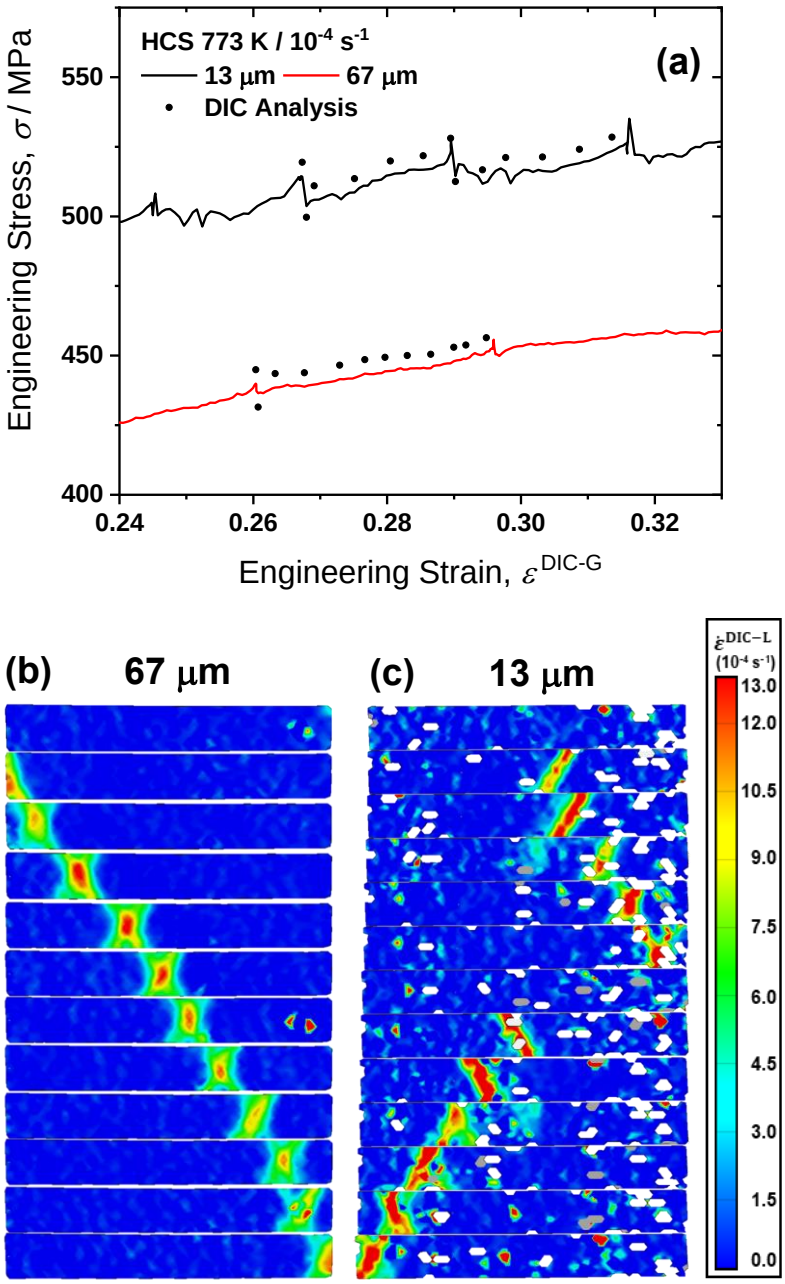

Figure 4.3 (a) Magnified stress-strain curves of Fig. 4.2(a); Strain rate distribution map showing A-type PLC band propagation in the gauge part of a test piece in HCS with (b) 67 μm and (c) 13 μm, respectively, deformed at 773 K/10^{-4} s^{-1}. Each image in (b) and(c) was acquired at the strain represented by the black dots in the stress-strain curve in (a).

4.3.2 Effect of replacement of C by N

Fig. 4.4 (a) and **(b)** exhibit engineering stress-strain curves of HCS (black line) and HNS (red line) tested at 773 K and 823 K, respectively, under an applied strain rate of 10^{-4} s^{-1}. In order to simply compare the effect of interstitial atoms for PLC effect in γ-STS under high-temperature DSA region, the materials having a comparable grain size, HCS with 67 μm and HNS with 75 μm, were selected. The yield stress is similar between HCS and HNS at two testing temperatures, but HCS has higher ultimate tensile strength than HNS at both temperatures due to higher strain hardening rate. With increasing testing temperature, however, the strain hardening effect in HCS significantly decreases, leading to the decrement in both ultimate tensile strength and uniform elongation. On the contrary, uniform elongation was improved maintaining high ultimate tensile strength in HNS.

Regarding the serration behavior, the serrated flow transited from A- to B-type in HCS with increasing testing temperature from 773 K to 823 K, while the typical A-type serrated flow is remained in HNS even at higher temperature. **Fig. 4.5** indicates the temperature dependence of the critical strain ε^{DSA} in both HCS and HNS, which shows the variation of $\ln \varepsilon^{DSA}$ as a function of $1/T$. It is obviously found that ε^{DSA} decreased in

HNS more significantly than in HCS with increasing temperature. As mentioned in chapter 2, the slope in this figure means the value of $1/(m + \beta) \times Q/R$. Assuming the ($m + \beta$) value in HNS is comparable with 2.42 in HCS as calculated in chapter 2, the activation energy Q was calculated to be ~413 kJ/mol in HNS. This value is about 2.3 time higher than the activation energy of 183 kJ/mol for the pipe diffusion of Cr in HCS, and comparable to the bulk diffusion of the substitutional atoms of Cr (400 kJ/mol) [18]. This high value may be attributed to a strong interaction between Cr and N [5,19], which might be enough high to form Cr-N pairs or nano-precipitates in N-bearing austenitic stainless steel [19-21]. Although the detailed discussion for the serration mechanism in HNS was not implemented in this study, it is obvious that replacing of C with N leads to the restriction of the Cr diffusion leading to effective DSA at higher temperature.

These results suggest that when γ-STSs are considered to be used in various industrial fields, type of alloying elements in γ-STSs and its manufacturing conditions must be considered as well as its operating environment such as temperature and deformation condition.

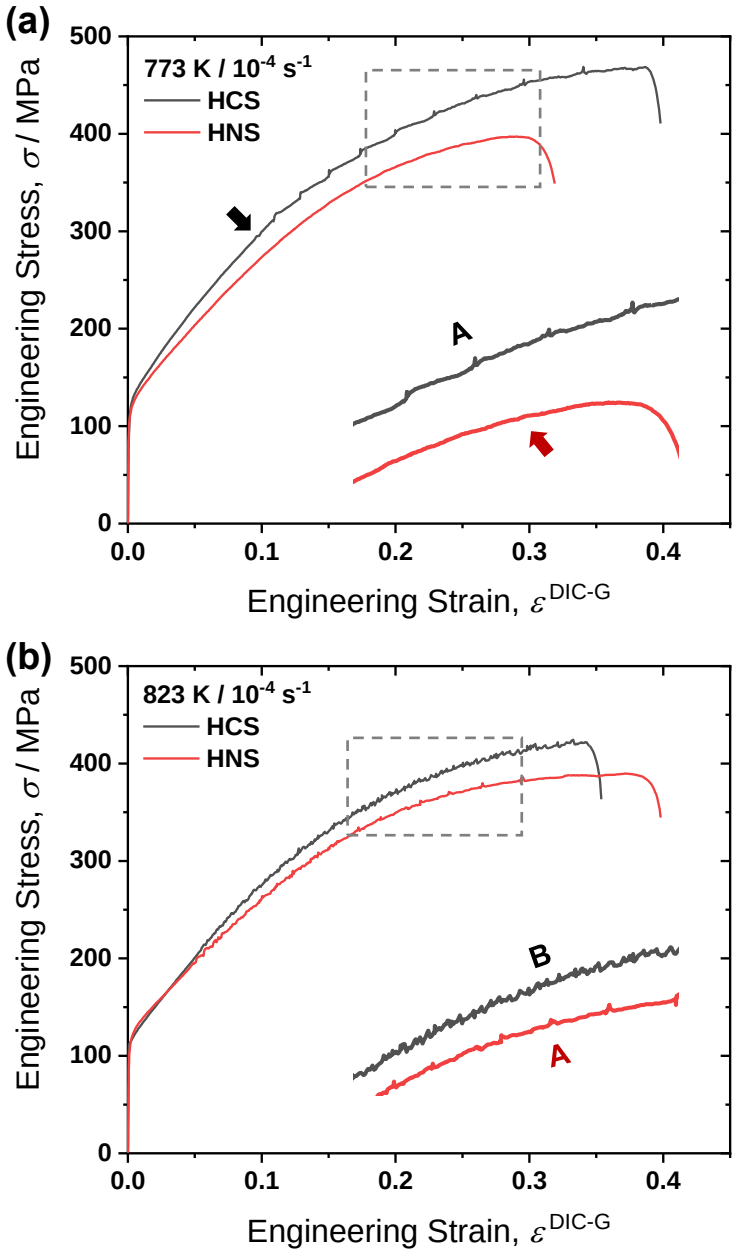

Figure 4.4 Engineering stress-strain curves of HCS (black line) and HNS (red line) tested at (a) 773 K and (b) 823 K, respectively, under an applied strain rate of 10^{-4} s^{-1}.

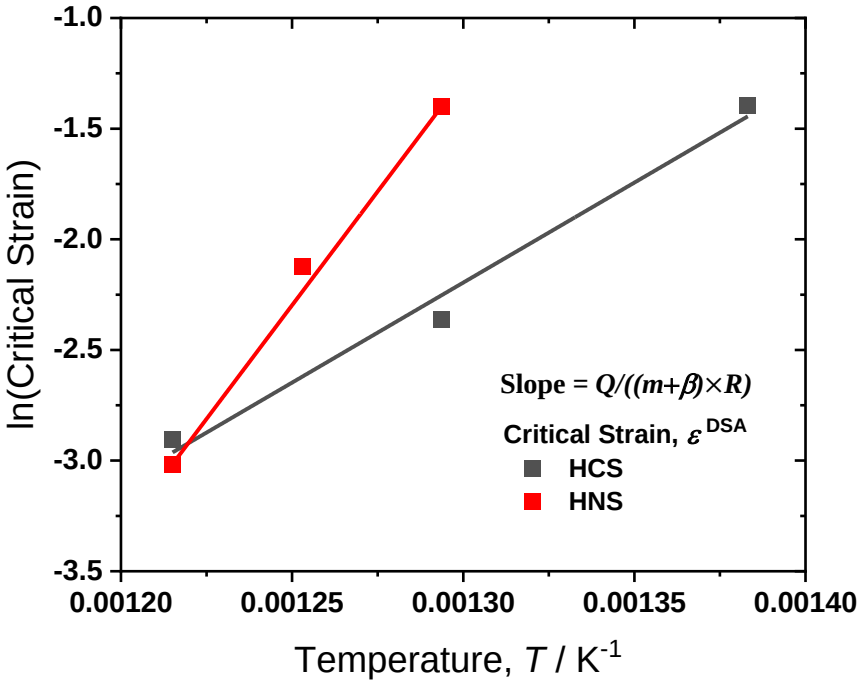

Figure 4.5 *ln* $\varepsilon^{\text{DIC-G}}$ and $1/T$ at the applied strain rate of 10^{-4} s^{-1}. $\varepsilon^{\text{DIC-G}}$ in each testing condition was measured by DIC analysis.

4.4 Conclusion

In this chapter, the effects of grain size and replacement of C by N on the PLC effect in γ-STS were investigated in terms of serration behavior and the PLC band characteristics. The obtained conclusions are as follows:

1. With decreasing grain size, yield stress and ultimate tensile strength increased in both HCS and HNS. Regarding serration behavior, both HCS and HNS with varying grain size had a typical A-type serrated flow and the critical strain for the dynamic strain aging decreased with decreasing grain size. This suggests that austenite grain boundaries act as a preferential nucleation site for mobile dislocations.

2. Regardless of variation in grain size, the nature of A-type PLC band characteristics, such as the width and local strain within the PLC band, hardly changed in both HCS and HNS.

3. Replacing C with N in γ-STS decreased strain hardening effect leading to the reduction of ultimate tensile strength and uniform elongation. However, γ-STS bearing N maintains the effective PLC effect even at 823 K. This may be because N has stronger interaction between Cr compared with C.

4.5 References

[1] K.H. Lo, C.H. Shek and J.K.L. Lai, Recent developments in stainless steels, Mat. Sci. Eng. R 65 (2009) 39-104.

[2] L.A. James, The effect of grain size upon the fatigue-crack propagation behavior of alloy 718 under hold-time cycling at elevated temperature, Eng. Frac. Mech. 25 (1986) 305-314.

[3] R. Jiang, S. Everitt, M. Lewandowski, N Gao and P.A.S. Reed, Grain size effects in a Ni-based turbine disc alloy in the time and cycle dependent crack growth regimes, Int. J. Fatigue 62 (2014) 217.227.

[4] D.W. Kim, Influence of nitrogen-induced grain refinement on mechanical properties of nitrogen alloyed type 316LN stainless steel, J. Nucl. Mater. 420 (2012) 473-478.

[5] J.W. Simmons, Overview: high-nitrogen alloying of stainless steels, Mater. Sci. Eng. 207 (1996) 159-169.

[6] D.W. Kim, W.S. Ryu, J.H. Hong, S.K. Choi, Effect of nitrogen on the dynamic strain ageing behaviour of type 316L stainless steel, J. Mater. Sci. 33 (1998) 675-679.

[7] D.W. Kim, W.G. Kim, W.S. Ryu, Role of dynamic strain aging on low cycle fatigue and crack propagation of type 316L(N) stainless steel, Int. J. Fatigue 25 (2003) 1203-1207.

[8] S.G. Hong and S.B. Lee, Mechanism of dynamic strain aging and characterization of its effect on the low-cycle fatigue behavior in type 316L stainless steel, J. Nucl. Mater. 340 (2005) 307-314.

[9] L.J. Meng, J. Sun, H. Xing, G.W. Pang, Serrated flow behavior in AL6XN austenitic stainless steel, J. Nucl. Mater. 394 (2009) 34-38.

[10] I. Nikulin and R. Kaibyshev, Deformation behavior and the Portevin-Le Chatelier effect in a modified 18Cr-8Ni stainless steel, Mater. Sci. Eng. A 528 (2011) 1340-1347.

[11] V. Ganesan, K. Laha, M. Nandagopal, P. Parameswaran, M.D. Mathew, Effet of nitrogen content on dynamic strain ageing behaviour of type 316LN austenitic stainless steel during tensile deformation, Mater. High Temp. 31 (2014) 162-170.

[12] B.K. Choudhary, Activation energy for serrated flow in type 316L(N) austenitic stainless steel, Mater. Sci. Eng. A 603 (2014) 160-168.

[13] A.S. Alomari, N. Kumar, K.L. Murty, Serrated yielding in an advanced stainless steel Fe-25Ni-20Cr (wt%), Mater. Sci. Eng. A 751 (2019) 292-302.

[14] W. Charnock, The influence of grain size on the nature of portevin-lechatelier

yielding, Phil. Mag. 18 (1968) 89-99.

[15] B.J. Brindley and P.J. Worthington, Serrated yielding in aluminium-3%magnesium, Acta Metall. 17 (1969) 1357-1361.

[16] S. Miura and H.Yamauchi, Influence of grain size on the Portevin-LeChatelier effect in Al-Mg alloys, Trans. JIM 13 (1972) 82-88.

[17] P.G. McCormick, Effect of grain size on serrated yielding in an Al-Mg-Si alloy, Phil. Mag. 23 (1971) 949-956.

[18] C.F. Jenkins, G.V. Smith, Serrated plastic flow in austenitic stainless steel, Trans. Metall. Soc. AIME 245 (1969) 2149.

[19] K. Tong, F. Ye and Y.K. Wang, Short-range ordered structure and phase stability of supersaturated nitrided layer on austenitic stainless steel, Acta Mater. 175 (2019) 314-323.

[20] P. Shankar, D. Sundararaman and S. Ranganathan, Clustering and ordering of nitrogen in nuclear grade 316LN austenitic stainless steel, J. Nucl. Mater. 254 (1998) 1-8.

[21] D. Sundararaman, P. Shankar and V.S. Ranganathan, Eletron microscopy study of Cr2N formation in thermally aged 316LN austenitic stainless steels, Metall. Mater. Trans. A 27 (1996) 1175-1186.

Chapter 5

Conclusions and Remarks

In this study, the Portevin-Le Chatelier (PLC) effect in Fe-19Cr-13Ni-0.2(C or N) austenitic stainless steels (γ-STS) were investigated. In order to clarify plastic deformation behavior under the PLC effect, high-temperature tensile testing equipped with Digital Image Correlation (DIC) system was carried out at various temperatures (473 - 823 K) and strain rates (5.0×10^{-5} - 1.0×10^{-2} s^{-1}). The PLC effect originated from dynamic strain aging (DSA) appeared at two different temperature ranges; low-temperature DSA region (473 - 623 K) and high-temperature DSA region (723 - 823 K) in an Fe-19Cr-13Ni-0.2C γ-STS. The low- and high-temperature DSA behavior was attributed to the pipe diffusion of interstitial C and substitutional Cr, respectively. Under the distinction between two temperature ranges, the research results and discussions of each chapter were conducted based on the phenomenon that appeared in one of the two temperature ranges.

In chapter 1, "Research Background", basics of the PLC effect and DSA and the motivation and objective of this study were described.

In chapter 2, "Macroscopic and Microscopic Characterizations of the Portevin-Le Chatelier Effect in Austenitic Stainless Steel using High-temperature Digital Image Correlation Analysis", the tensile deformation behavior accompanied with the PLC effect was investigated using DIC analysis at temperatures of 723-823 K under various applied strain rates of 10^{-4} s^{-1} - 5×10^{-3} s^{-1}. With the help of the DIC analysis, the global strain in the gauge part of a tensile specimen and the local strain in a PLC band were precisely measured regardless of the lowering machine stiffness at a high temperature. The high-temperature DIC analysis could identify the critical strain and strain rate conditions where stress-strain curve indicated serrated flow. it was also confirmed that the local strain gently increased in a gauge part through a PLC band propagation, which promoted a repeatable A-type PLC band propagation in the same direction. Furthermore, the local strain was discontinuously developed by the repeatable formation of PLC bands; consequently, the local strain rate became remarkably high within a PLC band. In addition, the local strain rate in the PLC band monotonically increased with the increase in the number of PLC bands. From this viewpoint, it was discovered that necking deformation occurs suddenly at the PLC band, when the local strain rate exceeds the critical value, where dynamic strain aging is ineffective.

In chapter 3, "Serrated Flow Accompanied with Dynamic Type Transition of the Portevin-Le Chatelier Effect in Austenitic Stainless Steel", the dynamic type transitions of the Portevin-Le Chatelier (PLC) effect were investigated in an Fe-19Cr-13Ni-0.2C austenitic stainless steel by considering the corresponding relationship between serrated flow and PLC band behavior. Different types of serration appeared in the stress–strain curve at temperatures from 473 K to 623 K, even at a constant applied strain rate, and the type transition took place dynamically in a certain order with deformation time. DIC analysis revealed that the PLC band propagation behavior also changed in accordance with the dynamic transition of serration type and that the transition of the PLC band propagation behavior could be attributed to the PLC band nucleation manner: "jumping" PLC band with C-type serration, "hopping" PLC band with B-type serration, and "walking" PLC band with A-type serration. In addition, it was found that the dynamic transition of the PLC effect was closely related to the dynamic variation in the global strain rate of the gauge part of the specimen with time. Furthermore, numerical modeling proved that the nucleation manner of PLC band nucleation changed in the order of jumping, hopping, and walking as the strain rate increased owing to the spatial-temporal coupling effect between the PLC band and neighboring regions.

In chapter 4, "Effects of Grain Size and Interstitial Atoms on the Portevin-Le Chatelier Effect in Austenitic Stainless Steel", the effects of grain size and interstitial atoms of C and N on the PLC effect in γ-STS were investigated in terms of serration behavior and the PLC band characteristics. Various grain sizes were acquired by solution-treatment from 1273 K to 1473 K in Fe-19Cr-13Ni austenitic stainless steels containing 0.2C (HCS) or 0.2N (HNS). The grain size increases with increasing the solution-treatment temperature. The critical strain for onset of serrated flow decreased with decreasing grain size in both HCS at 773 K and HNS at 823 K. It is closely related to the role of austenite grain boundaries where mobile dislocations are nucleated preferentially and also their movement is effectively hindered through DSA process. DIC analysis revealed that the nature of A-type PLC band characteristics hardly changed in both HCS and HNS regardless of the variation in grain size. Replacing C with N in γ-STS significantly increased the activation energy for the onset of serrated flow. It is attributed to a strong interaction between Cr and N, and thereby Cr diffusion is restricted by N leading to effective DSA at higher temperature in HNS, as compared with HCS.

This study was successfully able to observe inhomogeneous deformation behavior under the high-temperature PLC effect in γ-STS. Based on the experimental results, controlling mechanism of the high-temperature PLC effect and its effect influencing on mechanical properties were clarified in terms of the PLC band characteristics. These accomplishments will further develop the research on high-temperature structural materials not only academically but also industrially.

Acknowledgements

まず最初に、博士学位論文作成まで私を導いてくださった東京工業大学 指導教授の中田伸生先生に謝意を表します。いつも積極的で私のために頑張ってくださったことに対していつも感謝しながら生きていきます。私がこれから進んでいく研究に対する心構えと姿勢を中田先生を見て手本にします。

I would like to appreciate Prof. Byoungchul Hwang in Seoul National University of Science and Technology for let me experience the overall knowledge of various fields in metallurgy from Bachelor to Master's degree. I also thank to Dr. Jae-hyeok Shim and Dr. Jin-Yoo Suh in Korea Institute of Science Technology (KIST) for all the support that you'd given me. With the help of you all, I learned so many experimental and analyzing tools during Master's degree and intern researcher.

SEM と放電加工機使用など色んな装備使用を提供してくださった同大学　教授尾中晋先生にも感謝を表します。そして、試験片を提供してくださった日鉄ステンレス株式会社 濱田 純一さんと多久島 睦子さんに謝意を表します。

I appreciate Prof. Ritupan Sarmah and Ms. Sita Chettri for setting and calculating the AK model.

また、日本に来てからこれまで共にしてまいりました中田研究室の卒業生および在学生の方々にも感謝の意を表します。特に、日本に来たばかり時に研究以

外に生活的な適応にも役に立った私の DIC 先生長廻拓海とそのファミリーたち（福井大介、高橋尚太郎、雨宮雄太郎、Rui Bao、和田侑樹）に感謝します。

Lastly, I love and thank to my family for everything.